

**A Theoretical and Experimental Study on Solar Assisted Cooking System to
Produce Bulgur by Using Parabolic Trough Solar Collector**

Ph.D. Thesis

in

Mechanical Engineering

University of Gaziantep

Supervisor

Prof. Dr. M. Sait SÖYLEMEZ

by

İbrahim Halil YILMAZ

December 2014

© 2014 [İbrahim Halil YILMAZ]

REPUBLIC OF TURKEY
UNIVERSITY OF GAZIANTEP
GRADUATE SCHOOL OF NATURAL & APPLIED SCIENCES
MECHANICAL ENGINEERING DEPARTMENT

Name of the thesis : A Theoretical and Experimental Study on Solar Assisted
Cooking System to Produce Bulgur by Using Parabolic Trough Solar Collector

Name of the student : İbrahim Halil YILMAZ

Exam date : 15.12.2014

Approval of the Graduate School of Natural and Applied Sciences

Prof. Dr. Metin BEDİR

Director

I certify that this thesis satisfies all the requirements as a thesis for the degree of Doctor
of Philosophy.

Prof. Dr. M. Sait SÖYLEMEZ

Head of Department

This is to certify that we have read this thesis and that in our consensus opinion it is
fully adequate, in scope and quality, as a thesis for the degree of Doctor of Philosophy.

Prof. Dr. M. Sait SÖYLEMEZ

Supervisor

Co-Supervisor

Examining Committee Members

Prof. Dr. Hüsametdin BULUT

Prof. Dr. M. Sait SÖYLEMEZ

Prof. Dr. Mustafa BAYRAM

Assoc. Prof. Dr. Recep YUMRUTAŞ

Assoc. Prof. Dr. Önder KAŞKA

Signature

I hereby declare that all information in this document has been obtained and presented in accordance with academic rules and ethical conduct. I also declare that, as required by these rules and conduct, I have fully cited and referenced all material and results that are not original to this work.

İbrahim Halil YILMAZ

ABSTRACT

A THEORETICAL AND EXPERIMENTAL STUDY ON SOLAR ASSISTED COOKING SYSTEM TO PRODUCE BULGUR BY USING PARABOLIC TROUGH SOLAR COLLECTOR

YILMAZ, İbrahim Halil

Ph.D. in Mechanical Eng.

Supervisor: Prof. Dr. M. Sait SÖYLEMEZ

December 2014, 175 pages

In this dissertation, a pilot study has been performed for design, testing and model-based analysis of a cooking process-heat application assisted with Parabolic Trough Solar Collector (PTSC). An experimental setup consisting essentially of cooking pot, water preheating tanks, auxiliary heater, plate heat exchanger, thermal expansion tanks, PTSC array and measurement devices has been constructed and operated on campus of Gaziantep University to perform these purposes. The described Solar Assisted Process Heat (SAPH) system has been tested and monitored with a number of experiments under different operating conditions to investigate its technical feasibility and integrated performance for producing boiled wheat. On the other hand, thermal and mathematical models of each system component have been developed based on the fundamental scientific and engineering principles. Furthermore, physical insight of cooking phenomena has been described in detail, and three different cooking pots have been designed, tested and compared for their thermal performance. Finally, after model validations have been satisfied, a real-time transient simulation of the designed SAPH system has been carried out to specify the performance parameters and the annual solar fraction. The simulation results have shown that the solar fraction can supply 20.8% of the annual amount of energy consumed by the process heat application for the provided operating conditions.

Keywords: Parabolic trough collector, solar assisted process heat, wheat, transient analysis, thermal system design

ÖZET

PARABOLİK OLUK KOLEKTÖRÜYLE GÜNEŞ DESTEKLİ PIŞİRME SİSTEMİNDEN BULGUR ÜRETİMİNİN TEORİK VE DENEYSEL ÇALIŞILMASI

YILMAZ, İbrahim Halil
Doktora Tezi, Makine Müh.
Danışman: Prof. Dr. M. Sait SÖYLEMEZ
Aralık 2014, 175 sayfa

Bu tezde, Parabolik Oluk Güneş Kolektör (POGK) yardımıyla bir pişirme ısı-proses uygulamasının tasarım, test ve model-tabanlı analizi için pilot bir çalışma gerçekleştirilmiştir. Bu amaçları yerine getirmek için temel olarak pişirme kazanı, su ön-ısıtma tankları, yardımcı ısıtıcı, plakalı ısı değiştirgeç, termal genleşme tankları, POGK ağı ve ölçüm cihazlarından oluşan bir deney düzeneği Gaziantep Üniversitesi kampüsün'de kurulmuş ve devreye alınmıştır. Tasvir edilen Güneş Destekli Proses Isı (GDPI) sistemiyle kaynamış buğday üretiminin teknik açıdan yapılabilirliğini ve bütünlük sistem verimini incelemek amacıyla farklı çalışma koşulları altında çok sayıda deneyle test edilmiş ve gözlemlenmiştir. Diğer taraftan, her bir sistem bileşeninin termal ve matematiksel modelleri temel bilimsel ve mühendislik prensipleri kullanılarak geliştirilmiştir. Ayrıca, pişirme olgusunun fiziksel iç yüzü detaylı şekilde tanımlanmış ve üç farklı pişirme kazanı tasarlanarak test edilmiş ve kazanların termal verimleri karşılaştırılmıştır. Son olarak, model doğrulamalarının sağlanmasına müteakip tasarlanan GDPI sisteminin gerçek-zamanlı ve zamana bağlı benzetimi yapılarak sistemin performans parametreleri ve yıllık güneş kullanımı belirlenmiştir. Benzetim sonuçları göstermiştir ki sağlanan çalışma şartlarında, ısı proses uygulaması yıllık tüketmiş olduğu enerji miktarının %20,8'ini güneş enerjisi kullanımından sağlayabilmektedir.

Anahtar kelimeler: Parabolik oluk kolektör, güneş destekli proses ısı, buğday, zamana bağlı analiz, termal sistem tasarımı

ACKNOWLEDGEMENTS

I express my appreciation to Prof. Dr. M. Sait Söylemez for his supervision, understanding and encouragement throughout this thesis by setting me free for independent research and to develop myself scientifically. I would like to thank also Assoc. Prof. Dr. Recep Yumrutaş for his advices and concern. Further, I would like to thank Prof. Dr. Mustafa Bayram for agreeing to be part of the examination committee and contributing his valuable comments to the content of this dissertation.

I would like to thank Lider Mühendislik and its workers, especially to Mech. Eng. Hakan Hayta, for their help and support during installation of the experimental setup. Many thanks also to my colleague, Res. Asst. Fatih Balcı who helped me to analyze the properties of wheat grains. In addition, I couldn't forget to thank Prof. Dr. Hüsamettin Bulut for sharing solar radiation data. I would like to give special thanks to Electric & Electronic Eng. Ergün Menetlioğlu. Also, thanks to Assoc. Prof. Dr. Önder Kaşka and Res. Asst. Abdulkadir Ayanoğlu for their spiritual supports and friendships, and the employees of Mechanical Workshop for their supports.

I couldn't find the right words to say my wife, Feyza Yılmaz and my family for their supports and patience.

I acknowledge the financial support provided by the Gaziantep University Scientific Research Projects Fund under Grant No. MF.11.13.

CONTENTS	Page
ABSTRACT	v
ÖZET	vi
ACKNOWLEDGEMENTS	vii
CONTENTS	viii
LIST OF TABLES	xiii
LIST OF FIGURES	xiv
NOMENCLATURE	xvii
CHAPTER 1	1
INTRODUCTION	1
1.1 Background and motivation	1
1.2 Aim and objectives	6
1.3 Outline of the thesis	7
CHAPTER 2	9
LITERATURE REVIEW.....	9
2.1 Introduction	9
2.2 Applications on solar-integrated industrial process heat	9
2.3 Progress in solar-integrated industrial process heat	15
2.4 Design approaches for solar process heat systems	16
2.5 Summary	20
CHAPTER 3	21
MODELING OF PARABOLIC TROUGH SOLAR COLLECTOR	21
3.1 Introduction	21
3.2 Parabolic trough solar collector system	24

3.2.1 System description	24
3.2.2 Solar radiation on tracking aperture	25
3.2.3 Optical analysis	30
3.2.3.1 Reflectance of parabolic mirror	30
3.2.3.2 Cover transmittance	32
3.2.3.3 Absorptivity of absorber	35
3.2.3.4 Intercept factor of PTSC	35
3.2.3.5 Geometric factor	37
3.2.3.6 Miscellaneous factor	38
3.3 Thermal analysis of receiver	38
3.3.1 Heat loss analysis	39
3.3.1.1 Heat transfer to HTF	42
3.3.1.2 Heat conduction through absorber	43
3.3.1.3 Heat transfer in annulus region	44
3.3.1.3.1 Free molecular convection	45
3.3.1.3.2 Natural convection	46
3.3.1.3.3 Thermal radiation	48
3.3.1.4 Heat transfer from retainers	49
3.3.1.5 Heat conduction through cover	50
3.3.1.6 Heat transfer from receiver to surroundings	50
3.3.1.6.1 Convection to ambient air	50
3.3.1.6.2 Radiation from receiver to reflector and sky	52
3.3.2 Thermal loss coefficient	55
3.3.3 Useful heat gain and thermal efficiency	56
3.4 Model validation	57
3.5 Performance parameters	61
3.6 Summary	69

CHAPTER 4	70
THERMAL ANALYSIS OF SYSTEM COMPONENTS	70
4.1 Introduction	70
4.2 Analysis of water preheating tank	70
4.3 Analysis of cooking pot	74
4.3.1 Description of cooking mechanism	75
4.3.2 Thermal modeling of cooking	76
4.3.3 Heating process of mixture (Sensible heat gain)	77
4.3.3.1 Mass transfer by evaporation	78
4.3.3.2 Energy transfer to process-water	79
4.3.4 Cooking process of mixture (Latent heat gain)	82
4.3.4.1 Transition from subcooled boiling to saturated boiling	82
4.3.4.2 Mass diffusion into wheat grains	85
4.3.4.3 Condensation heat transfer	85
4.3.5 Heat loss to surroundings	88
4.3.6 Mass transfer by flash evaporation	89
4.3.7 Mass balance of water	89
4.3.8 Cooking load	90
4.4 Analysis of brazed plate heat exchanger.....	91
4.4.1 Thermal analysis	92
4.4.2 Effectiveness-NTU method	94
4.5 Analysis of thermal expansion tank	98
4.5.1 Volume expansion	99
4.5.2 Heat loss analysis	100
4.6 Analysis of pipe field	104
4.7 Analysis of solar field	105
4.8 Summary	106

CHAPTER 5	107
EXPERIMENTAL STUDY ON SOLAR ASSISTED COOKING SYSTEM	107
5.1 Introduction	107
5.2 System description	108
5.2.1 Experimental setup of SAPH application	108
5.2.2 Measurement devices	111
5.2.3 System arrangement	112
5.3 Methodology	113
5.3.1 Preparation of materials	113
5.3.2 Heating of loops	115
5.3.3 Cooking operation	117
5.3.4 Performance parameters	119
5.3.4.1 Useful heat gain	119
5.3.4.2 Thermal efficiency	119
5.3.4.3 Utilization ratio	119
5.3.4.4 Overall system efficiency	120
5.4 System operation	120
5.5 Performance tests	125
5.6 Model validation for system components	127
5.7 Design aspects for cooking pot	128
5.7.1 Annulus type	128
5.7.2 Externally coiled type	131
5.8 Summary	133
CHAPTER 6	135
SYSTEM ANALYSIS	135
6.1 Introduction	135
6.2 Transient analysis	135

6.3 System operation	135
6.4 Simulation results	136
6.5 Summary	139
CHAPTER 7	140
CONCLUSIONS AND RECOMMENDATIONS	140
REFERENCES	144
APPENDIX	156
Appendix A: Thermophysical Properties of Heat Transfer Fluid (Renolin therm 320)	157
Appendix B: Thermophysical Properties of Air	158
Appendix C: Thermophysical Properties of Water	159
Appendix D: Technical Specifications of Pipe Materials	160
Appendix E: Technical Specifications of Insulation Materials	161
Appendix F: Flowcharts of Program Algorithms	162
Appendix G: Evaporating Liquid – Basic Theory	167
Appendix H: Curriculum Vitae	175

LIST OF TABLES	Page
Table 3.1. Characteristics of Smirro300	25
Table 3.2. Parameters for equation (3.16)	37
Table 3.3. Miscellaneous factors	38
Table 3.4. Constants for equation (3.55)	51
Table 3.5. Specifications for SEGS LS-2 parabolic trough solar collector test	58
Table 3.6. Comparison between SNL experimental data and the current model: Vacuum intact	59
Table 3.7. Comparison between SNL experimental data and the current model: Lost vacuum	59
Table 3.8. Comparison of RMSE among the model studies	61
Table 4.1. Specifications of the WPT	71
Table 4.2. Specifications of the IHHE	77
Table 4.3. Technical specifications of the BPHE	94
Table 4.4. Constants for equation (4.87)	102
Table 5.1. Properties of wheat used in experiments	114
Table 5.2. Variation in grain moisture content	115
Table 5.3. Model prediction for heat transfer area of the IHHE	127
Table 5.4. Model prediction for fluid outlet temperatures of the BPHE	127
Table 5.5. Properties of parboiled wheat after cooking operation for IHHE	128
Table 5.6. Specifications of the AHE	129
Table 5.7. Properties of parboiled wheat after cooking operation for the AHE.....	131
Table 5.8. Specifications of the EHHE	131
Table 5.9. Properties of parboiled wheat after cooking operation for the EHHE ...	133
Table 6.1. System parameters used in simulation	137

LIST OF FIGURES	Page
Figure 1.1 World energy consumption by fuel type	2
Figure 1.2 Global solar process heat applications in operation	3
Figure 1.3 Production of bulgur in Turkey by year	4
Figure 1.3 Bulgur production in Turkey by cities	5
Figure 2.1 Solar IPH system design process	18
Figure 2.2 Preliminary design steps	19
Figure 3.1 Schematic representation of Smirro300	25
Figure 3.2 Attenuation of solar radiation through the atmosphere	26
Figure 3.3 Motion of the earth about the sun	26
Figure 3.4 Tracking mode for PTSCs	27
Figure 3.5 Sun angles: ϕ , ω , δ	27
Figure 3.6 Solar zenith angle, θ_z , solar azimuth angle, α_s and solar altitude angle, α at the observer's coordinate system on the earth surface along with unit vectors i , j , k along their respective axes	29
Figure 3.7 Total spectral reflectance of MIRO-SUN	31
Figure 3.8 Transmission of DURAN glass	33
Figure 3.9 Refraction of beam radiation over the receiver tube	34
Figure 3.10 Heat transfer analysis for a differential control volume in the receiver .	40
Figure 3.11 Resistance network applied for the cross-section of the receiver tube ...	41
Figure 3.12 Support bracket and retainer	49
Figure 3.13 Network of the enclosure consisting of four surfaces	53
Figure 3.14 Comparison of thermal efficiency with SNL data and the other models	60
Figure 3.15 Comparison of thermal losses with SNL data and the other models	60
Figure 3.16 Heat gain and lost components for the collector	62

Figure 3.17 The effect of the optical parameters on the optical loss	63
Figure 3.18 Temperature profiles in the receiver tube	64
Figure 3.19 Heat loss components of the receiver tube	65
Figure 3.20 Variation of thermal efficiency under different annulus conditions	65
Figure 3.21 Effect of mass flowrate on thermal efficiency	66
Figure 3.22 Effect of HTF type on thermal efficiency	67
Figure 3.23 Effect of wind speed on thermal efficiency	68
Figure 4.1 Water preheating tank	71
Figure 4.2 Progress of the gelatinization of the hard wheat starch at different cooking temperatures	76
Figure 4.3 CP with internally helicoidal heat exchanger (IHHE).....	77
Figure 4.4 Variation of friction factor with Re in the region of puffs	79
Figure 4.5 Geometry of the IHHE	80
Figure 4.6 Typical boiling curve for water at 1 atm pressure	83
Figure 4.7 Condensation heat transfer in the presence of a noncondensable gas in quiescent mixture at $T_{\infty} = 100^{\circ}$	87
Figure 4.8 Exploded view of the BPHE	92
Figure 4.9 Schematic view of the plate	93
Figure 4.10 Thermal losses from TET in vertical position	100
Figure 4.11 Thermal inertia analysis of pipe header	104
Figure 4.12 Nodal analysis of PTSC array	105
Figure 5.1 Experimental layout of the SAPH application	109
Figure 5.2 Test setup of the SAPH application	110
Figure 5.3 Gelatinization of starch induced by water and temperature	114
Figure 5.4 Temperature profile and thermal power for the PL	116
Figure 5.5 Temperature profile for the SL	116
Figure 5.6 Temperature variations in the system components	118
Figure 5.7 Variation in the useful heat gain	121

Figure 5.8 Variation of the beam radiation and thermal efficiency	121
Figure 5.9 Variation in the discharged/transferred power, cooking load and auxiliary heating	123
Figure 5.10 Variation in the utilization ratio and overall system efficiency	124
Figure 5.11 Test results of the experiments performed in September 22, 2013 (Left column), September 25, 2013 (Right column)	126
Figure 5.12 CP with AHE	129
Figure 5.13 Temperature variation for the AHE during cooking operation	130
Figure 5.14 CP with EHHE	132
Figure 5.15 Temperature variation for the EHHE during cooking operation	133
Figure 6.1 Monthly average beam radiation data used for simulation	136
Figure 6.2 Variation of solar fraction with respect to months	137
Figure 6.3. Simulation results for the days in June 15, 2012 (First row); August 15, 2012 (Second row); October 15, 2012 (Third row)	138

NOMENCLATURE

A	cross-sectional area, m^2
AST	apparent sun time, min
BOD_5	Biochemical oxygen demand, mg/l
c_p	specific heat capacity, $J/kg^\circ C$
D	diameter, m
DST	daylight savings time, min
E	equation of time, min
f	focal distance, m; friction factor
g	gravitational acceleration, m/s^2
h	convection heat transfer coefficient, $W/m^2^\circ C$
H	height, m
h_{fg}	enthalpy of vaporization, J/kg
I	total radiation, W/m^2
I_b	beam radiation, W/m^2
I_d	diffuse radiation, W/m^2
J	radiosity, W/m^2
k	thermal conductivity, $W/m^\circ C$
K	extinction coefficient, m^{-1}
k_{eff}	effective thermal conductivity, $W/m^\circ C$
k_{std}	thermal conductivity of annulus gas at standard condition, $W/m^\circ C$
L	thickness of glass cover, m; length, m
l_a	parabola length, m
L_c	characteristic length, m
L_{loc}	local meridian, $^\circ$
L_{st}	standard meridian, $^\circ$
LST	local sun time, min

m	mass, kg
M_g	molecular weight of gas, kg/mol
M_s	molecular weight of solid, kg/mol
\dot{m}	mass flowrate, kg/s
p	perimeter, m
P	pressure, Pa
\dot{Q}	rate of heat transfer, W
\dot{Q}_d	rate of discharged energy, W
Q_r	rejected heat, J
\dot{Q}_u	useful energy gain, W
r_r	rim radius, m
S	curve length of parabola, m; absorbed solar energy, W/m ²
t	time, sec; thickness, m
T	temperature, °C
T_a	ambient temperature, °C
T_{bulk}	bulk mean fluid temperature, °C
U	overall heat transfer coefficient, W/m ² °C
U_L	thermal loss coefficient, W/m ² °C
u_m	mean velocity, m/s
V	volume, m ³
w_a	parabola aperture, m

Greek letters

α	absorptivity; inclination angle, °
α_n	normal absorptivity
β	chevron angle, °; volume expansion coefficient, 1/K
γ	intercept factor; specific heat ratio
Γ	end-effect
Δ	increment
δ	declination angle, °

ε	emissivity
ε'	miscellaneous factor
ζ	shading factor
η_o	optical efficiency; overall efficiency
η_{PTC}	efficiency of parabolic trough collector
η_t	thermal efficiency
θ	incidence angle, °
θ_z	zenith angle, °
κ	end-effect correction
λ	wavelength, m
μ	dynamic viscosity, kg/m·s
ν	kinematic viscosity, m ² /s
ρ	reflectance of parabolic mirror; density, kg/m ³
σ	total reflected-energy standard deviations at normal incidence; surface tension, N/m
τ	transmissivity
φ_r	rim angle, °
ϕ	latitude, °; enlargement factor; utilization ratio; relative humidity
ω	hour angle, °

Dimensionless

De	Dean number
C	concentration ratio
F	view factor
F_R	heat removal factor
Gr	Grashof number
He	Helical number
Kn	Knudsen number
n	refractive index
Nu	Nusselt number
Pr	Prandtl number
Re	Reynolds number

Re_c	critical Reynolds number
Ra	Rayleigh number
r_{\perp}	perpendicular component of unpolarized radiation
r_{\parallel}	parallel component of unpolarized radiation
Sh	Sherwood number
Sc	Schmidt number
W	moisture content
x_a	air mass fraction

Subscripts

1;2	medium number; loop number
<i>a</i>	absorber; aperture; absorbed
<i>ac</i>	between absorber and cover
<i>air</i>	ambient air
<i>an</i>	annulus
<i>b</i>	boiling
<i>c</i>	cover; critical; condensation; characteristic; cold
<i>cond</i>	conduction
<i>conv</i>	convection
<i>cp</i>	cooking pot
<i>ev</i>	evaporation
<i>ex</i>	exit
<i>f</i>	film; flashing
<i>g</i>	grain; gas
<i>h</i>	hot
<i>HTF</i>	heat transfer fluid
<i>i</i>	inner
<i>ia</i>	inside of absorber
<i>ic</i>	inside of cover
<i>in</i>	inlet
<i>ins</i>	insulation
<i>l</i>	liquid

<i>loss</i>	loss
<i>m</i>	mixture
<i>o</i>	outside
<i>oa</i>	outside of absorber
<i>oc</i>	outside of cover
<i>out</i>	outlet
<i>p</i>	preheater; pipe
<i>pw</i>	process-water
<i>rad</i>	radiation
<i>r</i>	retainer
<i>s</i>	surface
<i>sat</i>	saturation
<i>sky</i>	sky
<i>t</i>	tank
<i>v</i>	vapor
<i>w</i>	water; wall

Abbreviations

AHE	Annulus Heat Exchanger
BPHE	Brazed Plate Heat Exchanger
CHE	Coiled Heat Exchanger
CP	Cooking Pot
CSP	Concentrating Solar Power
EES	Engineering Equation Solver
EHHE	Externally Helicoidal Heat Exchanger
HTF	Heat Transfer Fluid
IHHE	Internally Helicoidal Heat Exchanger
IPH	Industrial Process Heat
kW _{th}	Kilowatt thermal
MW _{th}	Megawatt thermal
NTU	Number of Transfer Unit
PHE	Plate Heat Exchanger
PL	Primary Loop

PTSC	Parabolic Trough Solar Collector
RMSE	Root Mean Square Error
SAPH	Solar Assisted Process Heat
SEGS	Solar Electric Generating Systems
SHIP	Solar Heat for Industrial Processes
SL	Secondary Loop
SNL	Sandia National Laboratory
TES	Thermal Energy Storage
TET	Thermal Expansion Tank
WPT	Water Preheating Tank

CHAPTER 1

INTRODUCTION

1.1 Background and motivation

By 2010, fossil fuels comprise approximately 84.1% percent of world energy use [1]. World energy consumption is projected to grow by 56% between 2010 and 2040 as shown in Figure 1.1. Factors such as rising growth of energy demand, depletion of fossil fuels, energy security, and greenhouse gas emissions are forcing us to ensure a sustained energy policy with alternative ways. Renewable energy sources are appealing the energy market remarkably for the concerned issues. Renewable energy is growing fastest relative to the other energy sources with an increasing rate of 2.5% per year. Growth in renewable energy use from 2010 to 2020 is at the level of 3.7% per year [1], it is higher than the growth rate of world total primary energy supply (TPES). In 2010, 13% of total primary energy use was supplied from renewable energy sources of which 11.4% is utilized in industrial fields [2]. Further, the share in growth of solar thermal grew at an average annual rate of 10.2%.

Solar energy is a kind of renewable energy source and used in a variety of applications that can be collected in four main groups; concentrating solar power, industrial process heat, commercial and residential usages. Although many applications focus on solar electric generation, industrial use of solar energy has been gathering affinity in recent years. Solar heat for industrial processes (SHIP) applications has been maturing, and increasing numbers of SHIP systems have been installed and experienced in the past decade. In 2007, about 90 SHIP applications with a total installed capacity of 25 MW_{th} (Megawatt thermal) were reported to be in the study made upon 21 countries [3]. Most of these plants were small-scale and experimental based. However a number of promising projects have been realized

in recent years ranging from small-scale demonstration plants to very large systems. By the end of 2014, the number of installed plants reached 124 to be in operation all over the world with a cumulated capacity of over 93 MW_{th} (133,200 m²) [4]. The final conditions of the SHIP applications are demonstrated in Figure 1.2. Although companies and public institutes paid attention to commercialize solar technology in industrial areas, especially in the past quarter, it was not achieved satisfactorily. Since high investment cost, price escalation of fossil fuels, unavailability of convincing government incentives, and certain drawbacks of using solar energy became major barriers for the growth of the technology [5]. However, by the improvements in the solar collector technology, the prices of collector systems and their payback periods were reduced relatively. As a result, the number of installed systems was apparently increased and appeared to attract many fields of industries as in [6–8].

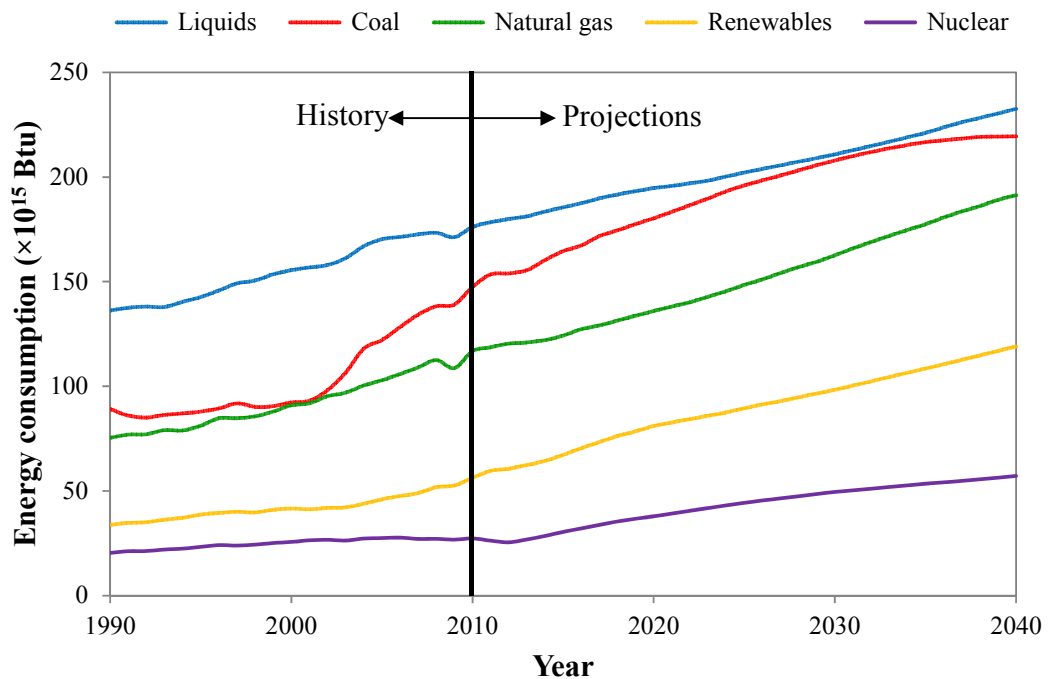


Figure 1.1. World energy consumption by fuel type.

Industrial heat requires various levels of temperature demand. High temperature (over 400°C) dominates 43% of the total demand, low (below 100°C) and medium temperature (between 100–400°C) demands corresponds to 30 and 27%, respectively [9]. Approximately 45–65% of the total energy involved for IPH is used in the preparation and treatment of goods. A number of studies on industrial heat-demands

for several sectors have been identified with favorable conditions for the application of solar energy [10]. The temperature levels for these applications range from 60°C to 260°C. The major portion of the industry, about 60%, uses process heat with temperatures below 250°C [11]. Most of the processes concentrate on the food and textile industry for diverse applications such as drying, cooking, cleaning, extraction and many others. A great number of the food processes are performed by the operation temperature of lower than 100°C thus the food industry has a great potential for the use of solar energy. Yet a significant part of these applications are situated at temperature levels between 100–250°C [12].

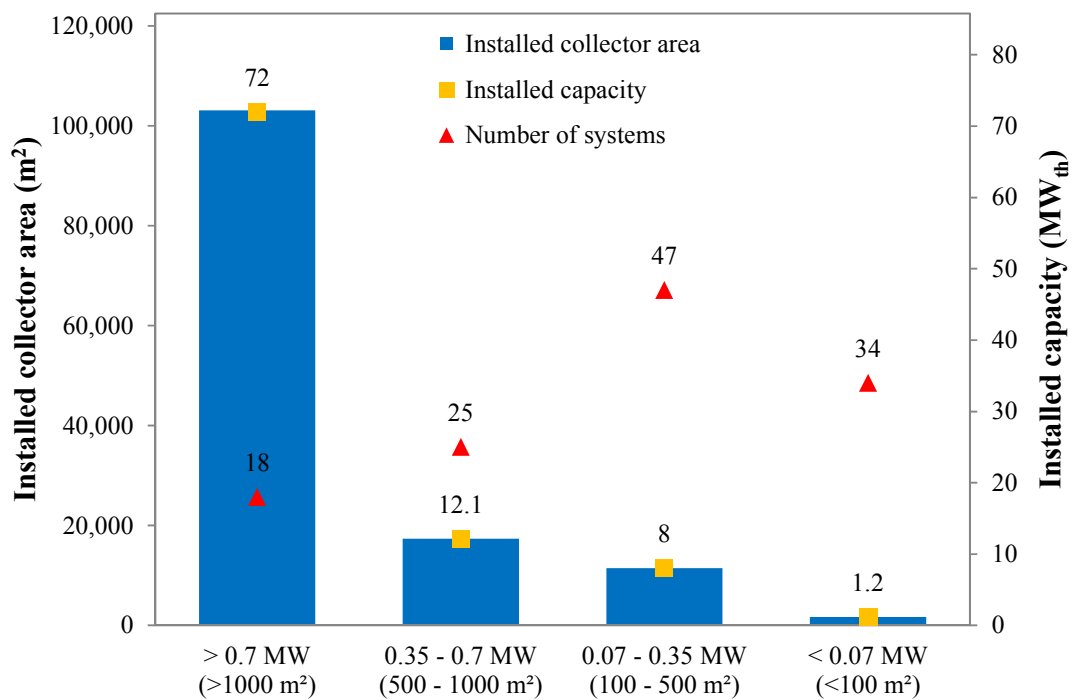


Figure 1.2. Global solar process heat applications in operation [4].

Most industrial factories supply thermal energy demand for their process heat applications from a heating system (generally steam boiler, fuel-oil or gas fired boiler) which uses fossil fuels as a heat source. Cooking process of cereals products is generally realized at moderate temperatures (between 90–120°C) and requires relatively substantial thermal energy demand. Typical steam temperature generated from these systems for food processing generally ranges from 105 to 200°C. Line-focusing solar systems appear very promising for these types of process heat applications at moderate temperature levels. Use of tracking concentrated solar collectors provides remarkable advantages at this temperature interval with respect to

the stationary solar technologies due to having relatively high thermal performance and low thermal loss [13]. These thermal requirements can be justified favorably by the recent improvements in the field of parabolic trough design. Parabolic trough solar collectors (PTSCs) have relatively lower energy cost in comparison to the other line-focusing solar collector systems. Heat costs for PTSC range from 0.04 €/kWh to 0.08 €/kWh depending on the operating process temperature and elevated solar radiation levels [14]. Although these energy costs are not satisfactory to be able to compete economically with cheaper fossil fuels without need of public subsidies, it is believed that further researches will bring the solar technology to an economically appealing status. For now, the most feasible way seems to use large-scale solar systems which lead to very low cost systems or to design systems without thermal energy storage (TES). The payback period of a process heat application can be shortened comparatively by using the former however the system without TES may not be cost effective for full-time daily operation [10]. Present investment costs for solar thermal systems range from 250 to 500 €/m² (corresponding to 250–1000 €/kW of thermal power) leading to average energy costs in Southern Europe from 0.02 to 0.05 €/kWh for very low temperature applications and from 0.05 to 0.15 €/kWh for medium temperature systems [7].

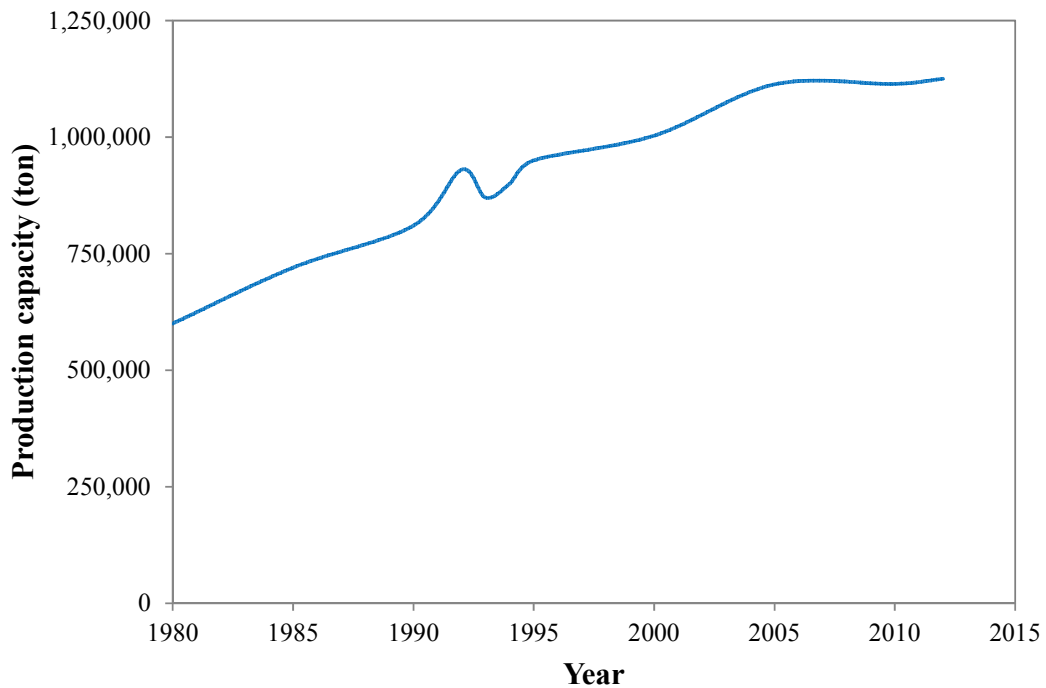


Figure 1.3. Production of bulgur in Turkey by year. (Source: Turkish Statistical Institute, Istanbul Chamber of Commerce, and Istanbul Commodity Exchange).

Turkey's developing economy and increasing targets includes agriculture and agricultural industries as well. Gaziantep is the one of the industrial city in Turkey with its five organized industrial zones (OIZ), and allocated by 755 companies are currently active with a number of employees of about 100,000. 43% of those companies are in textile, 22% in food, 9% in chemistry, 7% in plastics, and the remaining is active in other sectors [15]. Process heat usage is greatly wide for the mentioned sectors. 27% of the companies located in Gaziantep (including OIZ) are in food processing sector. According to the recent data, 362 small medium size food production companies are located in Gaziantep. Food industry is the second largest sector after textile. Especially in bulgur production, 40% of the bulgur processed in Turkey is produced in Gaziantep.

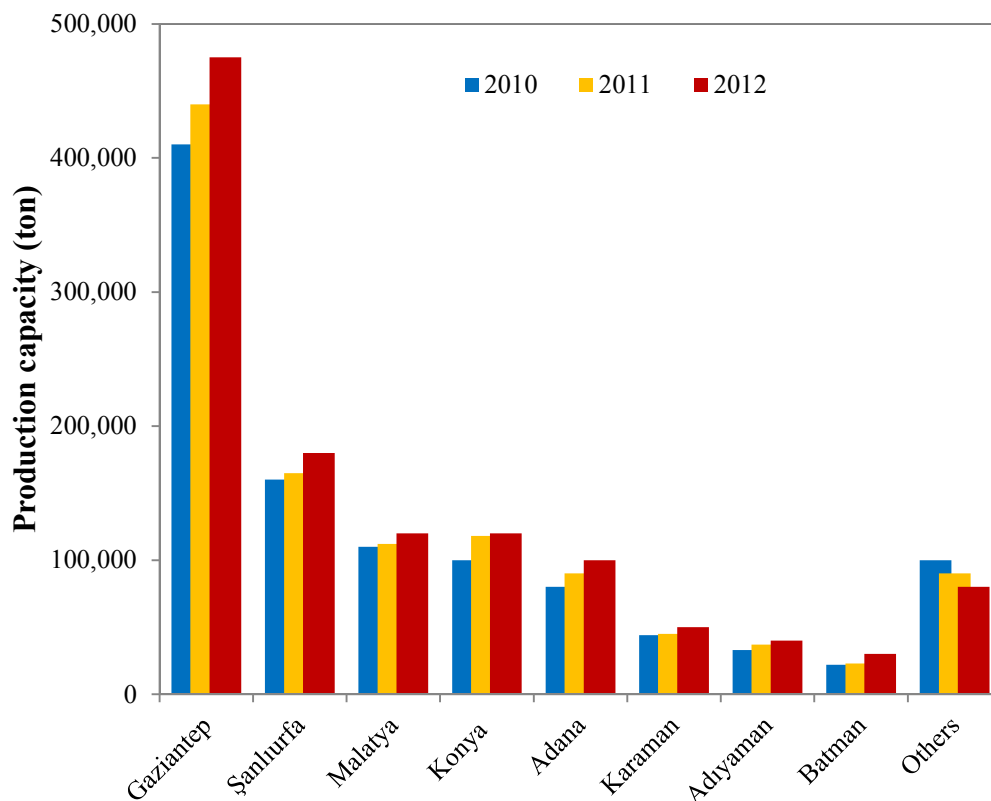


Figure 1.4. Bulgur production in Turkey by cities. (Source: Gaziantep Chamber of Commerce, Gaziantep Commodity Exchange, Gaziantep Chamber of Industry, Şanlıurfa Chamber of Commerce, Malatya Directorate of Provincial Food Agriculture and Livestock, Adana Chamber of Commerce, Adıyaman Chamber of Commerce, Batman Chamber of Commerce, Konya Commodity Exchange, Karaman Chamber of Commerce, Turkish Grain Board (TMO), Ankara Chamber of Commerce, Ankara Directorate of Provincial Food Agriculture and Livestock, 2012).

Production of bulgur in Turkey has been increasing regularly since 1980 with an average annual increment of 2.5% as seen Figure 1.3. There were about 500 bulgur

producers in Turkey, 20 in the United States of America (USA) and Canada, 6 in the European Union (EU) and 15 in the Middle-East [16]. Today, this number has been decreased nearly to 120 for Turkey because of modernization and increase in the production capacities of plants. The production capacities in respect of the cities of Turkey are shown in Figure 1.4. Annual bulgur production capacity in Turkey is sailing around 1,125,000 million tons, followed by American continent with a capacity of 300,000 tons. Due to increase in the market demand, European and Middle East companies have started to construct new bulgur factories with production capacities of 80,000 and 120,000 tons, respectively [16]. It is inferred that Turkey is the biggest bulgur producer in the world and exports annually above 120 million \$ to other countries [17].

1.2 Aim and objectives

Bulgur is basically produced from hard wheat (*Triticum durum*) using cooking, drying, debranning, cracking and classification steps. Cooking and drying processes require remarkable quantity of thermal energy which is met from fossil fuels or its derivatives in industrial bulgur plants. About one-third of the energy used in drying is driven by the cooking operation [18]. The market enlargement entails cost reduction to increase the production capacity. In order to reduce the energy costs of the process, either new methods or alternative ways are needed.

In this study, it is focused on the enhancement of the energy efficiency of the cooking facility, and the reduction of production costs by using solar energy. Because solar energy is a renewable source which offers to be utilized freely. Industrial applications are conducive to cost-effective solar implementation. Unlike solar heating or cooling of buildings, industrial process loads occur mostly during the day and are fairly constant throughout the year; therefore, it is possible to use industrial solar systems year-round [19]. This is especially important during the summer months when solar energy is most available. Little or no storage is required for daytime loads, which reduces the initial investment. Moreover, the solar system can be tailored to provide energy at the temperature required by the process. For these reasons, solar energy is thought to be a promising source for this issue as its potential is high and being integrated with the regarding IPH process. Nevertheless,

it is useful to conduct a preliminary work to determine whether the integration of a process heat application to conventional thermal system using solar energy is feasible or not. Thus, an experimental research has been carried out on solar assisted process heat (SAPH) application using PTSC array for cooking wheat to produce bran-free parboiled wheat. Wheat crops are harvested seasonally from the end of May through August in Turkey, and the production capacity of bulgur is increased especially in spring and summer seasons although bulgur plants produce bulgur through the whole year. In these seasons, the energy potential of solar reaches high levels in Gaziantep that locates at southeastern of Turkey. Therefore, a pilot study was performed for analyzing the technical feasibility of a process-heat application assisted with solar energy for cooking facility at moderate temperatures. A test setup was installed to evaluate the performance and the energy efficiency of the system with respect to conventional cooking systems. Thermal and mathematical models of the system components used in the experimental setup were established, and the annual solar contribution supported to the SAPH application was analyzed by simulating it transiently under real-time conditions.

1.3 Outline of the thesis

This dissertation is composed of seven chapters with an introductory chapter.

Chapter 2 addresses the most updated research and development status for SHIP so as to fully appreciate the latest findings and key challenges available in the literature. It presents the studies on SHIP applications, the progressions in SHIP projects to be applied, and the design methodologies for SHIP applications.

Chapter 3 introduces modeling of PTSC and simulation of its performance parameters under different conditions. Optical and thermal analyses of PTSC are performed in detail. Furthermore, the model validation for the developed heat transfer model is included.

Chapter 4 presents the methodologies for thermal analysis for each component of the SAPH system which includes cooking pot (CP), brazed plate heat exchanger (BPHE), thermal expansion tank (TET), pipe installations and receiver tube of PTSC.

Physical insight of cooking phenomena is described in detail, and the mathematical modeling of cooking process is carried out.

Chapter 5 presents the experimental setup for the designed SAPH system and describes the materials and experimental methodology for the research. The experimental tests performed under different operating conditions are presented. The test results obtained from experimental studies are analyzed for technical restrictions and system performance. The performance tests of three different CPs being designed are introduced.

Chapter 6 presents the outputs of the transient simulation program for analyzing the SAPH application under the given system parameters. Variation in the solar fraction with respect to calendar months is analyzed, and the annual system performance of the SAPH application is obtained.

Chapter 7 implies the crucial points based on the conclusions drawn at the end of each chapter and the suggestions for the further researches.

CHAPTER 2

LITERATURE REVIEW

2.1 Introduction

Since the 1980's, a noticeable number of SHIP systems have been designed, installed and operated. However some of them were shut down or deactivated due to different reasons. Nevertheless increasing numbers of SHIP plants were constructed around the world in the past decade. Along with increasing in the projects, a growing awareness of being installed SHIP systems has attracted the federal and national agencies to fund the research programs. In this section, the most updated research and development status for SHIP is addressed so as to fully appreciate the latest findings and key challenges available in the literature. The studies on SHIP applications, the progressions in SHIP projects to be applied, and the design methodologies for SHIP applications are presented in detail at the following sections.

2.2 Applications on solar-integrated industrial process heat

Many attempts have been put the plan into action to integrate solar heat for IPH applications since the mid-1970s. Especially in the past decade, increasing number of SHIP projects were implemented and experienced. The status of the existing SHIP plants throughout the world has been overviewed in the online database formed [8] under the framework of the IEA Task 49/IV. Furthermore, the plants being installed previously and operating currently all around the world were extensively represented in this part.

Kutscher et al. [5] presented the solar industrial process heat field projects funded by the U.S. government. A list of these projects supported within the scope of this

program was experienced for a various applications demanding hot water (<100°C); hot air; low-temperature steam (100–177°C); and intermediate-temperature steam (177–275°C). Six of the field tests performed were given in the study for solar thermal applications mainly used in industry, namely, process hot water, drying/dehydration and process steam.

Schweiger et al. [6] summarized the results of the POSHIP project funded by the European Commission within the 5th Framework Program. In the project, potential for solar heat in industrial processes at medium temperature level was analyzed for Spain and Portugal. The status of the SHIP projects existing in Europe and USA was given in a list which involves the general information about the projects.

The SHIP applications existing in the Mediterranean region were overviewed by the study reported [7]. In this report, examples for installed plants were given, and experiences gained from these applications were discussed. One of the examples is related to the plant installed in Spain for the washing process of containers used for transport sector. Hot water at 70–80°C is required to meet the daily capacity in the range of 70–80 m³. The solar thermal system is composed of flat-plate collectors of around 500 m², representing a total installed capacity of 357 kW_{th} (Kilowatt thermal), and a storage system of 45 m³. Additionally, a gas-fired steam boiler is installed for the preparation of hot water as back-up. In 2001, a dairy process was integrated with the flat-plate collector field having total collector area of over 1000 m² (706 kW_{th}) and the existed 50 m³ heat storage system to feed the sanitary hot water network of the company in Greece. A LPG (liquefied petroleum gas) fired boiler was installed as back-up. The solar system was designed to cover 80% of the load during the summer period. The payback period of the investment is expected less than 3 years. Another SHIP plant was installed at Italy in 2008 for pre-heating processes (heating of emulsions and factory building) of a cosmetic company. The solar field is composed by 90 m² (63 kW_{th}) of flat-plate collector, and also a heat storage with a tank capacity of about 5 m³. The system was integrated to the existing natural gas fired boilers. In the 1990's, two pilot SHIP plants (food and textile industries) were commissioned in the Egyptian industry within the program of “Solar Industrial Process Heat and Waste Heat Recovery System”. Both projects were composed of 350 m² of locally manufactured flat-plate collectors to produce 26

m³/day of hot water at 50–60°C however they were deactivated in 2005 due to specific reasons. In Turkey, a PTSC solar field was implemented into a process heat application available in a hotel. 180 m² of collector area were used for this application to provide hot water for laundry and space heating. Though the application is not particularly a SHIP application, it can be accounted as a commercial application. Another project was carried out in Jordan for the process of dissolving powder milk. 128 m² flat-plate collector and 5 m³ storage tank were used in the plant to obtain hot water in a temperature range of 40–60°C.

Thomas [20] installed a solar steam generation system using parabolic trough concentrators having 192 m² of collector area to generate steam to be used in several processes at the printing section of the Government Silk Factory in India. The performance of the system was continuously monitored in April, and the average daily collector and system efficiency were obtained as 45–53% and 33.5%, respectively.

An advanced control system was developed by Köhne et al. [21] for the operation of solar process heat plants and a simulation program. A flexible test facility TESOP, consisting of different small collector fields, two storage tanks, an auxiliary electric heater and an adjustable heat sink for simulating any load profile, was installed in order to qualify the control system and the simulation model. It was concluded that suitable and sufficiently fast control system was essential for the operation of solar process heat plants with optimized operation strategy to match the temperature requirements of load processes properly. TRNSYS simulation program was used for modeling, long-term testing under realistic conditions and design of solar process heat plants.

Nagaraju et al. [22] presented an industrial model solar water heating system which was designed and installed to heat and supply 110,000 liters of hot water at 85°C per day for an egg powder making plant. 2560 m² of solar collector area and four thermally insulated hot water storage tanks (each having a capacity of 57.5 m³) were considered in the system design. Performance studies conducted on the whole system revealed that the annual net savings in furnace oil consumption is on the level

of 78%. It was concluded that this plant could be a role model for future applications, particularly in the food industry.

Eskin [23] analyzed the unsteady performance of a solar process heat application with cylindrical parabolic collector and storage tank by using the test results of IPH system established for a textile plant in Turkey. The test results of the system were validated by a simulation study.

Karagiorgas et al. [24] evaluated about ten solar thermal systems in Greece for the sectors of agrofood, textiles, chemicals and beverages in terms of economic view. Monitoring results from five installations for a typical day's operation were given in their work.

Bokhoven et al. [25] presented an operational experience of two large solar thermal systems in the Netherlands. One of them, consisting of 1200 m² high performance flat-plate collector array and 1000 m³ water storage tank, was installed for the purpose of agricultural drying and conditioning to meet the temperature requirement between 25–80°C. The other one was realized as a solar plant for industrial heat for a confectionery factory operating 5 days a week. 2400 m² collector area was utilized to provide a daily system load of 125,000 L of hot water at 65°C.

Krüger et al. [26] presented their operational experience for integration of the PTSC (108 m² collector area erected in 6 rows with each having two modules) to the steam line of the aluminum processing company located in German in order to produce saturated steam at 4 bar and 143°C. The study was also focused on the layout and monitoring results of the installation.

A mathematical model was developed by Abdel-Dayem [27] for El-Nasr pharmaceutical solar process heat project which was the largest industrial system installed and working in Egypt. It was simply constructed using one-axis tracking parabolic-trough having a total collector area of 1958.4 m² to produce saturated steam at 8 bars and 175°C for the industrial processes in the company. The mathematical model was developed for the system components to simulate annual performance of the system. The simulation results were verified successfully by the

measured data obtained from the monitoring of the system performance. The validated numerical model was performed for obtaining optimal collector area in terms of economical view. The optimal collector area was estimated 538 m² which is less than that of the installed.

Boutaghriout et al. [28] investigated the potentialities of natural gas saving in the dairy industry as a case study of agro food in Algeria. They performed an experimental study showing the potential of solar thermal energy at low temperatures that could be explored for the heating process using flat plat collectors.

Within the framework of the European FP7 Project InSun, the reliability and quality of large solar thermal collector fields including three different collector technologies (flat-plate, Fresnel or parabolic trough collectors) were demonstrated to produce industrial process heat at different temperature levels in different climatic regions. Pietruschka et al. [29] started European FP7 Project InSun using different types of collector systems applied to different industrial processes, each having a capacity of more than 1 MW: improved flat plate collectors for an Austrian meat factory for steam pre-heating up to 95°C, tracked concentrating Fresnel collectors for an Italian brick drying factory at 200°C and parabolic trough collectors for milk powder production at 185°C in Spain. Cotrado et al. [30] showed the monitoring data of a large scale solar plant installed in Austria to provide heat up to 90°C for the manufacture of meat products. A dynamic simulation of this plant was developed in TRNSYS considering technical information of the installed solar system and controlling provided by the cooperated company. Vittoriosi et al. [31] demonstrated the monitoring results of the solar field in a brick manufacturing process within the scope of FP7 project InSun. Solar heat was produced by Fresnel collectors with an overall area of about 2700 m² and a planned maximal capacity of 1.2 MW to provide thermal energy to the drying process of a brick company in Italy. The solar plant was composed of two different fields, one with direct steam generation (DSG) and the second with thermal oil as heat transfer fluid (HTF) used for indirect steam generation by means of an oil-to-water steam generator.

Frank et al. [32] evaluated the measurements on PTSC fields integrated into the solar process heat plants in Switzerland. The performance of the collector fields and

monthly evaluation of the energy delivery of the collector field were analyzed in April for two plants. The first plant (115 m² aperture area) in Bever, the collector field performance (the fraction of daily solar gains from total direct irradiation) reached values in the range of 45 % providing outlet temperatures of about 190°C. The second plant (630 m²) in Saignelegier yielded low collector field performance relative to the first plant due to having lower beam radiation level although the design temperature of this plant was about 125°C.

Lauterbach et al. [33] described the integration of a flat-plate collector array (155.5 m² aperture area) and storage tank (10 m³ capacity) into the hot water supply of a brewery plant. The system was analyzed based on the monitored data and the simulations developed in TRNSYS program. Furthermore, the operational experiences were identified and their influence on the system yield was evaluated. It was illustrated that the amount of available load had the highest impact on system performance since the load was reduced by manual interference, a substantially lower system yield was obtained compared to the expected one. The correct estimation of available load was crucial to predict the performance of a solar thermal system before installation. Additionally, global and local sensitivity analyses were carried out and the most important factors for system yield were identified as the process temperature, the choice of a suitable and well-functioning collector and the load profile.

Iglauer and Zahler [34] presented the technical details of the solar process heat system being integrated to the curing of autobody paint at 200°C for the company servicing to automobile manufacturing technology. The solar process heat generated by a Fresnel collector field was used to preheat the compressed combustion air of the micro gas turbine (used by a combined heat and power system) to be used in paint shop convection ovens along with electric power. The consumption of fossil fuels was expected to be reduced by up to 35% at nominal power by implementing the solar process heat into that IPH application.

2.3 Progress in solar-integrated industrial process heat

Potential studies on solar-integrated IPH applications are still proceeding in different regions of the world. This section focuses on the preliminary analysis and design strategies performed for these applications. Based on the search in the open literature, at first glance the following studies draw the attention.

Under the framework of the CDM mechanism, a solar plant providing steam for 8 fish-meals plants is considered to be installed in Morocco [7]. Fresnel and flat-plate collector fields will be connected to a back-up fuel oil system for producing steam and hot water. The maximum energy demand is estimated to be 6 MW for each plant. In Tunisia, PROSOL program has been extended for the development of solar heating systems in industrial sectors such as agro-food, textile, chemistry and paper mills [7]. Many feasibility studies have been made on the solar systems providing hot water or steam to those of industrial processes.

Frein et al. [35] presented the main analysis and design steps made for the integration of a solar thermal plant of 1000 m² into the dyeing process of industrial facility in Tunisia. This solar thermal demonstration plant is seen as an opportunity to realize a good practice example of solar thermal plant integration into industrial processes. This is why special care has been put on analyzing the actual process in order to choose the suitable integration of the solar plant, considering especially the investment costs issue.

Hafner et al. [36] provided insight into the status of the SolSteam project and the activities planned to develop a standardized solar-fossil fuel powered steam generation system (a fresnel collector field and a shell boiler) for industrial applications that is paving the way for a more sustainable production in sectors such as food, textile, pharmaceutical and many others.

In the framework of a European Union-funded demonstration project, three large-scale solar thermal systems (each with an installed thermal peak capacity ≥ 1 MW_{th}) are being realized. The scope of the project demonstrates the integration of large scale solar thermal systems on process level for different applications (mashing,

pasteurization of beer, drying of green malt) at process temperatures below 80°C. Mauthner et al. [37] presented technical solutions for the hydraulic integration of large solar process heat applications equipped with flat plate collectors for a direct heat supply to the thermally driven processes in the brewing industry commissioned at Austria, Spain and Portugal.

Silva et al. [38] studied the possibility of production of process heat steam for a food processing industry (devoted to vegetables preservation by thermal treatment and canning) with an unfired boiler configuration using a parabolic trough solar plant in Spain. The base solar plant configuration analyzed consists on a parabolic trough solar field, thermally stratified energy storage, and an unfired boiler to meet the total process heat annual consumption of 148 MWh by saturated steam at 7 bar. The influence of the main operational variables of the solar plant was studied, and the parameters affecting the performance of the industrial plant were obtained as the solar field outlet temperature and the unfired boiler return temperature.

An analytical feasibility study was performed by Eldean and Soliman [39] for the heating process of margarine melting using solar thermal power as an alternative energy source to lower the power consumption of their heating process. The efficiency and cost effectiveness of a PTSC solar field were compared to a steam boiler, and different configurations and the different working fluids were investigated.

2.4 Design approaches for solar process heat systems

Design stage is very critical for SHIP applications to obtain maximum yield while ensuring the minimum system cost and payback period. There are many design considerations that should be evaluated in this stage. Preliminarily, the application field of IPH is specified, and its suitability for solar integration is analyzed. Even if the type of industrial process appears similar in nature, the process requirements can be different from each other. Any IPH application may have distinct plant designs thus the IPH being applied should be configured by taking into account the plant design. In this section, the methodologies are presented in the literature introduced for designing SHIP applications.

Kutscher et al. [5] have prepared a design handbook from the experiences gained over 100 projects on solar heating and cooling (SHAC) of buildings and about a dozen projects on solar industrial process heat (IPH) systems installed in the USA. The content of this handbook has been arranged to guide the user through a system design using solar thermal energy in industry (see Figure 2.1). Furthermore, it provides how to choose the proper application and system configuration and how to estimate the amount of energy the solar system can be expected to supply. Moreover, a methodology is presented for choosing appropriate components such as collectors, storage, piping, insulation, pumps, valves, heat exchangers, and heat transfer fluids. System integration, controls, economics, start-up procedures and safety and environmental issues are addressed, and a new, simple method for predicting energy delivery is included. Consequently, all the guidelines are evaluated for designing, constructing, and operating of the solar thermal energy systems to shorten the time required for conceptual and preliminary design, which should, in turn, reduce total design costs.

Gordon and Rabl [40] have developed a design procedure for solar industrial process heat systems without storage that supply heat to a constant load. The method provides explicit algebraic equations including a quick procedure for selecting the most cost effective collector and calculation of pumping energy. The cost and performance penalties associated with storage of solar heat are avoided by proposing the backup operating at variable heating rate for the lowest possible cost. The economic optimum is shown to imply a slightly oversized collector field with dumping of excess energy during peak insolation.

Collares-Pereira et al. [41] have presented a new method for the design and optimization of solar industrial process hot water systems with day-night and/or weekend storage (i.e. constant load applications). The method proposes the single-pass open-loop design which operates at higher system efficiency than conventional system designs. Introducing the method may advantageously bring cost effectiveness while enabling the designer to reduce collector area without reducing the yearly useful energy delivered by the system. The results obtained are in the form of closed-form equations for calculating the net yearly useful energy delivered by a given system design and optimizing the collector area and storage size.

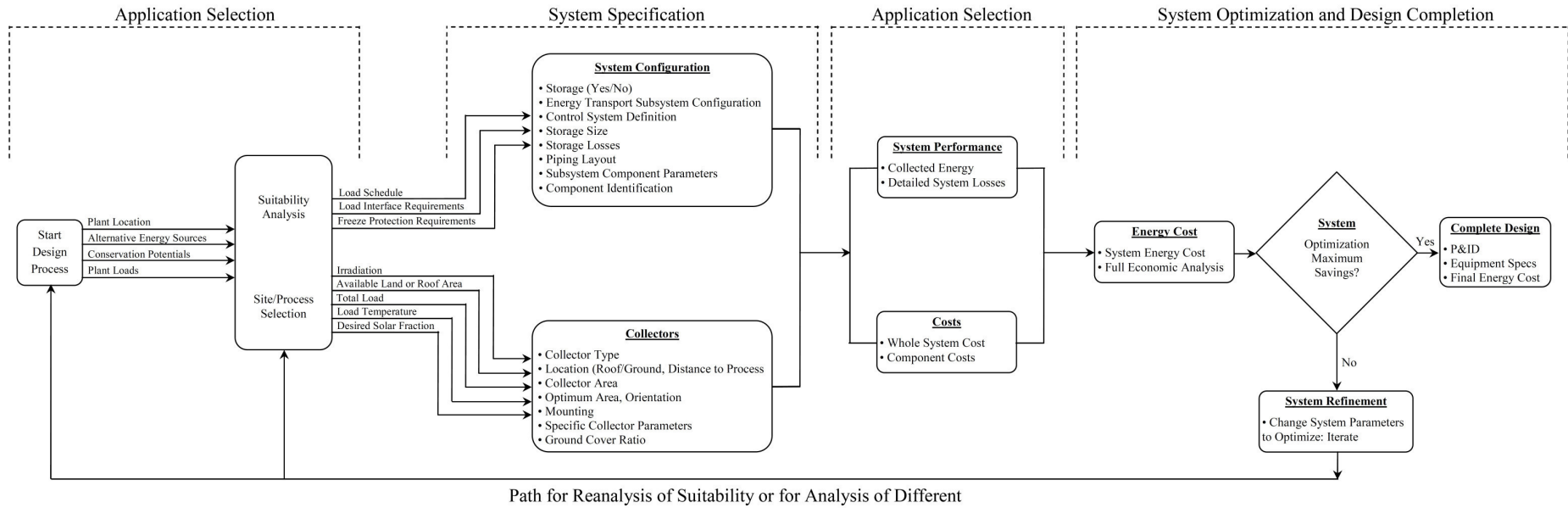


Figure 2.1 Solar IPH system design process [5].

Aidonis et al. [42] have published a brochure which involves the design and maintenance guidelines for the implementation of solar thermal systems coupled with industrial sectors using hot water with temperature requirements up to about 90°C. The brochure aims to present a technical background by the experience gained and also a methodology to analyze all common design aspects of solar thermal plants as shown in Figure 2.2. A simple tool called as *nomogram* is demonstrated for dimensioning a solar plant and the energy savings that correspond to certain solar fractions. Moreover, dimensioning of a solar plant as well as its optimum configuration is offered by a simulation program TSOL for simplified system configurations.

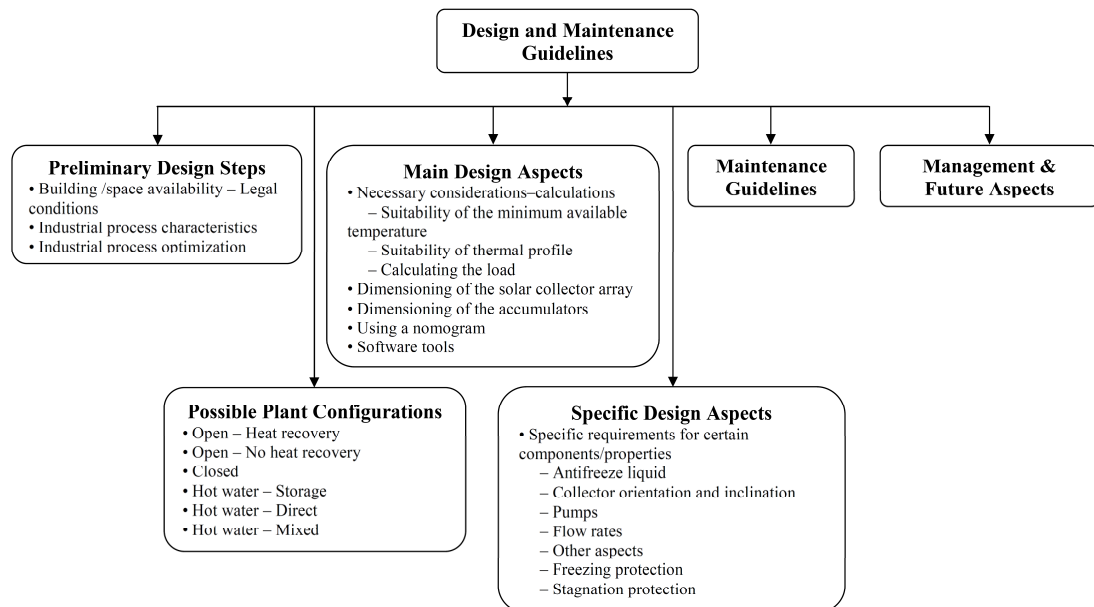


Figure 2.2. Preliminary design steps. Adapted from [42].

Kulkarni et al. [43] have introduced a design methodology based on the concept of *design space approach* in order to design and optimize concentrating solar collector based systems with pressurized hot water storage. The design space is the region bounded by constant solar fraction curves traced on the collector area vs. storage volume diagram and it represents all possible feasible design configurations subjected to different constraints such as existing collector area, limitations on available floor spacing, existing storage volume, or maximum allowable storage volume. The proposed design and optimization tool offers flexibility to the designer in choosing a system configuration on the basis of desired performance and

economy. The study shows also the possibility of applicability of the design space methodology to a variety of industrial process heat configurations in an effective way. However, the methodology has a deficiency since it requires initially the choice of a solar fraction which is always not a practical approach for solar process heat applications when the process constraints change.

2.5 Summary

Studies on SHIP applications have increased moderately but number of studies made until now is not satisfactorily enough. Since solar energy does not provide performance guarantee, generally used as supplementary source, and brings technical drawbacks. It requires higher initial cost whose return depends mainly on the system performance. Thus great diligence is showed in the design stage of SHIP applications. Most of the time design process of SHIP applications is time consuming and requires technical qualification for making appropriate system layout, optimization etc. There is no strict methodology followed in the design stage but it basically obeys the general rules of thermal system design. Although providing solar heat for IPH applications is cumbersome, the researches on them are increasing day by day. There are more practical studies rather than theoretical ones as the literature reviewed. However, applied studies differ from each other regarding their process requirements; process type, thermal load profile and storage. These are the main features that draw the boundaries of the SHIP application being designed. Other requirements can be justified by proper selection of system components and their integration for obtaining maximum possible system performance.

CHAPTER 3

MODELING OF PARABOLIC TROUGH SOLAR COLLECTOR

3.1 Introduction

In recent years parabolic trough solar collectors have gathered much more interest since they have remarkable advantages with respect to the stationary solar thermal technologies such as relatively high thermal performance and operating temperature. Such typical characteristics put them forward to be used in industrial process heat (IPH) and concentrating solar power (CSP) applications. There are currently several commercial PTSCs for CSP plants that have been successfully tested in a temperature range of 300–400°C. A number of projects for solar electric generating systems (SEGS) are currently under development or construction worldwide. Up to date, there are 20 active parabolic trough power plants, and 27 parabolic trough power plants are being constructed [44]. New SEGS plants concentrate on substantial technological progress in vacuum technology, selective surfaces, manufacturing processes, and improved materials. Additionally; a number of works have been carried out for reducing the cost of energy using advanced thermal energy storage techniques (such as storage in concrete medium and thermocline tanks), and for overcoming the limitations originated from the heat transfer fluid used. Although most of the PTSC applications focus on CSP, SHIP applications have been gaining momentum in the course of time as well. Currently, 124 SHIP applications are in operation with a total capacity of over 93 MW_{th} [4].

Along with increasing SHIP and CSP applications, necessarily have increased the researches on the PTSCs and their analyses. However, the thermal and/or mathematical analyses have been developed with either simplified approaches for a specified system [45,46] or more detailed ones. Simplified approaches save

considerable time of the analyst but they may not provide constantly to get consistent solutions particularly when the number of variables is high. On the contrary, more comprehensive and realistic analyses make possible to obtain more accurate results reflecting the nearest system characteristics of the PTSC. Thus making a detailed analysis shows the effective system parameters on the performance of the PTSC and provides us to apply it to the fronting studies relevant with thermal system design.

Many researchers presented energy models on parabolic trough collectors. When the studies conducted on detailed modeling of PTSC are handled, Edenburn [47] predicted the efficiency of a PTSC by using analytical methods for heat transfer modeling for evacuated and non-evacuated annulus. The results showed good agreement with data measured by Sandia National Laboratory (SNL) under the collector test setup. Kalogirou [48] studied the performance characteristics of the parabolic trough collector system and its analytical model equations. Odeh et al. [49] developed a simulation to evaluate the efficiency and the thermal losses of parabolic trough collectors for the case of synthetic oil and water usage. The most noticeable and broad models were established by Forristall [50] who developed both one-dimensional and two-dimensional heat transfer models of parabolic trough solar receiver implementing in Engineering Equation Solver (EES) and compared the models. The results indicated that the two-dimensional model provides a higher degree of accuracy than the one-dimensional model when evaluating long receivers greater than 100 m. Moreover, he investigated the effects of many collector parameters on the collector efficiency. The other study is of Jacobson et al. [51] who developed a solar parabolic trough simulation to determine the optimum parameters to sustain a solar thermal power plant system in Thailand. Garcia-Valladares and Velazquez [52] carried out detailed numerical simulations for thermal and fluid-dynamic behavior of single-pass and double-pass solar parabolic trough collectors. Another study was made by Qu et al. [53] who applied a model to the tubular receiver to improve the PTSC design and overall system performance. The model was verified by the experimental data taken from the tests of the PTSC system which was used for high temperature solar cooling and heating. Padilla et al. [54] performed a one-dimensional numerical heat transfer analysis, and an optical analysis to optimize the PTSC and understand its performance under different operating conditions. In order to validate the numerical results, the model was compared with

experimental data obtained from SNL and other one-dimensional heat transfer models demonstrating a better agreement with experimental data compared with the other studies. Huang et al. [55] proposed a new analytical model for optical performance to simulate the performance of a parabolic trough solar collector. Coccia et al. [56] described a mathematical model of a parabolic trough collector in detail and tested by comparing the efficiency predicted by the model with the efficiency measured through outdoor tests on a PTSC prototype. Another study of Kalogirou [57] was related with a detailed thermal model of a parabolic trough collector considering all modes of heat transfer. The model was written in EES and validated with known performance of existing collectors to be installed at the Cyprus University of Technology. Wirz et al. [58] modeled three-dimensional heat transfer in a parabolic trough solar concentrator system using Monte Carlo ray tracing, coupled to a finite volume solver. The computed heat losses and thermal efficiencies agreed well with experimental data. Silva et al. [59] developed a tri-dimensional non-linear dynamic model of a parabolic trough collector in Modelica and coupled to a solar industrial process heat plant modeled in TRNSYS. You et al. [60] analyzed the models of flow and heat transfer processes in a trough solar collector for the direct steam generation system. Dongqiang et al. [61] examined overall heat loss, end loss and thermal emittance of the coating of a newly designed receiver of PTSC in order to evaluate its thermal characterization. A series of heat loss tests were conducted for new receivers to evaluate the thermal performance in a newly developed test stand following the steady state equilibrium method. Hachicha et al. [62] developed a detailed numerical heat transfer model based on the finite volume method for the receiver element. Further, an optical model was made for calculating the non-uniform solar heat flux around the receiver using finite volume method and ray trace techniques. The optical model was compared with known analytical solutions, and the performance of the overall model was tested with the experimental measurements of SNL and other un-irradiated receiver results showing a good agreement but with some discrepancies. Ouagued et al. [63] evaluated the performance of a tracking PTSC using a heat transfer model developed under the topographical and climatic conditions. Marif et al. [64] developed a computer program based on one dimensional implicit finite difference method with energy balance approach in order to determine the optical and thermal performance of a PTSC under the climate conditions of Algerian Sahara. Mokheimer et al. [65] developed a computer

simulation code using EES to evaluate the optical and thermal efficiencies of PTSCs solar field considering average hourly, daily, monthly, or annually averaged weather data; in addition to detailed cost analysis of the solar field. Yılmaz and Söylemez [66] performed a comprehensive analysis to simulate the solar, optical and thermal characteristics of PTSC by introducing thermo-mathematical modeling. The developed thermal model was compared to the experimental data of SNL and yielded satisfactory results showing a pretty good consistency with respect to the other model studies. Finally, the model was applied to an existing PTSC module to analyze its performance characteristics under different operating conditions.

Although many modeling studies are available in the literature, numerous ones examine the parabolic troughs relating to their individual technical specifications and/or present different approaches for their modeling. All these attempts may help us to develop more consistent models and to implement them to new PTSC systems. In this study, a comprehensive thermo-mathematical analysis of PTSC was proposed and presented. Solar energy calculations for determining optical efficiency and useful heat gain supplied to a HTF were conducted for analyzing the thermal performance of the PTSC. The heat losses from the receiver were evaluated considering steady-state and one-dimensional heat transfer approach. In the performance analysis of the PTSC, the effects of optical efficiency, thermal losses, ambient conditions, and the state of receiver under different scenarios were investigated.

3.2 Parabolic trough solar collector system

3.2.1 System description

A PTSC basically is operated by a tracking mechanism which rotates the parabolic trough to orient toward the sun. The trough directs the sun's rays onto a tubular receiver, which absorbs and transfers the resulting thermal energy to a working fluid circulated inside the absorber pipe, aligned with the focal line of the trough. The absorber pipe is usually enclosed by a glass cover to reduce the heat losses since it operates at high temperatures. A schematic representation of a single PTSC module (Smirro300) and its technical specifications are given in Figure 3.1 and Table 3.1, respectively.

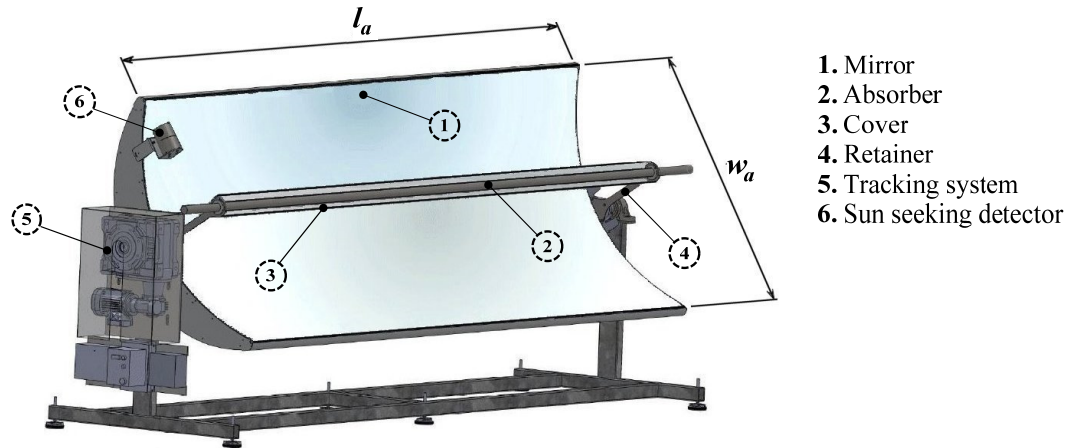


Figure 3.1. Schematic representation of Smirro300. Adapted from [67].

Table 3.1. Characteristics of Smirro300 [67].

Tracking mode	Single-axis
Parabola dimension, $l_a \times w_a$	3.00 m \times 1.14 m
Focal distance, f	0.358 m
Absorber diameter, D_{ia} / D_{oa}	0.032/0.035 m
Cover diameter, D_{ic} / D_{oc}	0.054/0.060 m
Cover emissivity, ε_c [68]	0.88
Mirror emissivity, ε_{ref} [68]	0.85
Absorber absorptivity, α_n [69]	0.95
Absorber emissivity, ε_a [69]	0.15
Absorber material	Selective coated stainless steel
Cover material	DURAN glass
Mirror material	MIRO-SUN
Annulus condition	Air filled

3.2.2 Solar radiation on tracking aperture

Solar radiation reaching the earth involves the direct (beam) and the indirect (diffuse) components. The solar radiation is partially reflected, scattered and absorbed in the atmosphere (see Figure 3.2) and the remaining is referred as the beam radiation which can be used as useful energy when it is manipulated by a concentrated collector system.

The emitted radiation from the sun has a directional characteristic that is defined by a set of geometric relations to determine the angle of incidence with respect to the receiver. Due to instant change in the position of the earth (Figure 3.3), the solar

angles and the incidence angle of the sun with collector surface vary throughout the year.

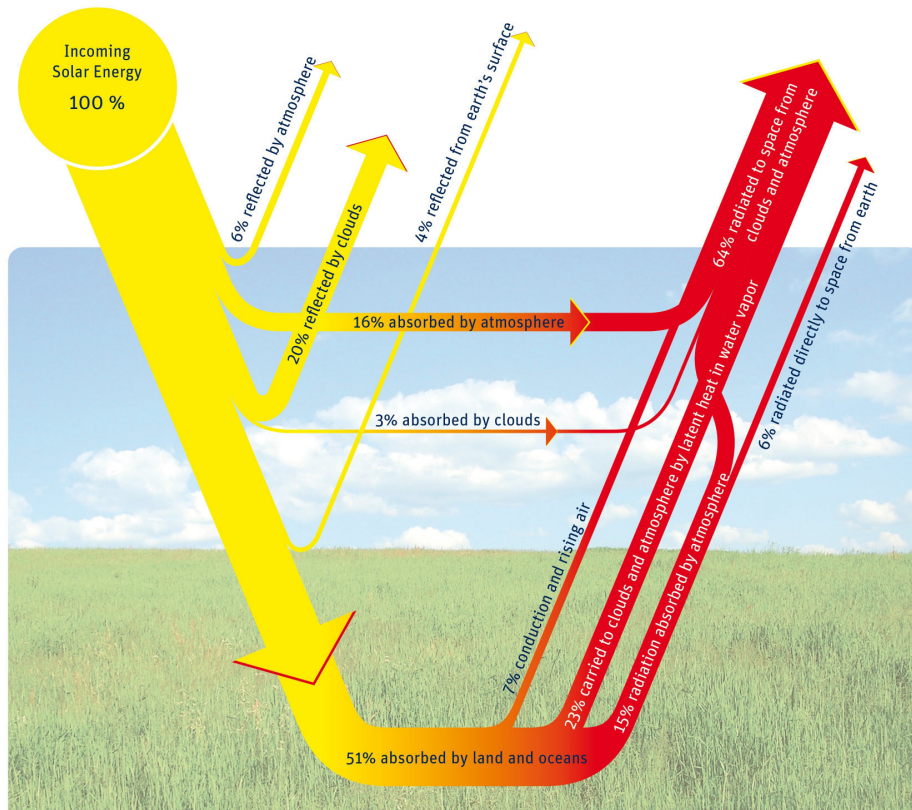


Figure 3.2. Attenuation of solar radiation through the atmosphere [70].

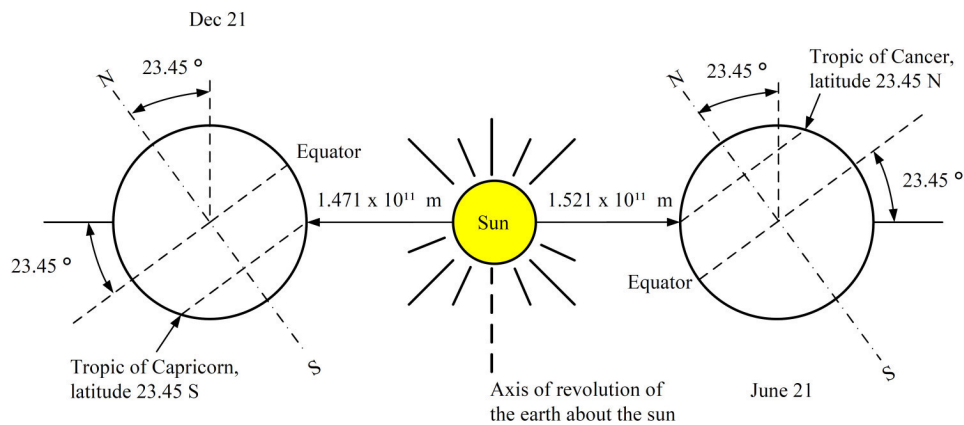
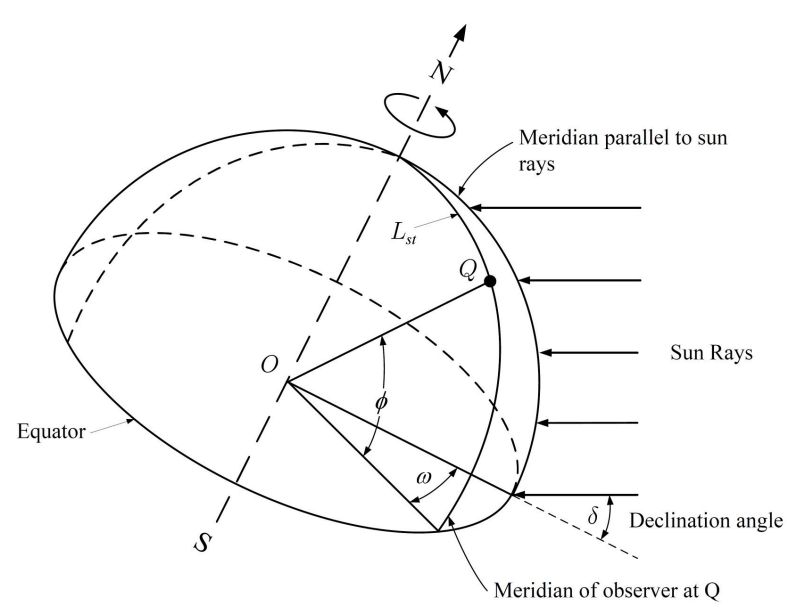
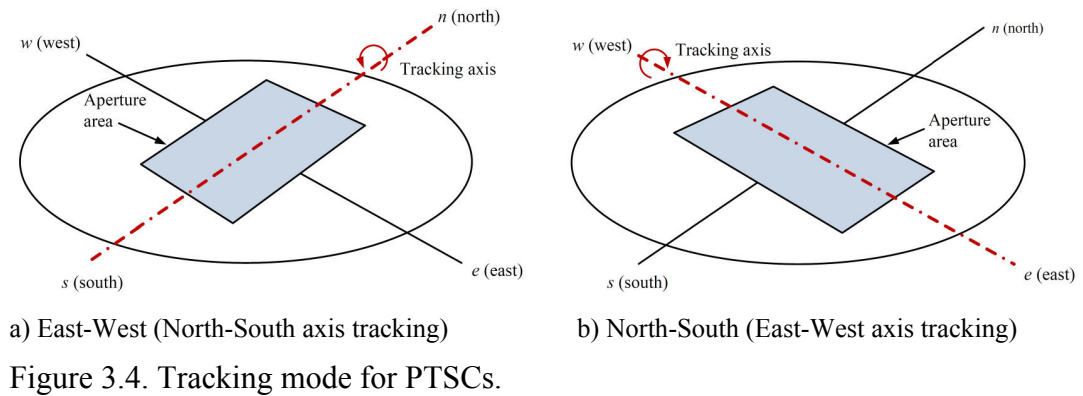


Figure 3.3. Motion of the earth about the sun. Adapted from [71].

The geometric relations between a plane moving relative to the earth and the sun are determined during solar calculations in order to find solar energy reaching the collector aperture. These calculations have been performed by considering the PTSC module installed at Gaziantep where the geographic position is $37^{\circ}02'N$ for the

latitude and $37^{\circ}19'E$ for the longitude. Generally, two different tracking modes are used in single-axis solar tracking (Figure 3.4): North–South (East–West axis tracking) and East–West (North–South axis tracking). The solar analyses have been made considering the orientation of the PTSC to be aligned on the North–South axis of the local. Since the North–South orientation provides the collector to gather more energy from the sun in summer season with respect to the other orientations over a period of one year [57,64].



Solar time is used in all of the sun-angle relationships but it does not coincide with local clock time. Thus it is necessary to convert standard time to solar time. The procedure for calculating the apparent solar time (AST) and the fundamental angles used in solar relations (Figure 3.5) from equation (3.1) to (3.6) are given by [72].

The general equation for calculating the apparent solar time is

$$AST = LST \pm 4 \times (L_{st} - L_{loc}) + E - DST \quad (3.1)$$

where L_{st} is the standard meridian for the local time zone, L_{loc} is the longitude of the location interested.

The first correction is for the difference in longitude between the observer's meridian (L_{loc}) and the meridian (L_{st}) on which the local standard time is based. Since the sun takes 4 min to transverse 1° of longitude. This correction is constant for a particular longitude, and the following rule must be followed with respect to sign convention. If the location is east of the standard meridian, the correction is added and if the location is west, it is subtracted from the local standard time. The second correction is from the equation of time, (E) which takes into account the perturbations in the earth's rate of rotation which affect the time the sun crosses the observer's meridian. If a daylight saving time is used, this must be subtracted from the local standard time. The term depends on whether daylight saving time is in operation (usually from end of March to end of October). The difference in minutes between solar time and standard time gives the result for all these corrections.

The values of the equation of time, E as a function of the day of the year can be obtained accurately from the following equation.

$$E = 229.2(0.000075 + 0.001868 \cos B - 0.032077 \sin B - 0.014615 \cos 2B - 0.04089 \sin 2B) \quad (3.2)$$

The declination angle, δ varies seasonally due to the tilt of the Earth on its axis of rotation at an angle of 23.45° with the ecliptic axis. This requires a coordinate transformation i.e., the sun moves around the earth. The declined function of the day of the year can be accurately defined as

$$\delta = 0.006918 - 0.399912 \cos B + 0.070257 \sin B - 0.006758 \cos 2B + 0.000907 \sin 2B - 0.002679 \cos 3B + 0.00148 \sin 3B \quad (3.3)$$

where $B = (n - 1) \frac{360}{365}$ and it is common variable for equations (3.2) and (3.3).

Hour angle, ω determines angular displacement of the sun east or west of the local meridian due to rotation of the earth on its axis at 15° per hour and takes negative values before solar noon and positive values after solar noon thus it is denoted by

$$\omega = \pm 15 \times (AST - 12 : 00) \quad (3.4)$$

Zenith angle, θ_z is defined as the angle between beam radiation and horizontal surface as illustrated in Figure 3.6. The zenith angle, for the PTSC module placing on a horizontal surface, equals to

$$\theta_z = \cos^{-1}(\cos \phi \cos \delta \cos \omega + \sin \phi \sin \delta) \quad (3.5)$$

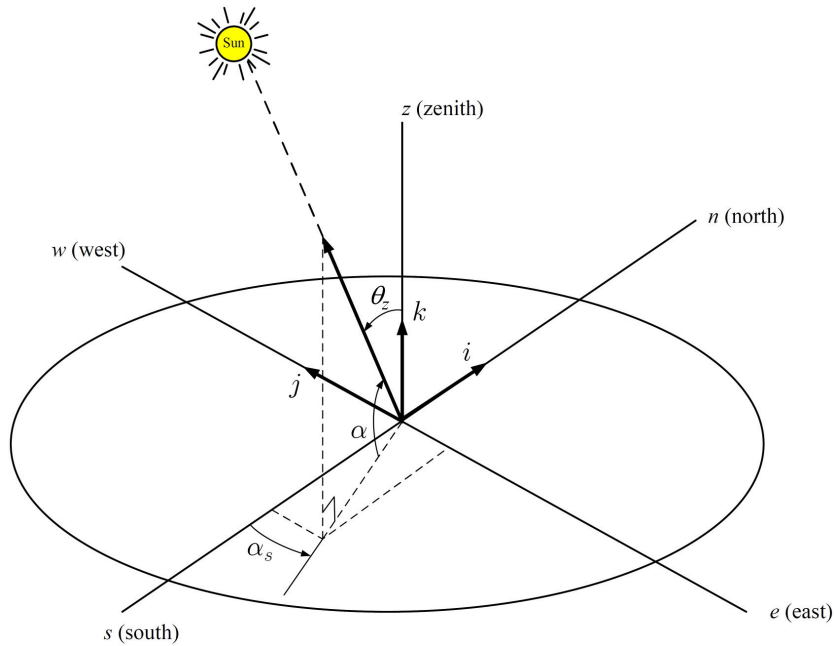


Figure 3.6. Solar zenith angle, θ_z , solar azimuth angle, α_s and solar altitude angle, α at the observer's coordinate system on the earth surface along with unit vectors i , j , k along their respective axes. Adapted from [71].

The amount of solar radiation falling on a moving surface depends strongly on the incidence angle. Solar tracking systems primarily function to orient the collector

aperture toward the sun. This minimizes the angle of incidence between the beam radiation and the collector aperture and increases the amount of energy gained by the receiver. The selection of the collector orientation with respect to the local directions is significant to reduce cosine losses during the tracking operation. The incidence angle for a plane rotated about a horizontal North–South axis with a single axis tracking is estimated by the relation,

$$\theta = \cos^{-1}\left(\sqrt{\cos^2 \theta_z + \cos^2 \delta \sin^2 \omega}\right) \quad (3.6)$$

3.2.3 Optical analysis

Optical analysis is required to estimate the optical efficiency which is defined as the ratio of the energy absorbed by the receiver to the energy incident on the collector's aperture. The optical efficiency is basically influenced by the optical properties of the material used, construction and operation of the collector. Furthermore, cosine losses occur during the tracking operation since the tracking path of the sun during a day may not always coincide with the tracking path of the collector. All these factors affect the optical efficiency of the collector, η_o so that it has been associated with the following terms,

$$\eta_o(\theta) = \rho\tau\alpha\gamma\kappa\epsilon' \cos\theta \quad (3.7)$$

The optical efficiency of the collector depends upon the radiative and optical properties of the receiving and the reflecting surfaces which are affected instantaneously by the variation of incidence angle since the position of the sun changes daily and seasonally. Thus the relations between the incidence angle and the radiative properties of the optical elements have been demonstrated herein for the estimation of the optical efficiency.

3.2.3.1 Reflectance of parabolic mirror

PTSCs require a reflecting surface shaped in a parabola to concentrate the beam radiation onto the receiver. Thus the reflector is produced from the material that

having high specular reflectance in order to direct much solar energy by minimizing the non-specular reflecting losses. Although there is not a direct correlation for estimating spectral, directional and temperature dependence of a reflecting material, certain methods were used to measure reflectivity for a number of metals [68,74].

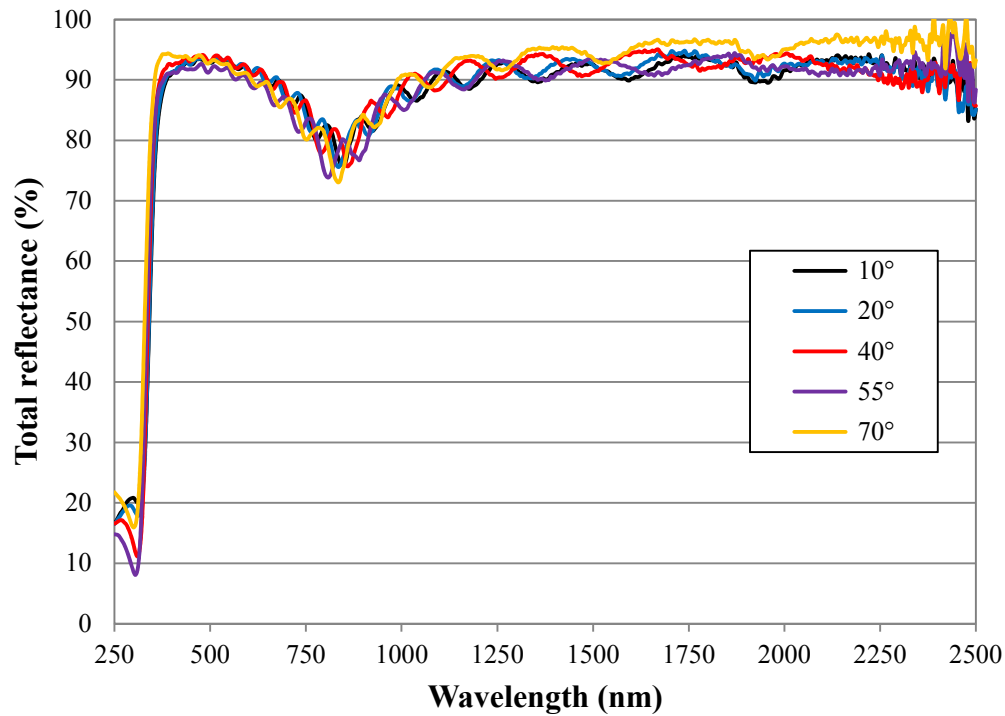


Figure 3.7. Total spectral reflectance of MIRO-SUN. Adapted from [75].

The reflecting material used in the optical analysis of the PTSC has been produced from multi-layer coated aluminum named as MIRO-SUN whose spectral, hemispherical reflectance character for the different angles of incidence shown in Figure 3.7 within the solar spectrum [75]. For the solar spectral reflectance, the spectral irradiance curve is essentially to be considered, and the spectral absorbance of aluminum around the wavelength of 800 nm needs to be taken into account. Not only anodized aluminum, but also multi-layer coated aluminum (constituting the MIRO-SUN) exhibits a tendency of decline in reflective property due to the energy absorption in this wavelength. Only the visible light spectrum plays a dominant role in spectral distribution of the extraterrestrial radiation thus the energy absorption of the aluminum is of no consequence since it lies outside the visible band (between 380 nm and 780 nm). As it is seen that the change in the directional spectral reflectance of the material displays nearly the same characteristic with its spectral

property at 10°, 20°, 40°, 55° and 70°. Acting from this figure, the evaluation of equation (3.8) was solved numerically by dividing the solar spectrum into a certain number of wavelengths such that the incremental solar energy in each of the wavelength intervals is constant ($dE = J_s(\lambda)d\lambda$).

$$\rho = \frac{\int_0^{\infty} \rho(\lambda)J_s(\lambda)d\lambda}{\int_0^{\infty} J_s(\lambda)d\lambda} \quad (3.8)$$

where $J_s(\lambda)$ is the solar spectral irradiance at wavelength λ .

When equation (3.8) is solved by utilizing the computational software program, Wolfram Mathematica 7.0 for the interval of 50 wavelength, the total directional spectral reflectance for the incidence angle of 10°, 20°, 40°, 55° and 70° are determined as 0.893, 0.895, 0.895, 0.899 and 0.880, respectively. Note that the spectral reflectance of the reflector varies with the angle of incidence which changes instantly due to the earth's orbital motion. The incidence angle gets different values while the collector is tracking the sun. Therefore, the estimation of the directional reflectance can be made by using the incidence angle corresponding to the local hour interested.

3.2.3.2 Cover transmittance

The cover material is made of DURAN glass whose transmissivity depending on wavelength and wall thickness is shown in Figure 3.8 [76]. As it is seen from the figure, the transmittance property of the cover is nearly constant within the solar radiation spectrum. However, the directional surface property of the cover varies with solar incidence angle. The relationship between the normal specular transmittance and its angular dependency is described as follows:

Since the receiver is covered by a single glass, the solar beam radiation is refracted from the ambient air with a refractive index, $n_1 = 1.0$, to the glass cover

with a refractive index, $n_2 = 1.473$ when θ_2 is not equal to θ . The angles θ_1 and θ_2 , (see Figure 3.9) are related with the indices of refraction by Snell's law,

$$\frac{n_1}{n_2} = \frac{\sin \theta_1}{\sin \theta_2} \quad (3.9)$$

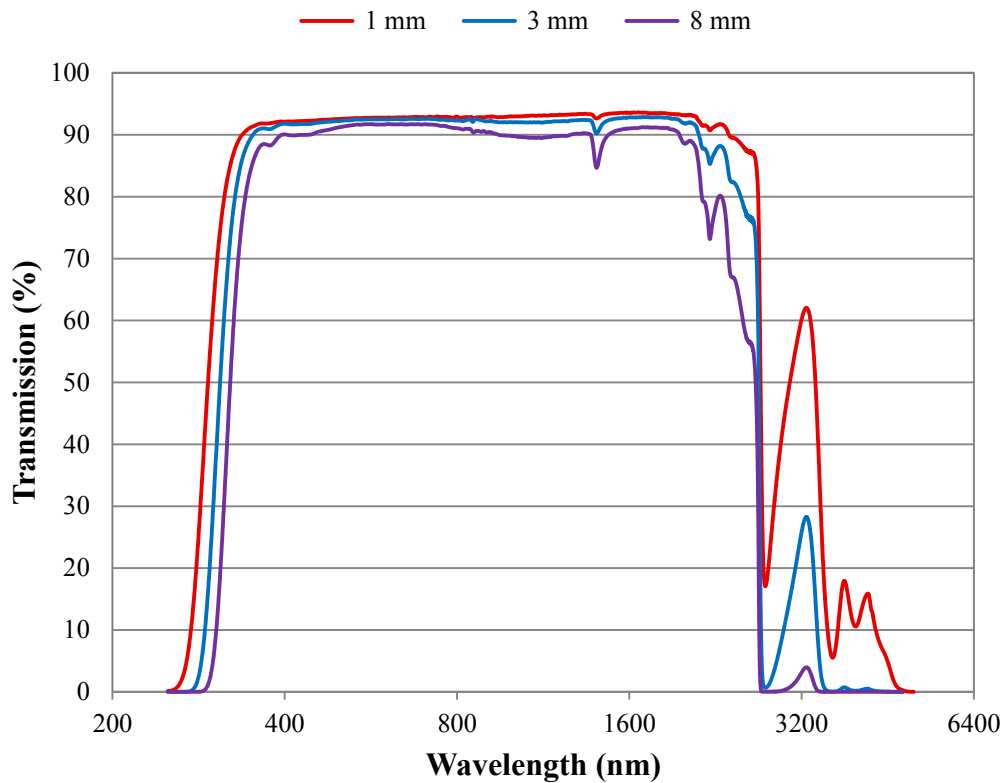


Figure 3.8. Transmission in DURAN glass. Adapted from [76].

It is convenient to choose a coordinate system in which the z-axis is placed along the tracking axis and the y-axis along the axis of symmetry or optical axis, as shown in Figure 3.9. With perfect tracking, the misalignment between the beam radiation and the glass cover vanishes and θ_2 equals the incidence angle. The parallel and perpendicular components of unpolarized radiation are functions of the projections of the incidence angle of the sun on the y-z plane and on the x-y plane, respectively. For smooth surfaces, the components can be determined using Fresnel's derivation,

$$r_{\perp} = \frac{\sin^2(\theta_2 - \theta_1)}{\sin^2(\theta_2 + \theta_1)} \quad (3.10)$$

$$r_{\parallel} = \frac{\tan^2(\theta_2 - \theta_1)}{\tan^2(\theta_2 + \theta_1)} \quad (3.11)$$

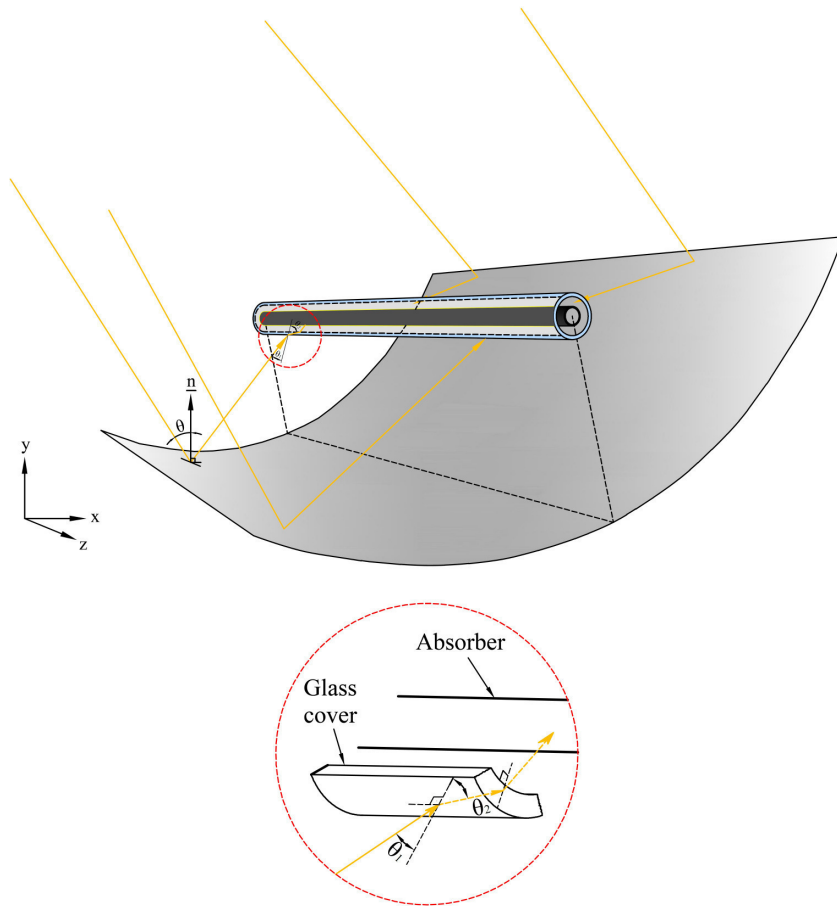


Figure 3.9. Refraction of beam radiation over the receiver tube.

The cover can be treated as partially transparent hence some portion of the incidence radiation is absorbed by the cover itself. The absorption of the transmitted solar radiation within the cover is determined by

$$\tau_a = e^{\left(\frac{-KL}{\cos \theta_2}\right)} \quad (3.12)$$

where K is called the extinction coefficient that is 4 m^{-1} for “water white” glass. For a single cover, the transmittance can be defined by averaging the transmittance of the parallel and perpendicular components of polarization when both reflection and absorption losses considered. As a result, the angular transmittance of the cover element is specified with equation (3.13).

$$\tau = \frac{1}{2} \left[\left(\frac{1-r_{\parallel}}{1+r_{\parallel}} \right) \left(\frac{1-r_{\parallel}^2}{1-(r_{\parallel}\tau_a)^2} \right) + \left(\frac{1-r_{\perp}}{1+r_{\parallel}} \right) \left(\frac{1-r_{\perp}^2}{1-(r_{\parallel}\tau_a)^2} \right) \right] \quad (3.13)$$

3.2.3.3 Absorptivity of absorber

The absorber pipe is coated with selective whose solar absorptance depends also upon the incidence angle. Knowledge of the directional dependent solar absorptance of the solar absorbers is important but such data are not available for most of the commercial absorbers. Nevertheless there is not sufficient study in the literature for describing the relationship between the directional and normal absorptance, it can be estimated by the relation that provides fair results for the angle of incidence up to 80° [51].

$$\frac{\alpha}{\alpha_n} = 1 + 2.0345 \times 10^{-3} \theta - 1.99 \times 10^{-4} \theta^2 + 5.324 \times 10^{-6} \theta^3 - 4.799 \times 10^{-8} \theta^4 \quad (3.14)$$

3.2.3.4 Intercept factor of PTSC

The intercept factor is an optical property which is defined as the ratio of the solar radiation intercepted by the receiver to the radiation reflected by the parabolic mirror that strikes directly to the receiver. It is affected by random and non-random errors [77]. Random errors are truly random in nature owing to the fact that they can be represented by normal probability distributions with zero mean. They originate from, in turn

- The misalignment of the ideal focus of the reflector depending on the energy distribution of the sun shape due to purely random tracking errors, σ_{sun} .
- The slope errors of the reflector surface, i.e., surface imperfections, taken place during manufacture, assembly and/or operation, σ_{slope} .
- The scattering effects due to the property of the optical material used, σ_{mirror} .

Random errors can be modeled as statistically by determining the standard deviation of the total reflected energy distribution at normal incidence [78] as equation (3.15).

$$\sigma = \sqrt{\sigma_{sun}^2 + 4\sigma_{slope}^2 + \sigma_{mirror}^2} \quad (3.15)$$

Non-random errors generally describe the errors arise from the permanent characteristics of the collector due to its manufacture/assembly and/or operation. In general these errors cause the central ray of the reflected energy distribution (effective sunshape) to deviate from the design focal line. The intercept factor is defined by random and non-random errors and universal error parameters as well. Using all these error parameters, the intercept factor is determined by [78].

$$\gamma = \frac{1 + \cos \varphi_r}{2 \sin \varphi_r} \int_0^{\varphi_r} \left[\left[\text{Erf} \left[\frac{\sin \varphi_r (1 + \cos \varphi) (1 - 2d^* \sin \varphi) - \pi \beta^* (1 + \cos \varphi_r)}{\sqrt{2} \pi \sigma^* (1 + \cos \varphi_r)} \right] \right] \right. \\ \left. - \text{Erf} \left[- \frac{\sin \varphi_r (1 + \cos \varphi) (1 + 2d^* \sin \varphi) + \pi \beta^* (1 + \cos \varphi_r)}{\sqrt{2} \pi \sigma^* (1 + \cos \varphi_r)} \right] \right] \frac{d\varphi}{(1 + \cos \varphi)} \quad (3.16)$$

where

C : area concentration ratio, $C = (w_a - D_{oa}) / \pi D_{oa}$.

d^* : universal nonrandom error parameter due to receiver mislocation and reflector profile errors, $d^* = d_r / D_{oa}$.

β^* : universal nonrandom error parameter due to slope error, $\beta^* = \beta C$.

σ^* : universal random error parameter, $\sigma^* = \sigma C$.

For the evaluation of the intercept factor, a computer program was written in Wolfram Mathematica 7.0 to solve equation (3.16) numerically using Trapezoidal rule. The solutions obtained for different random and nonrandom collector parameters gave consistently satisfactory results compared to [78]. Based on the computer program, the intercept factor has been estimated to be considering the collector as carefully-fabricated. The error parameters are given in Table 3.2.

Table 3.2. Parameters for equation (3.16). Adapted from [79].

Parameter	Value
Sun deviation, σ_{sun} ^a	0.0025 rad
Slope deviation, σ_{slope}	0.0040 rad
Mirror deviation, σ_{mirror}	0.0020 rad
Misalignment slope error, β	0.0035 rad
Dislocation from ideal focus, d_r	0.002 m
Rim angle, φ_r [67]	77°

^a Standard deviation of the energy distribution of the sun's rays at solar noon on a clear day

3.2.3.5 Geometric factor

Geometric factor can be associated with the effective reduction in the aperture area due to incidence effects such as blockage, shading and end-effect. Blockage is not mentioned for a single collector because it usually occurs in parallel arrangement of collector arrays. Thus, in this analysis, the geometric factor is only affected by shading and end effect. Shading is caused by the receiver that forms a strip of shadow (projected area of the absorber) on the reflector. Hence the shaded part of the reflector area is not effectively utilized since it is not subjected to the solar heat flux. The area loss is related as a measure of the factor,

$$\zeta = \frac{D_{oa}}{l_a} \tan \theta \quad (3.17)$$

End-effect can be defined as the reflected beam radiation from the end of the collector cannot be received by the receiver tube. If the receiver tube has the same length as the reflector and is placed symmetrically then end-effect is given by [80].

$$\Gamma = \frac{f}{l_a} \left(1 + \frac{w_a^2}{48f^2} \right) \tan \theta \quad (3.18)$$

Thus a portion of the aperture area has inactively used due to all these effects. The geometric factor is expressed by equation (3.19) combining equations (3.17) and (3.18) as

$$\kappa = 1 - \left[\frac{D_{oa}}{l_a} + \frac{f}{l_a} \left(1 + \frac{w_a^2}{48f^2} \right) \right] \tan \theta \quad (3.19)$$

3.2.3.6 Miscellaneous factor

Effects of miscellaneous parameters on optical efficiency can be defined as surface condition of reflecting and receiving components and unaccounted factors during the system operation. Unaccounted factors can be disregarded when it is considered carefully-fabricated and well-arranged collector nevertheless it may occur in reality. The other factors affect the miscellaneous can be counted as [50]

- Shadowing sourced from bellows, shielding, supports, ε'_1
- Dust and contamination on reflector, $\varepsilon'_2 = \rho_i / \rho$ (ρ_i is an input parameter with usual range: 0.88–0.93)
- Dust and contamination on receiver, $\varepsilon'_3 = (1 + \varepsilon'_2) / 2$

The values for ε' are given in Table 3.3. The miscellaneous factor can be defined as

$$\varepsilon' = \prod_{i=1}^N \varepsilon'_i \quad (3.20)$$

Table 3.3. Miscellaneous factors. Adapted from [50].

Factor	Value
Shadowing, ε'_1	0.980
Clean mirror reflectivity, ρ	0.893
Dirt on mirror, ε'_2	0.989
Dirt on receiver, ε'_3	0.995

3.3 Thermal analysis of receiver

Thermal analysis of a solar collector is significant to determine the thermal efficiency and the useful heat gain. A detailed thermal analysis has been proposed herein in order to make a consistent model that gives more likely results to predict

the actual behavior of the PTSC under distinct working conditions. Thus the model study was developed to satisfy the following states that hold the physical nature of the system. The main characteristics of the model include:

- The PTSC performs under steady state conditions in other words; there is no change in the thermodynamic state properties with respect to time since the surface temperatures are regarded as constant at an arithmetic mean of inlet and exit side of the receiver.
- Heat transfer is one-dimensional since any significant temperature gradients exist predominantly in radial direction. Solar radiation comes to the receiver from the radial direction, and the cross-section of the receiver is relatively shorter than the length of the receiver. Hence the temperature change in the axial direction can be treated as negligible. Owing to the fact that the temperature of the HTF increases linearly in the flow direction in the case of constant surface heat flux, thus the temperature change will be negligible along the receiver on an average temperature i.e., bulk temperature. However, once the operating field reaches hundreds or thousands of meters using collector arrays, the change in flow rate (caused by the density change) and pressure drop can have an appreciable effect on the heat transfer. In this case, the temperature variation along the receiver will deviate somewhat from the linearity, thus two-dimensional model can reflect the nonlinearity due to the change in longitudinal axis.

3.3.1 Heat loss analysis

The thermal analysis provides to estimate the heat losses from the receiver, and the useful heat gain transferred to the working fluid as a consequence. The solar irradiation falling onto the collector's aperture is reflected partially by the mirrors toward the receiver. The directed irradiation is refracted by the cover and focused onto the absorber. As a result, the surface temperature of the absorber is increased and heat is conducted cross the wall of the absorber. The fluid passing through the absorber pipe transfers thermal energy by forced convection as useful heat and the remaining is lost back to the annulus as a combination of radiation and natural convection, and lost through the retainers by conduction as well. Then the lost energy

is eventually conducted through the cover and transferred from the outer surface of the cover by convection to the ambient air and radiation to the reflector and the sky.

The thermal condition on the receiver surface was approximated as being subjected to constant heat flux along the PTSC. The mean fluid temperature of the HTF, T_m increases linearly in the flow direction in the case of constant surface heat flux, since the surface area increases linearly in the flow direction. In the fully developed region, the inner surface temperature of the absorber will also increase linearly in the flow direction since h_{HTF} is treated as constant along the absorber.

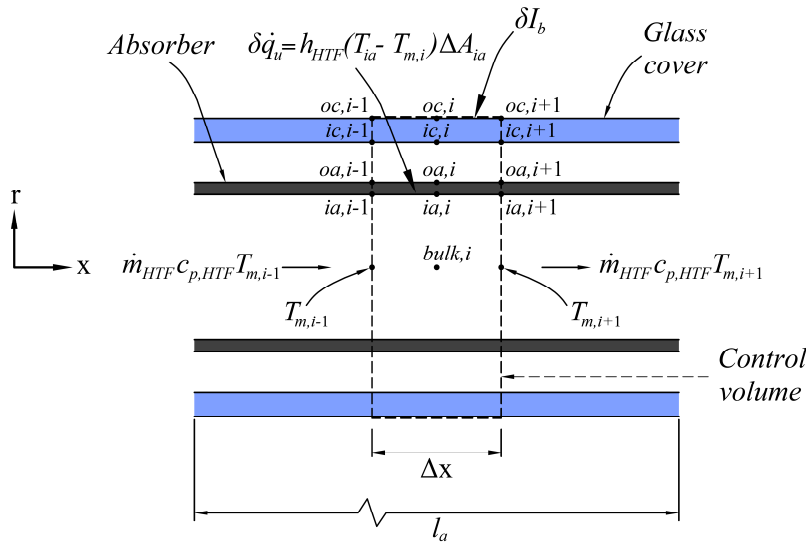


Figure 3.10. Heat transfer analysis for a differential control volume in the receiver.

If the energy balance is applied to the control volume shown in Figure 3.10, the generalized form of the governing equation (3.21) for steady-state can be defined by means of discretizing the receiver by dividing into N number of equal finite segments. The radial heat fluxes are assumed uniform and normal to the surfaces for each segment, and the central temperature is evaluated at the average temperature between the left and right side of the segment, $T_{m,i} = (T_{m,i-1} + T_{m,i+1})/2$. The longitudinal temperature is treated to be linear and the convection coefficient to be constant as mentioned above. Therefore, the right and left side longitudinal convection terms cancel out, and only the HTF will transfer energy in the longitudinal direction.

$$\sum_{i=1}^N \delta \dot{q}_{u,i} p_{ia} \Delta x = \dot{m}_{HTF} \left[\left(h + \frac{u_m^2}{2} \right)_{i+1} - \left(h + \frac{u_m^2}{2} \right)_{i-1} \right] \quad i = 1, 2, 3, \dots, N \quad (3.21)$$

where $h \cong c_p T$ for incompressible fluids. $\delta \dot{q}_u$ is the differential useful energy gained by the inner surface of the absorber ($\Delta A_{ia} = p_{ia} \Delta x$), and p_{ia} is the internal perimeter of the absorber pipe.

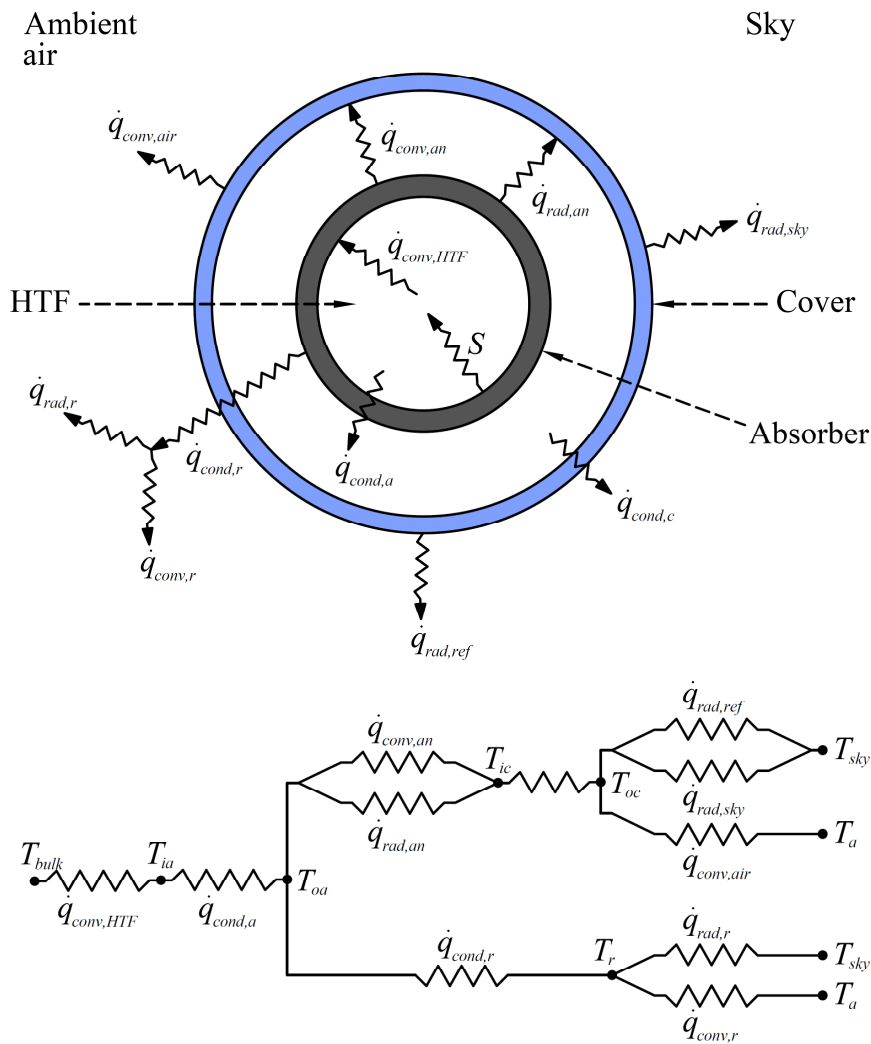


Figure 3.11. Resistance network applied for the cross-section of the receiver tube.

The thermal analysis was established by the *thermal resistance method* shown in Figure 3.11 to find the nodal temperatures. The net heat loss from the receiver tube is caused by the temperature difference arising in radial direction. In order to determine the temperatures on the receiver, the governing energy equations were written

between the nodal points of the resistance network. The model algorithm makes possible to solve the non-linear equations in order to calculate the temperatures and the heat transfer coefficients for the receiver. These energy balance relations are expressed with three sets of equality for each segment as shown in equations (3.22), (3.23) and (3.24).

$$\dot{q}_{conv,HTF} = \dot{q}_{cond,a} \quad (3.22)$$

$$\dot{q}_{cond,a} = \dot{q}_{conv,an} + \dot{q}_{rad,an} + \dot{q}_{cond,r} \quad (3.23)$$

$$\dot{q}_{cond,c} = \dot{q}_{conv,air} + \dot{q}_{rad,r-s} + \dot{q}_{conv,r} + \dot{q}_{rad,r} \quad (3.24)$$

3.3.1.1 Heat transfer to HTF

The flow inside the absorber pipe is stated by forced convection due to pumping of the HTF. The flow regime is defined according to the Reynolds number (Re) which specifies whether the regime is laminar or turbulent. The flow in a pipe is laminar when the generally accepted value of the critical Re is below 2300 [81]. The mass flowrate of the HTF is denoted by equation (3.25) under steady-state conditions. The typical thermal properties of the HTF (Renolin therm 320) [82] used in the analysis are given in Appendix A.

$$\dot{m}_{HTF} = \rho_{HTF} A_a u_{m,HTF} \quad (3.25)$$

Heat flux focused onto the outer surface of the receiver can be treated as constant since the solar heat flux is distributed uniformly along the absorber surface. Therefore, for fully developed laminar flow in a pipe subjected to constant surface heat flux, the Nusselt number (Nu) is a constant [81].

$$Nu_{HTF} = 4.364 \quad (3.26)$$

When the Re is higher than 10,000, the flow is usually fully turbulent in smooth pipes [81]. In this case, the Nu relation is defined by equation (3.27) which can be used accurately for fully developed turbulent flow [83].

$$\text{Nu}_{HTF} = \frac{\sqrt{f/8} \text{Re}_{HTF} \text{Pr}_{HTF}}{12.48 \text{Pr}_{HTF}^{2/3} - 7.853 \text{Pr}_{HTF}^{1/3} + 3.613 \ln(\text{Pr}_{HTF}) + 5.8 + C} \quad \begin{array}{l} 0.5 \leq \text{Pr} \leq 2000 \\ 10^4 \leq \text{Re} \leq 5 \times 10^6 \end{array} \quad (3.27)$$

where $C = 2.78 \ln(\sqrt{f/8} \text{Re}_{HTF} / 90)$ and f is the friction factor, $f = (0.79 \ln \text{Re}_{HTF} - 1.64)^{-2}$ for smooth pipes [81].

The convection heat transfer coefficient within the absorber is obtained from

$$h_{HTF} = \text{Nu}_{HTF} \frac{k_{HTF}}{D_{ia}} \quad (3.28)$$

Then, the convection heat transfer within the absorber pipe is defined using the Newton's law of cooling,

$$\dot{q}_{conv,HTF} = h_{HTF} p_{ia} (T_{ia} - T_{bulk}) \quad (3.29)$$

$T_{bulk} = T_{m,i}$ is the bulk mean fluid temperature, which is the arithmetic average of the mean fluid temperatures at the inlet and the exit of the each segment. For internal flow, the mean temperature of the fluid increases linearly in flow direction in the case of constant surface heat flux thus the fluid properties are basically evaluated at the bulk mean fluid temperature through the pipe.

3.3.1.2 Heat conduction through absorber

Heat transfer cross the wall thickness of a hollow cylinder is realized by pure conduction. The conduction heat transfer rate through the radial direction of the absorber pipe is obtained by applying the Fourier's law heat conduction.

$$\dot{q}_{cond,a} = \frac{2\pi k_a}{\ln(D_{oa}/D_{ia})} (T_{oa} - T_{ia}) \quad (3.30)$$

Thermal conductivity of the absorber has been treated as a varying property which is affected by material type and temperature. The absorber is made of 304L type stainless steel and its temperature dependence can be evaluated using the linear relationship below [84].

$$k_a = 0.013T_{ave,a} + 15.2 \quad (3.31)$$

where $T_{ave,a} = (T_{oa} + T_{ia})/2$.

3.3.1.3 Heat transfer in annulus region

Heat transfer mechanism between the absorber and the cover involves simultaneous convection and radiation. Mode of the convection heat transfer depends on annulus pressure; it occurs by thermal conduction when the annulus pressure is below 1 Torr and can be treated as natural convection for the pressure above it. The thermal conduction through gases can be distinguished by the continuum, temperature-jump, transition and free molecular regimes [85]. These regimes are determined by the value of the Knudsen number (Kn) which is defined as the ratio of the mean free path of the gas molecules to the characteristic dimension of the body or surface. In the continuum regime ($Kn < 0.01$), where the molecular mean free path is several orders of magnitude smaller than the characteristic dimension, thermal conduction through a gas is the result of numerous collisions between gaseous molecules. In the temperature-jump regime ($0.01 < Kn < 0.1$), the molecular mean free path is much smaller than the characteristic dimension. In the transition regime ($0.01 < Kn < 10$), the molecular mean free path of the gas is of the same order as the characteristic dimension. This regime is in between temperature-jump and free molecular regimes. In the free molecular regime ($Kn > 10$), where the molecular mean free path is large compared to the characteristic dimension, inter-molecular collisions between gas molecules are infrequent when compared with molecular collisions with solid surfaces.

3.3.1.3.1 Free molecular convection

When the annulus region is evacuated, the pressure in the annulus is reduced. In this case, no convection currents occur in the annulus thus heat transfer is suppressed by conduction. As the corresponding pressure falls under 0.0001 Torr, heat transfer can be defined by free molecular convection. The recommended correlation for this case can be related by [86].

$$\frac{k_{eff}}{k_{std}} = \left[1 + \frac{(2-a)(9\gamma-5)\lambda}{a(\gamma+1)\ln(D_{ic}/D_{oa})} \left(\frac{1}{D_{ic}} + \frac{1}{D_{oa}} \right) \right]^{-1} \quad (3.32)$$

where λ is the mean free path of the gas molecules, and a is the thermal accommodation coefficient.

$$\lambda = 2.331 \times 10^{-20} \frac{T_{ac}}{P_a \delta^2} \quad (3.33)$$

Equation (3.32) is valid for $Ra_{an} < [D_{ic}/(D_{ic} - D_{oa})]^4$ but slightly overestimates under very low pressures (0.0001 Torr). The molecular diameter of the annulus gas, δ is equal to 3.55×10^{-10} m for air. P_a is the pressure of the annulus region in Pascals and T_{ac} is the average temperature $(T_{oa} + T_{ic})/2$ in Kelvin. The ratio of specific heats, γ for air can be evaluated at T_{ac} . The thermal accommodation coefficient, a is an empirical attempt to quantify the complicated interaction between an impinging gas molecule and molecules comprising a solid boundary. When a gas comes in contact with a solid, there is a flow of energy from the one to the other and the rate of interchange is defined in terms of the thermal accommodation coefficient. Accommodation coefficients range between 0 and 1. In particular, the thermal accommodation coefficient not only depends on the structure of the gas molecule itself, but also the physical and mechanical condition of the surface. The available data for a number of monatomic and polyatomic gases on different metal surfaces at temperatures in the range 273–1250 K was investigated by [87] who developed the correlation as

$$a = F \left(\frac{M_g^*}{C_1 + M_g^*} \right) + (1 - F) \left[\frac{2.4\mu}{(1 + \mu)^2} \right] \quad (3.34)$$

In equation (3.34), F stands for the fractional coverage of the adsorption layer which depends upon the nature of the surface and μ is the ratio of molecular weight of the gas to that of the solid.

$$F = \exp \left[C_0 \left(\frac{T_s - T_0}{T_0} \right) \right] \quad (3.35)$$

$$\mu = \frac{M_g}{M_s} \quad (3.36)$$

where $C_0 = -0.57$, $C_1 = 6.8$, and $T_0 = 273$ K. $M_g^* = 1.4M_g$ for polyatomic gases.

The rate of heat transfer through the annular space is finally expressed by

$$\dot{q}_{conv,an} = \frac{2\pi k_{eff}}{\ln(D_{ic}/D_{oa})} (T_{oa} - T_{ic}) \quad (3.37)$$

3.3.1.3.2 Natural convection

When the pressure of the annulus region is over 1 Torr, the natural convection currents begin stronger. In this case, the calculation of the convective heat transfer is defined by the conduction layer model. There are many available analytical models and correlations for natural convection in a horizontal circular annulus with isothermal boundary conditions obtained from experimental data, numerical results in the literature.

A method for estimating the convection heat transfer by conduction covering the regimes of laminar and turbulent flows were only correlated by [88] for horizontal cylinders to a cylindrical enclosure as below. Correlations are expressed in terms of

the Nusselt and Rayleigh numbers which are based on the characteristic length of D_{ia} .

$$\text{Nu}_{an} = \left[\text{Nu}_{cond}^{15} + \text{Nu}_{conv}^{15} \right]^{1/15} \quad (3.38)$$

where Nu_{cond} and Nu_{conv} refer to expressions for the conductive and convective limits, respectively. The conductive limit in equation (3.38) is found by for those cases involving concentric cylinders:

$$\text{Nu}_{cond} = \frac{2}{\ln(D_{ic}/D_{ia})} \quad (3.39)$$

The convection term in equation (3.39) is determined by the following expression:

$$\text{Nu}_{conv} = \frac{2}{\ln\left(\frac{1 + 2/\text{Nu}_i}{1 - 2/\text{Nu}_o}\right)} \quad (3.40)$$

For the case of an air-filled annulus, the convection on the inner and outer surfaces, Nu_i and Nu_o , for the full range of Ra_{an} including both laminar and turbulent flow, are calculated by:

$$\text{Nu}_i = 0.3987\text{Ra}_{an}^{1/4} \quad (3.41)$$

$$\text{Nu}_o = \left(39.24 + \left(\frac{D_{ic}}{D_{ia}} \right)^{5/4} \text{Ra}_{an}^{5/12} \right)^{3/5} \quad (3.42)$$

The typical thermal properties of air are given in Appendix B [89].

The convection heat transfer coefficient within the annulus region is obtained from

$$h_{an} = \text{Nu}_{an} \frac{k_{an}}{L_{an}} \quad (3.43)$$

And the convection heat transfer rate through the annulus is expressed by

$$\dot{q}_{conv,an} = h_{an} p_{oa} (T_{oa} - T_{ic}) \quad (3.44)$$

3.3.1.3.3 Thermal radiation

Radiation heat transfer inside an annulus occurs due to temperature difference between the absorber and the cover even if the annulus space comprises a gas. Free-molecular or natural convection heat transfer coefficients are typically very low compared to those for forced convection. Therefore, radiation is usually disregarded in forced convection, but it must be considered in free convection condition that involves a gas. This is especially the case for surfaces with high emissivity.

Considering the enclosure consisting of two opaque surfaces at equilibrium temperatures, the radiation heat transfer can be calculated by equation (3.45) which is applicable to gray (independent of wavelength), diffuse (independent of direction) and opaque surfaces. These approximations are reasonable since the absorber surface behaves nearly gray in the solar spectrum and behaves diffuse emitter when its emissivity remains nearly constant for the angles lower than 40° [68]. The calculations illustrate that the angle of incidence gets the angular values lower than $\theta < 40^\circ$ with solar tracking especially in summer season. The cover material behaves like an opaque material at longer-wavelength infrared regions of the electromagnetic spectrum when it is losing energy by radiation. Once these approaches are considered, the radiation heat transfer within the annulus can be estimated by

$$\dot{q}_{rad,a} = \frac{\sigma(T_{oa}^4 - T_{ic}^4)}{\frac{1 - \varepsilon_a}{\varepsilon_a} + \frac{1}{F_{ac}} + \frac{1 - \varepsilon_c}{\varepsilon_c} \left(\frac{D_{oa}}{D_{ic}} \right)} \quad (3.45)$$

where σ is Stefan-Boltzmann constant and equals to $5.67 \times 10^{-8} \text{ W/m}^2\text{K}^4$ [81].

3.3.1.4 Heat transfer from retainers

Retainers are used as connecting elements to join the absorber and the cover. Contrarily, the support brackets are the gripping elements connected to retainers to keep the receiver tube in position at the focal line of the reflector as shown in Figure 3.12. When the absorber pipe is heated up, it conducts heat to the retainer which loses the heat by convection and radiation. Treating the support brackets as an extended surface or a fin element, the rate of heat transfers from the retainer for the convection and the radiation are related by equation (3.47) and (3.48), respectively [81].

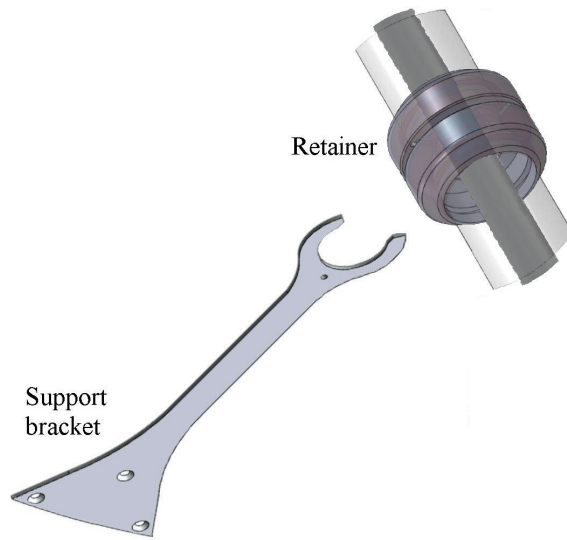


Figure 3.12. Support bracket and retainer. Adapted from [67].

$$\dot{q}_{cond,r} = \dot{q}_{conv,r} + \dot{q}_{rad,r} \quad (3.46)$$

$$\dot{q}_{conv,r} = \sqrt{h_{air} p_r k_r A_r} (T_b - T_a) \tanh mL/L \quad (3.47)$$

$$\dot{q}_{rad,r} = \sigma \varepsilon_r p_r (T_r^4 - T_{sky}^4) \quad (3.48)$$

Noting that $m = \sqrt{h_{air} p_r / k_r A_r}$. Also L , A_r and p_r represent the length, the cross-section and the perimeter of the fin, respectively.

3.3.1.5 Heat conduction through cover

Solar energy absorption within the cover material was not included in the thermal analysis since the radiation incident on the absorber is partly reflected back to the cover and the left, in turn, is absorbed by the absorber pipe. The cover is a glass medium and its solar absorptivity is comparatively small $\alpha \approx 0.02$ [68], thus being considered in the optical analysis of the cover. Only the heat transfer cross the cover material, which is opaque, is considered here and can be defined by Fourier's law of heat conduction.

$$\dot{q}_{cond,c} = \frac{2\pi k_c}{\ln(D_{oc}/D_{ic})} (T_{ic} - T_{oc}) \quad (3.49)$$

The thermal conductivity of the cover material at 90°C can be taken as 1.2 W/m·°C [76].

3.3.1.6 Heat transfer from receiver to surroundings

Heat loss from the outer surface of the cover involves the combined convection and the radiation heat transfer modes. Convection heat transfer has two regimes; natural and forced convection. In order to provide more realistic approach, the mixed convection regime (natural and forced) was considered in the analysis. Furthermore, the radiation heat transfer from the cover was handled not only with the sky but also with the reflector.

3.3.1.6.1 Convection to ambient air

Convection heat transfer on the external surface of the receiver can change depending on windy conditions of ambient air. Estimation of the convection heat transfer requires the average heat transfer coefficient over the entire surface although variation of the local heat transfer coefficient along the circumference of the cover is not uniformly distributed. For a heated horizontal cylinder subjected to cross flow, the angle of the approaching stream greatly affects the heat flow in the mixed convection regime. The effect of receiver orientation on the average Nu is negligible

when the Re is $\leq 4.5 \times 10^5$ [90]. However this is the case when wind speed is higher than 13 m/s at the standard atmospheric condition.

For a long isothermal horizontal circular cylinder in an isothermal environment, Nu can be obtained by adapting the correlations to air for the following equations.

$$Nu^T = 0.772 Ra_{air}^{1/4} \quad (3.50)$$

$$Nu_l = \frac{2f}{\ln(1 + 2f/Nu^T)} \Rightarrow f = 1 - \frac{0.13}{(Nu^T)^{0.16}} \quad (3.51)$$

$$Nu_t = 0.103 Ra_{air}^{1/3} \quad (3.52)$$

$$Nu_N = [(Nu_l)^{10} + (Nu_t)^{10}]^{1/10} \quad (3.53)$$

$$Nu_F = a Re^n \quad (3.54)$$

Table 3.4. Constants for equation (3.55). Adapted from [91].

	Re range						
	10 ⁻⁴ to 4×10 ⁻³	4×10 ⁻³ to 9×10 ⁻²	9×10 ⁻² to 1.0	1.0 to 35	35 to 5×10 ³	5×10 ³ to 5×10 ⁴	5×10 ⁴ to 2×10 ⁵
a	0.437	0.565	0.800	0.795	0.583	0.148	0.0208
n	0.0895	0.136	0.280	0.384	0.471	0.633	0.814

A procedure for calculating the heat transfer in the mixed convection regime has been proposed by [91]. For a given Ra and Re , the value of Nu is computed from equation (3.54) for air. For the given Re , the constants a and n are chosen from Table 3.4. The value of Re_i is then found from equation (3.55) using the equality of

$$Nu_F = Nu_N.$$

$$Re_i = [Nu_N/a]^{1/n} \quad (3.55)$$

An effective Reynolds number, Re_{eff} is then calculated from

$$Re_{eff} = \left[(Re_i + Re_{air} \cos \phi)^2 + (Re_{air} \sin \phi)^2 \right]^{1/2} \quad (3.56)$$

and the substitution of Re_{eff} into equation (3.56) obtains the Nu relation for mixed convection regime.

$$Nu_{air} = a Re_{eff}^n \quad (3.57)$$

The convection heat transfer coefficient outside of the receiver tube is obtained from

$$h_{air} = Nu_{air} \frac{k_{air}}{D_{oc}} \quad (3.58)$$

and consequently, the convection heat transfer on the outside of the cover can be denoted by

$$\dot{q}_{conv,air} = h_{air} p_{oc} (T_{oc} - T_a) \quad (3.59)$$

3.3.1.6.2 Radiation from receiver to reflector and sky

Heat transfer occurs over the outer surface of the cover also by radiation to the surrounding mediums i.e., the reflector and the sky. The cover was treated that a portion is surrounded by the sky, and the rest is faced to the parabola of the reflector as shown in Figure 3.13. Analysis of radiation transfer in enclosures involving nonblack surfaces is very complicated unless some simplifying assumptions are made such that surfaces showing the properties as opaque, diffuse and gray and also each surface of the enclosure is isothermal. All these considerations are appropriate and reasonable for the nature of the analysis to be made herein. The radiation heat transfer among the cover, the reflector and the sky was examined using the *Network*

method. The systematic approach for solving this type of radiation problems was introduced by [92].

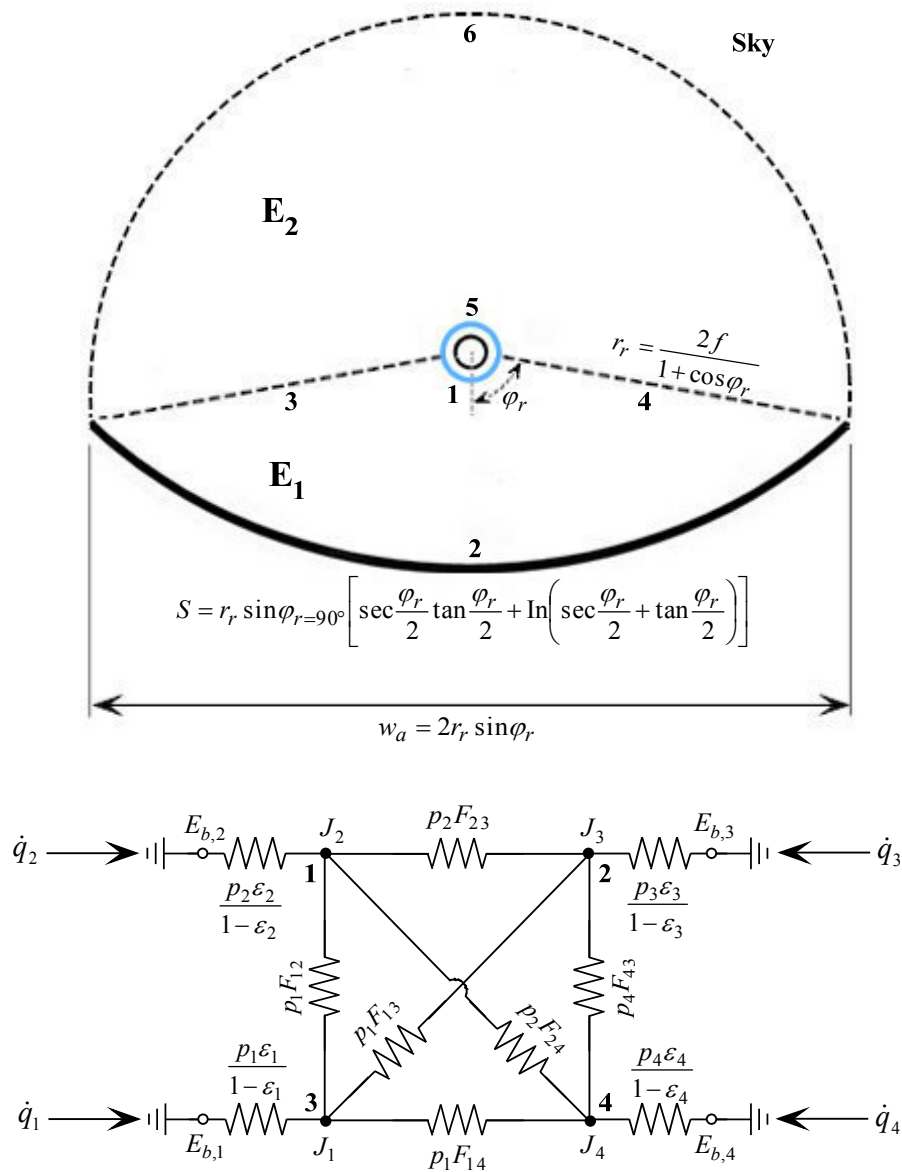


Figure 3.13. Network of the enclosure consisting of four surfaces.

The resistance network of the enclosure consisting of four surfaces is shown in Figure 3.13 and applied to the enclosure E_1 neglecting the side end-effects. For the determination of the N unknown radiosities for an N -surface enclosure, the evaluation of N^2 view factors is required. The relationships specifying the view factors between the surfaces are given in equations (3.60) and (3.61) indicated by the reciprocity and summation rules, respectively. Noting that the view factors can be interrelated with $F_{13} = F_{14}$ and $F_{23} = F_{24}$ using the symmetry rule. For an enclosure

with 4 surfaces there will be 16 view factors. F_{11} , F_{33} and F_{44} can be set to zero since the corresponding surfaces are either flat or convex. The view factor for the parabolic surface to itself was approximated as $F_{22} \approx 1 - 2/\pi$ [50,54].

$$p_i F_{i \rightarrow j} = p_j F_{j \rightarrow i} \quad (3.60)$$

$$\sum_{j=1}^N F_{i \rightarrow j} = 1 \quad (3.61)$$

The radiosities and the net rates of radiation heat transfer at the four surfaces are determined from equation (3.62) and (3.63) applying to the enclosure E_1 and to E_2 but changing the notations for E_2 as analogous in E_1 .

$$\sigma T_i^4 = J_i + \frac{1 - \varepsilon_i}{\varepsilon_i} \sum_{j=1}^N F_{i \rightarrow j} (J_i - J_j) \quad i = 1, 2, 3, \dots, N \quad (3.62)$$

$$\dot{q}_i = p_i \sum_{j=1}^N F_{i \rightarrow j} (J_i - J_j) \quad i = 1, 2, 3, \dots, N \quad (3.63)$$

In this analysis, it was estimated that the surface temperature of the reflector is close to the ambient temperature and the sky temperature was considered as a black body at an equivalent temperature. Although the character of the atmospheric emission is far from blackbody', it can be treated as a blackbody at some lower fictitious temperature that emits an equivalent amount of radiation energy i.e., the effective sky temperature. The sky temperature is expressed with a simple relationship using local air temperature [93].

$$T_{sky} = 0.05532 T_a^{1.5} \quad (3.64)$$

Thus, the radiation transfer between the glass cover and its environment can be interrelated as

$$\dot{q}_{rad,r-s} = \dot{q}_{rad,ref} + \dot{q}_{rad,sky} \quad (3.65)$$

$$\dot{q}_{rad,ref} = p_1 [F_{12}(J_1 - J_2) + F_{13}(J_1 - J_3) + F_{14}(J_1 - J_4)] \quad (3.66)$$

$$\dot{q}_{rad,sky} = p_5 [F_{53}(J_5 - J_3) + F_{54}(J_5 - J_4) + F_{56}(J_5 - J_6)] \quad (3.67)$$

3.3.2 Thermal loss coefficient

The evaluation of the thermal losses requires the estimation of the absorbed solar radiation and the thermal loss coefficient. The solar radiation absorbed by the working fluid can be calculated by multiplying the beam radiation with the optical efficiency of the collector. For the estimation of the thermal loss coefficient, the temperature of the entire surfaces in the radial direction is identified and then the heat transfer coefficients are obtained. In order to find the temperatures of the surfaces, an initial guess is assigned for the outlet temperature of the HTF to generate successive approximations until two consecutive iterations converge to a solution while satisfying the energy balance and the heat transfer relations. For this task, a program code was written in EES Professional V8.581 using its macro tool. The details of the solution algorithm are shown in Appendix F.

When considering the absorber pipe covered and no temperature gradients exist around the receiver, the thermal loss coefficient of the receiver tube can be defined by [72]

$$U_L = \left[\frac{1}{h_{an} + h_{ac}} + \frac{1}{h_{air} + h_{c,sky}} \left(\frac{D_{oa}}{D_{oc}} \right) \right]^{-1} \quad (3.68)$$

where h_{ac} and $h_{c,sky}$ is the radiation heat transfer coefficients. The radiation heat transfer coefficient enables to express analogously the radiation heat transfer in terms of the convection heat transfer [81]. The linearized forms of the radiation coefficient can be calculated from equation (3.69) and equation (3.70) for the annulus and the outside of the cover regions, respectively.

$$h_{ac} = \frac{\sigma(T_{oa} + T_{ic})(T_{oa}^2 + T_{ic}^2)}{\frac{1 - \varepsilon_a}{\varepsilon_a} + \frac{1}{F_{ac}} + \frac{1 - \varepsilon_c}{\varepsilon_c} \left(\frac{D_{oa}}{D_{ic}} \right)} \quad (3.69)$$

$$h_{c,sky} = \sigma \varepsilon_c (T_{oc} + T_{sky})(T_{oc}^2 + T_{sky}^2) \quad (3.70)$$

3.3.3 Useful heat gain and thermal efficiency

Actual useful energy gain is quantified by the collector heat removal factor, F_R which shows the effectiveness of the receiver tube. In other words, it is a measure of the decline in the maximum possible useful energy gain since the whole absorber surface temperature is not at the fluid inlet temperature. It can be defined as [72]

$$F_R = \frac{\dot{m}_{HTF} c_{p,HTF} (T_{m,i+1} - T_{m,i-1})}{w_a [S - U_L (T_{m,i-1} - T_a)]} \quad (3.71)$$

where $S = I_b \eta_o(\theta)$ is the absorbed solar energy for the receiver. It is directly related with the beam radiation falling onto the aperture and the optical efficiency of the collector.

Thus, the useful energy gain transferred to the HTF under steady-state condition can be written in the following form [72].

$$\dot{q}_u = F_R w_a \left[S - \frac{U_L}{C} (T_{m,i-1} - T_a) \right] \quad (3.72)$$

where w_a is the aperture of the parabola.

The exit temperature of the HTF for interior segments can be obtained by using equation (3.21). In the case of constant heat flux, it turns to equation (3.69) due to only sensible heat gain addition to the HTF.

$$T_{m,i+1} = T_{m,i-1} + \frac{\delta \dot{q}_{u,i} P_{ia} \Delta x}{\dot{m}_{HTF} C_{p,HTF}} \quad (3.73)$$

where $T_{m,i-1} = T_{in}$ at the pipe inlet ($i = 1$), and $T_{m,N} = T_{ex}$ at the pipe exit when the useful energy gain is collected by the absorber as $\sum_{i=1}^N \delta \dot{q}_{u,i} P_{ia} \Delta x$ along the receiver.

The thermal efficiency of the PTSC is defined under steady state conditions as

$$\eta_{PTC} = F_R \eta_o C - \frac{F_R U_L (T_{in} - T_a)}{I_b} \quad (3.74)$$

3.4 Model validation

Results of the developed heat transfer model were compared with the test results of SNL [45] and the proposed analytical and numerical models of [50,52,54]. Before applying the current model to the collector module given in Table 3.1, its validness was examined in this section. The test results of SNL were used for comparison at two cases: vacuum and air in annulus. The tests were applied under the solar collector assembly LS-2 placed on the AZTRAK rotating platform at the SNL. Two different selective coatings, cermet and black chrome, were used in these tests. The tests were performed for the cases of full sun and no sun; besides the annulus regions with vacuum intact, lost vacuum and bare tube were analyzed. The tests were performed covering the temperature range from 100°C to 400°C using water and Syltherm 800 as the working fluid. However, the cases used in the experimental were just considered as given in Table 3.6 in order to make the current model comparable with the other models.

Variation in the collector efficiency and the thermal loss are shown in Figure 3.14 and 3.15 with respect to the bulk fluid temperature of the HTF, respectively. As it is seen that the thermal efficiency declines strikingly raising with temperature contrary to the thermal loss when the annulus is filled with air rather than vacuumed. Under vacuum conditions, the developed model gives the most consistent results

among the others when the entire temperature range is considered. The predicted results for the exit temperature of the working fluid and the thermal efficiency of the collector are presented in Table 3.7 and Table 3.8 for both cases. The results for the case of lost vacuum showed a good accordance with the test results and most values are inside the experimental error band relative to the other models especially at higher temperatures. The consistency of the results at higher temperatures is more significant because PTSCs generally operate in temperatures higher than 150°C.

Table 3.5. Specifications for SEGS LS-2 parabolic trough solar collector test [45].

Module size	7.8 × 5 m
Rim angle	70°
Reflector	12 thermally sagged panels
	Second surface silvered
	Low iron glass
Aperture area	Typical reflectivity: 0.93 39.2 m ²
Focal length	1.84 m
Concentration ratio	22.42
Receiver	Evacuated tube design, metal bellows at each end
	Absorber inner diameter: 66 mm
	Absorber outer diameter: 70 mm
	Pyrex glass envelope: Anti reflective coated
	Internal diameter: 109 mm
	External diameter: 115 mm
	Transmittance: 0.95
	Cermet selective surface
	Absorptance: 0.96
	Emittance: 0.14 @ 350°C
Annulus condition	Vacuum intact
	Evacuated annulus pressure: 10 ⁻⁴ Torr
	Lost vacuum
Optical efficiency	Annulus filled with ambient air: 0.83 atm
	0.731 (Vacuum intact)
Heat transfer fluid	0.733 (Lost vacuum)
	Syltherm 800
Test method	Full sun

The root mean square error (RMSE) of the obtained exit temperatures from the test results for vacuum intact and lost vacuum cases were specified as 0.42°C and 0.26°C. And the average percentage errors for the thermal efficiency were obtained as 0.86% and 1.84%. These results can be accounted as quite consistent. The error for the case of lost vacuum is slightly higher than the vacuum intact has. Since the

heat transfer within the annulus by convection has significant effect on the thermal analysis. Nevertheless, the exit temperatures obtained from the model gives more close results with respect to the experimental data. The variation in the coating's emissivity with temperature has also considerable effect on the thermal analysis. The temperature dependence was estimated in the analysis by using the relation, $\varepsilon_a = 0.000327(T + 273.15) - 0.065971$ for the coating type, Luz cermet [45]. In addition that improvement in the temperature dependence on the thermo-physical properties of heat transfer mediums may enhance the model accuracy. Furthermore, the technical data used for Syltherm 800 [94] that were adapted from typical values obtained from production samples might exhibit slightly different specifications from the test conditions of SNL.

Table 3.6. Comparison between the SNL experimental data and the current model: Vacuum intact.

I_b W/m ²	Flow rate l/min	Wind speed m/s	T_a °C	T_{in} °C	T_{ex} °C	Model T_{ex} , °C	Exp. η_{PTSC} , %	Model η_{PTSC} , %	% error exp. vs model
933.7	47.7	2.6	21.2	102.2	124.0	124.32	72.51 ± 1.95	72.37	0.19
968.2	47.8	3.7	22.4	151.0	173.3	173.87	70.90 ± 1.92	71.80	1.27
982.3	49.1	2.5	24.3	197.5	219.5	220.14	70.17 ± 1.81	71.01	1.20
909.5	54.7	3.3	26.2	250.7	269.4	269.57	70.25 ± 1.90	69.47	1.11
937.9	55.5	1.0	28.8	297.8	316.9	317.21	67.98 ± 1.86	67.85	0.19
880.6	55.6	2.9	27.5	299.0	317.2	317.07	68.92 ± 2.06	67.36	2.26
903.2	56.3	4.2	31.1	355.9	374.0	374.45	63.82 ± 2.36	64.04	0.34
920.9	56.8	2.6	29.5	379.5	398.0	398.48	62.34 ± 2.41	62.54	0.32
RMSE						0.42°C		Ave.	0.86%

Table 3.7. Comparison between the SNL experimental data and the current model: Lost vacuum.

I_b W/m ²	Flow rate l/min	Wind speed m/s	T_a °C	T_{in} °C	T_{ex} °C	Model T_{ex} , °C	Exp. η_{PTSC} , %	Model η_{PTSC} , %	% error exp. vs model
813.1	50.3	3.6	25.8	101.2	119.0	118.70	71.56 ± 2.21	69.35	3.09
858.4	52.9	3.1	27.6	154.3	171.7	171.66	69.20 ± 2.10	68.01	1.73
878.7	54.6	3.1	28.6	202.4	219.4	219.42	67.10 ± 1.88	66.31	1.18
896.4	55.2	0.9	30.0	250.7	267.8	267.94	65.50 ± 1.80	65.03	0.72
889.7	55.3	2.8	28.6	251.1	268.3	267.96	66.61 ± 2.29	64.15	3.69
906.7	55.4	0.0	31.7	299.5	316.5	317.01	62.58 ± 1.79	63.17	0.94
874.1	56.2	4.0	28.7	344.9	361.1	360.74	59.60 ± 2.27	57.33	3.81
870.4	56.1	0.6	29.1	345.5	361.6	361.84	59.40 ± 2.12	59.21	0.32
879.5	55.4	1.8	27.4	348.9	365.2	365.34	58.52 ± 2.02	57.99	0.91
898.6	56.2	2.8	29.7	376.6	393.1	393.06	56.54 ± 1.93	55.36	2.09
RMSE						0.26°C		Ave.	1.84%

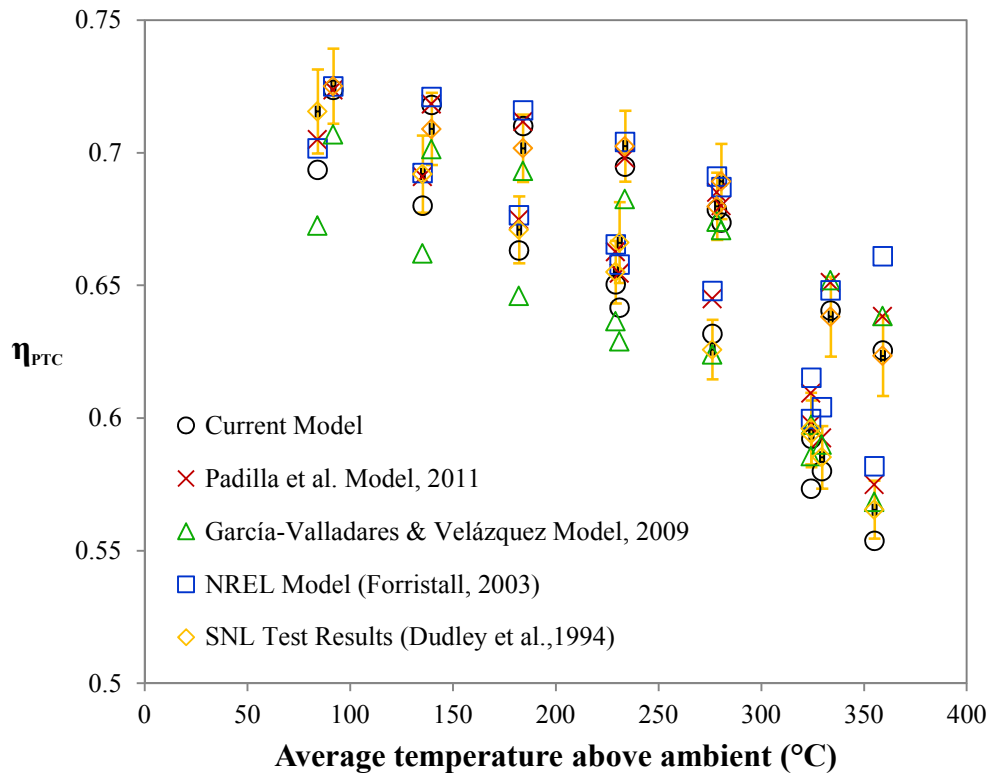


Figure 3.14. Comparison of thermal efficiency with SNL data and the other models.

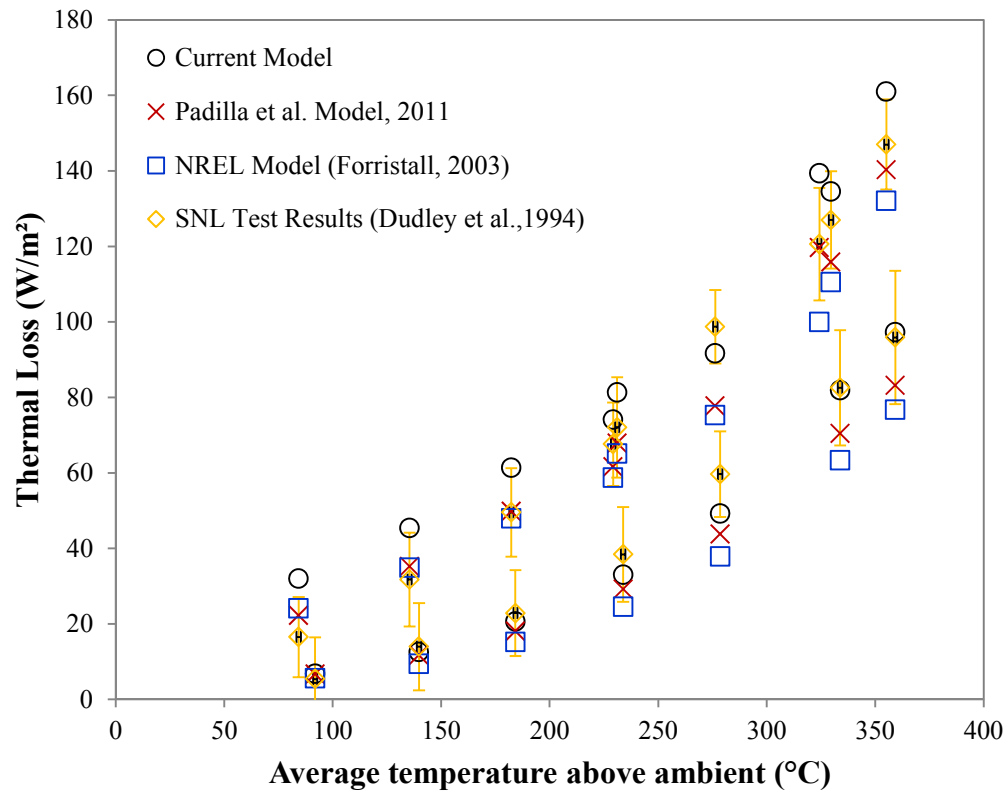


Figure 3.15. Comparison of thermal losses with SNL data and the other models.

Table 3.9. Comparison of RMSE among the model studies.

Model	RMSE	
	η_{PTC} (%)	Thermal Loss (W/m ²)
<i>Vacuum intact</i>		
Current model	0.766	4.638
Padilla et al. model	1.012	10.255
García-Valladares & Velázquez model	1.433	–
NREL model	1.382	14.718
<i>Lost vacuum</i>		
Current model	1.429	11.483
Padilla et al. model	1.225	8.959
García-Valladares & Velázquez model	2.292	–
NREL model	1.562	13.594

A detailed RMSE analysis was made to compare the current model with the Padilla et al., NREL and Garcia-Valladares & Velázquez models as shown in Table 3.9. The current model gave the most accurate values in vacuum intact case as compared with those obtained from the other models. The RMSEs were obtained as 0.766% and 1.429% for collector efficiency, 4.638 W/m² and 11.483 W/m² for thermal loss, respectively. Our proposed model achieved pretty good RMSE values relative to the other models. The improvement in the lost vacuum case gave better results relative to NREL and Garcia-Valladares & Velázquez models and close value compared to Padilla et al. model.

3.5 Performance parameters

The thermal performance of a PTSC is affected by working conditions under which it operates. There are many system parameters which play roles on the optical and the thermal properties of the PTSC. Thus the model was analyzed under different operating conditions to view the system behavior at different scenarios. This model was applied to the collector module whose technical specifications were given in Table 3.1.

The useful heat gain is important to determine the outlet temperature and the net energy transfer to the working fluid. Moreover, it is quite essential for sizing,

designing and making energy policy of a thermal system operated by PTSC. Using a typical beam radiation measured in the summer solstice for Gaziantep, the heat gain and the loss components of the PTSC which were obtained from the model as shown in Figure 3.16. The total energy loss from the collector comprises the optical and the thermal losses. As it is seen, the optical loss increases and reaches maximum level, due to the effect of incidence angle, at local solar noon then decreases almost symmetrically after noon. Since the geometric factor of the collector and the cosine losses are the most affected parameters by the angle of incidence, they play dominant role for increasing the optical loss. The cosine of the incidence angle is related to the orientation of the collector. If the orientation were chosen as East-West, the incidence angle would have much lower values at solar noon in summer season. However the collector performance, during the early and late hours of the day, is greatly reduced for this orientation due to large cosine losses. As it is seen from Figure 3.16, the thermal loss is nearly constant throughout the day owing to the fact that it is affected only by the operating bulk fluid temperature under steady conditions.

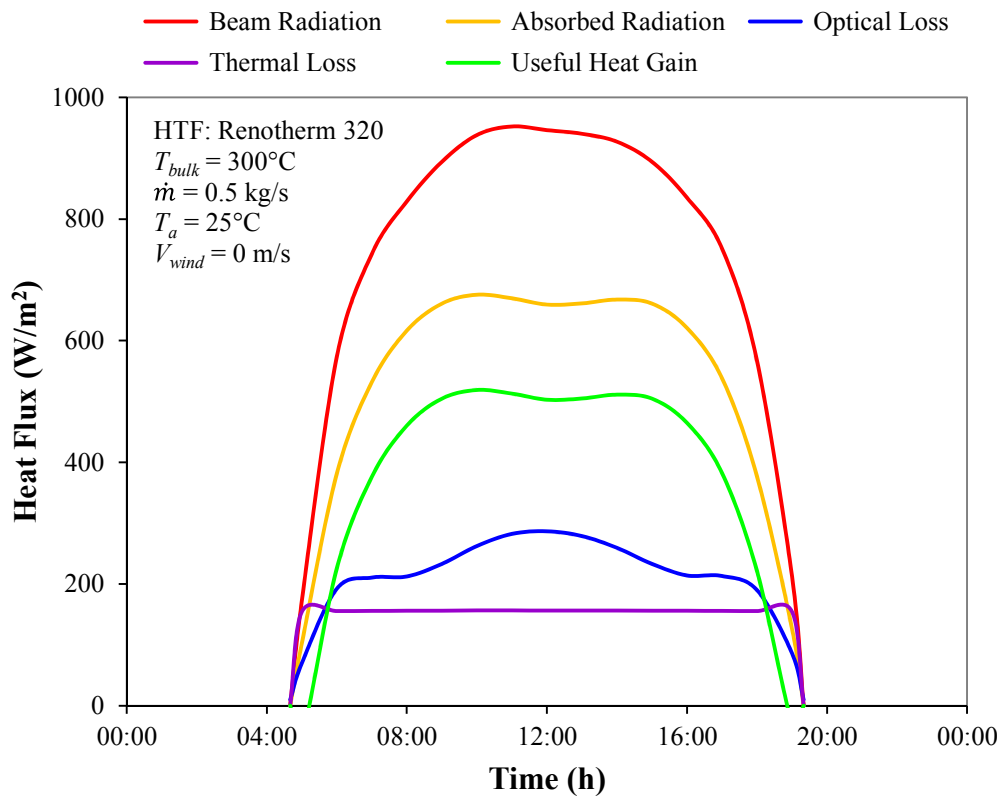


Figure 3.16. Heat gain and lost components for the collector.

The effect of the optical parameters on the optical loss is shown in Figure 3.17 with respect to local solar hour. The optical parameters, apart from the geometric factor and the cosine losses, are more stable against the variation of the incidence angle. While the variation in the geometric losses and the cosine losses during the summer solstice (except very early hours) are within the range of 2.8–17.5% and 0.3–15% respectively, the maximum variation in the remaining optical parameters stands below 2%.

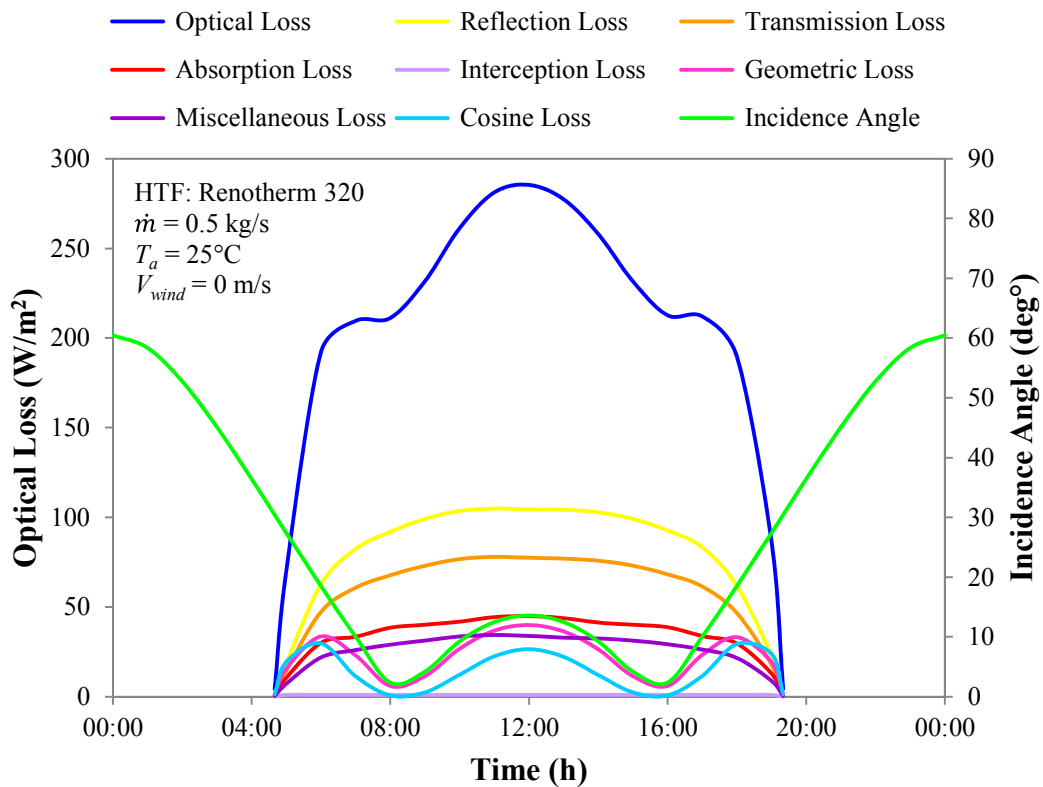


Figure 3.17. The effect of the optical parameters on the optical loss.

Figure 3.18 shows the temperature distribution in the radial direction of the receiver with respect to the inlet temperature of the HTF. The highest temperature occurs at the outer surface of the absorber pipe due to absorption of beam radiation. The heated surface transfers the energy through the absorber pipe whose inner surface temperature falls due to convection heat transfer by the flowing HTF. The condition of the heat transfer in the annulus region specifies the magnitude of the temperature inside the glass cover. If the annulus region is vacuumed, the outer surface of the cover will fall remarkably. The glass envelope reduces heat transfer by thermal radiation and convection and thus remains at a lower temperature.

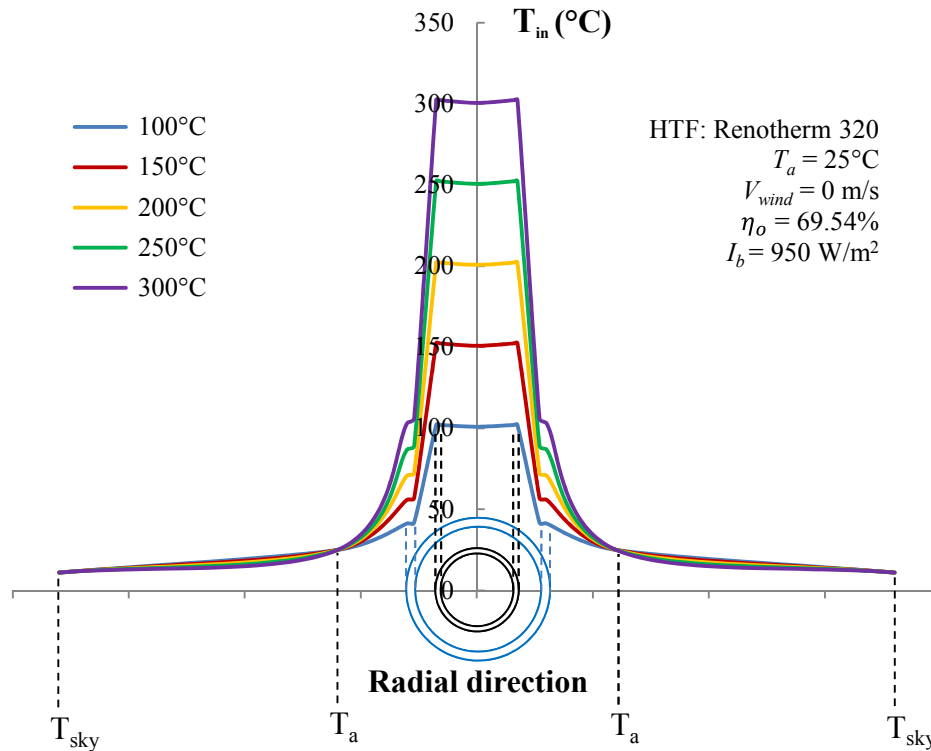


Figure 3.18. Temperature profiles in the receiver tube.

Figure 3.19 illustrates the variation in each component of the thermal loss increasing with bulk fluid temperature. It also identifies the fractions over the thermal loss and provides a facility to visualize their effects on the thermal efficiency. As it is expected that the convection heat loss generated from the HTF has the biggest part of the thermal loss since the highest temperature occurs at the outer surface of the absorber pipe. The temperature decreases through the radial direction and has the minimum value at the outside of the cover. The heat transfer rates inside and outside of the receiver depend strongly on the thermophysical properties of the optical elements and the condition of the annulus. When the annulus is vacuumed, the outside temperature of the cover falls remarkably thus the thermal loss from the receiver lowers significantly relative to the case of lost vacuum. Another way of reducing convection heat transfer through the annulus is to use a less-conducting fluid such as argon or krypton instead of air as seen in Figure 3.20. The gap in this case needs to be well sealed to prevent the gas from leaking outside. Filling the annulus space with an inert gas instead of a vacuum could result in higher reliability and help to lessen the hydrogen permeation problem [50]. The improvement in the thermal efficiency over air is obtained as 6.25% at 300°C when krypton is used. In fact, the outdoor conditions (ambient temperature, wind speed etc.) also affect the

thermal losses in negative sense but their effect can be minimized possibly selecting a proper site for installation.

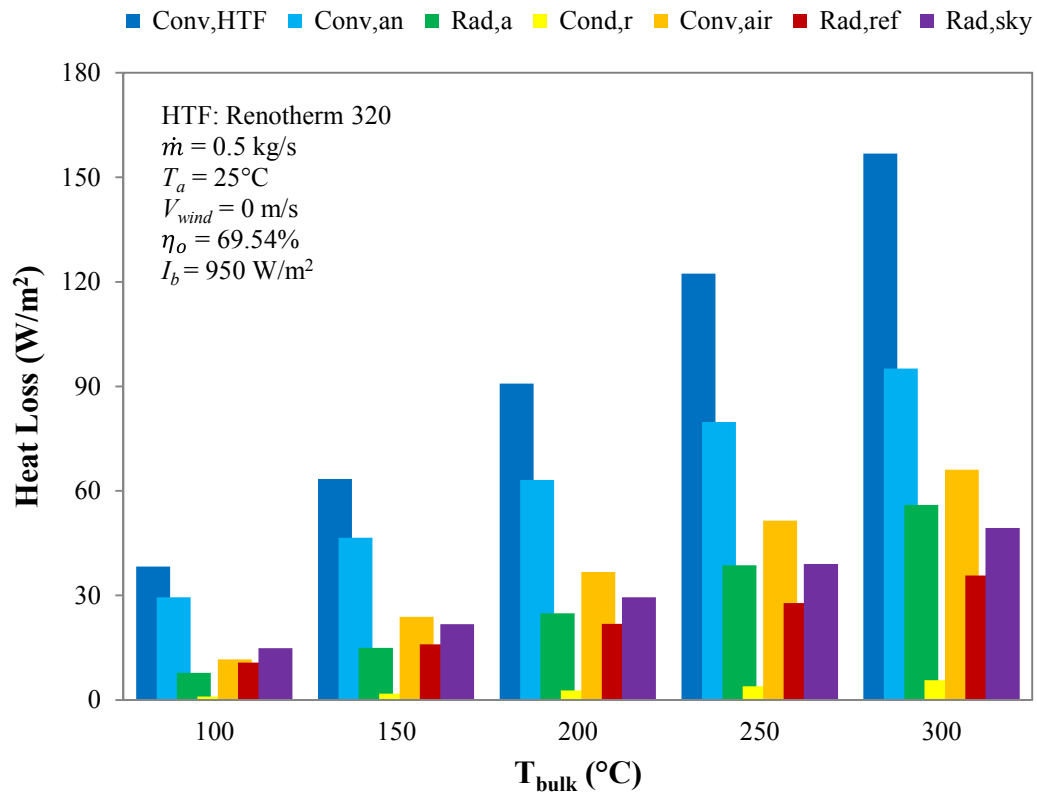


Figure 3.19. Heat loss components of the receiver tube.

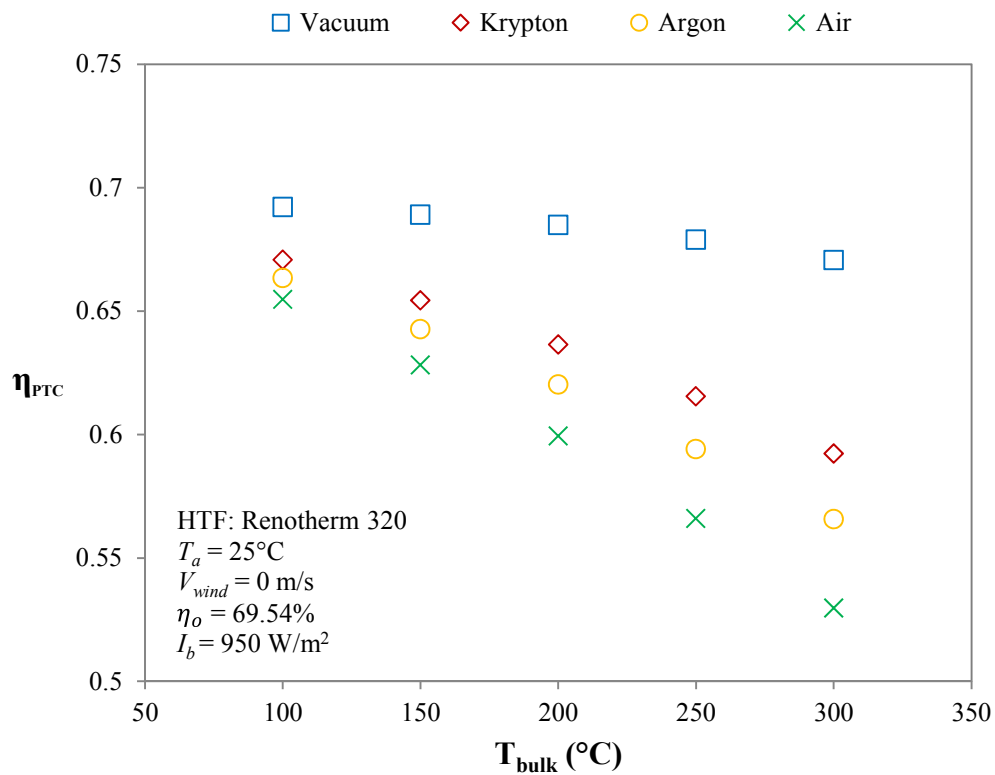


Figure 3.20. Variation of thermal efficiency under different annulus conditions.

Figure 3.21 points out the variation of mass flowrate and its effect on the thermal efficiency. It is seen that the increase in mass flowrate enhances the thermal efficiency. At lower flow rates and temperatures, the regime of the flow may turn to laminar or transition regime which degrades the convection heat transfer coefficient within the absorber pipe hence the thermal efficiency of the collector drops severely as seen in Figure 3.21.

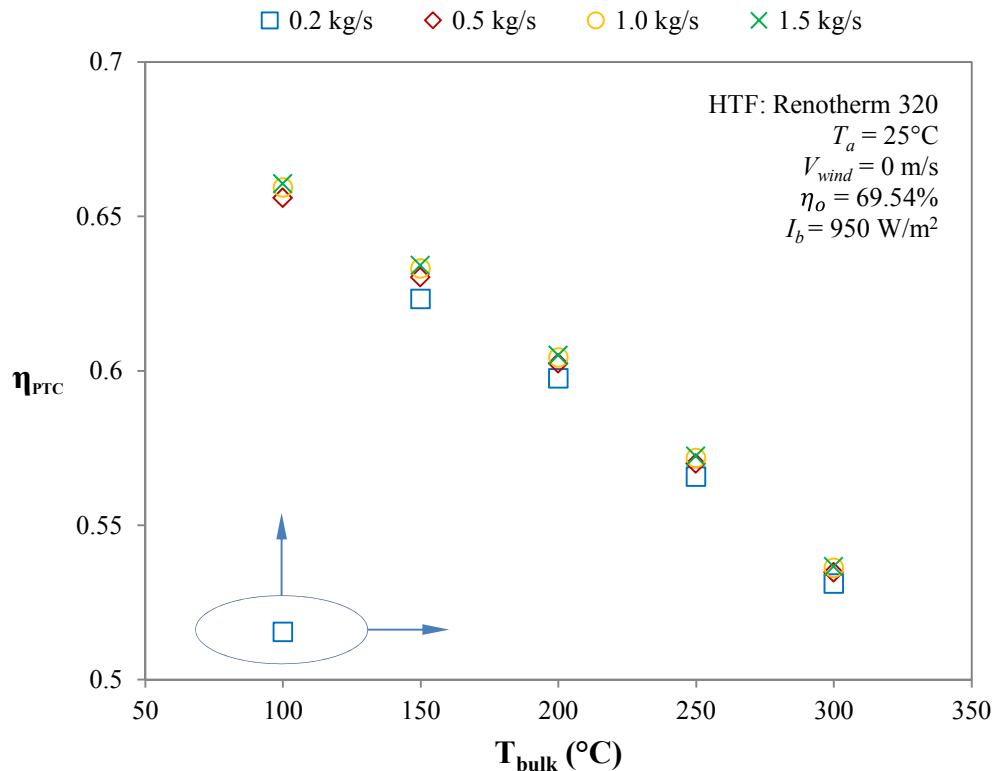


Figure 3.21. Effect of mass flowrate on thermal efficiency.

The thermal efficiency has increased lower than 1% as a result of the change in the mass flowrate from 0.2 to 1.5 kg/s at 300°C. Since this change occurs by increase in the mass flowrate which causes to develop turbulent currents within the absorber pipe so that the HTF transfers more energy from the inner surface of the pipe. The higher the mass flowrate, the higher the fluid motion or Re which in turn increases the convection heat transfer coefficient of the HTF. This leads the inside temperature of the absorber to fall down thus the useful heat gain transferred to the fluid has increased due to lowering the thermal loss. However, increasing the mass flowrate requires much pumping work thus the optimal mass flowrate is needed to keep the pump work minimum for the sake of raising the thermal efficiency. The optimum

mass flowrate, \dot{m}_{opt} was defined as 0.7 kg/s using equation (3.75) over the range of bulk fluid temperature. After this value, increase in the mass flowrate requires more power for pumping rather than transfer power as useful heat gain to the HTF. Raising the operating temperature of HTF increases the Re and consequently the convection currents within the absorber. Note that the type of HTF and its operating temperature have also important effects on the optimum mass flowrate.

$$\dot{m}_{opt} = \frac{w_a I_b \Delta \eta_{PTC, \Delta \dot{m}} \eta_{pump}}{\frac{f}{D_{ia}} \frac{u_m^2}{2}} \quad (3.75)$$

where $\Delta \eta_{PTC, \Delta \dot{m}}$ is the increment of the thermal efficiency between subsequent mass flowrate values and η_{pump} is the efficiency of the pump which can be typically taken as 0.85.

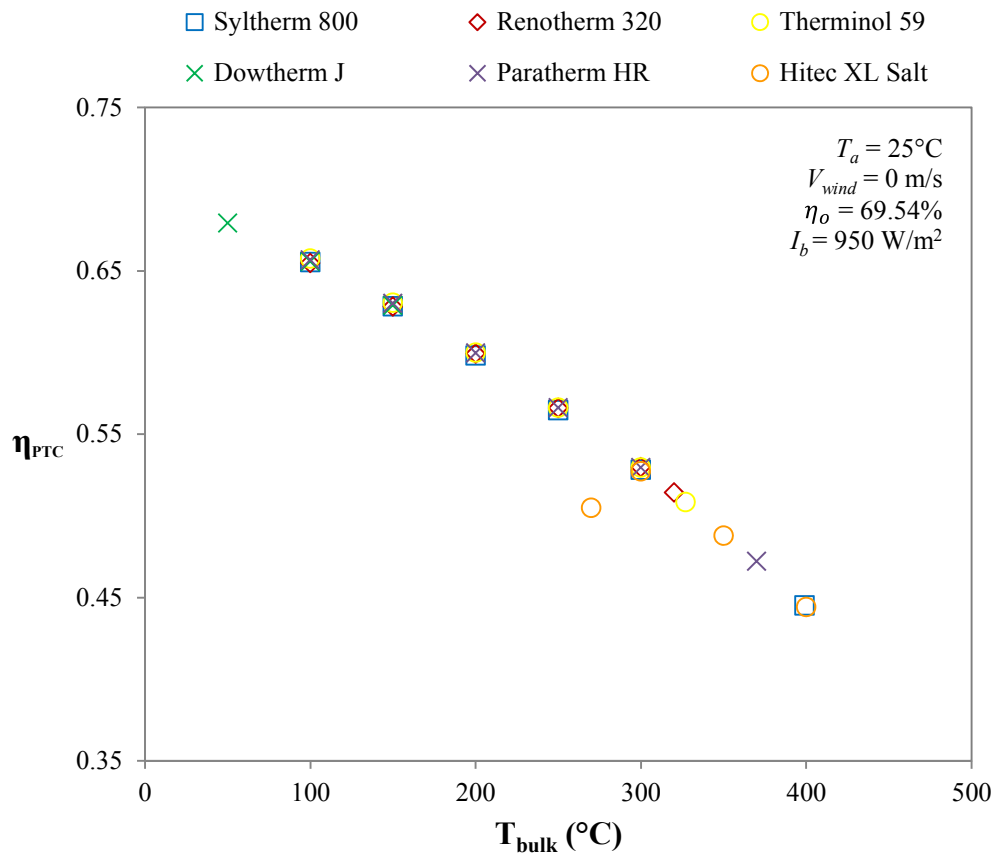


Figure 3.22. Effect of HTF type on thermal efficiency.

Figure 3.22 reveals that the type of the HTF [94] has almost insignificant effect on the enhancement of the thermal efficiency. As it is expected, increasing of bulk temperature increases the heat loss, and drops the efficiency. Thus, fluids that can operate at lower temperatures would improve the collector performance. However, each HTF has a range of operating temperature that is provided by the producer. For instance, thermal oils are generally operated at high temperatures about 200–300°C to lower the viscosity, but functioned below its recommended film temperature not to undergo thermal cracking. Molten salts can be used as thermal storage media, but also could require additional heating during off-sun hours to prevent solidification in installations. Thus, operating temperature should be selected according the maximum system efficiency that is to be obtained.

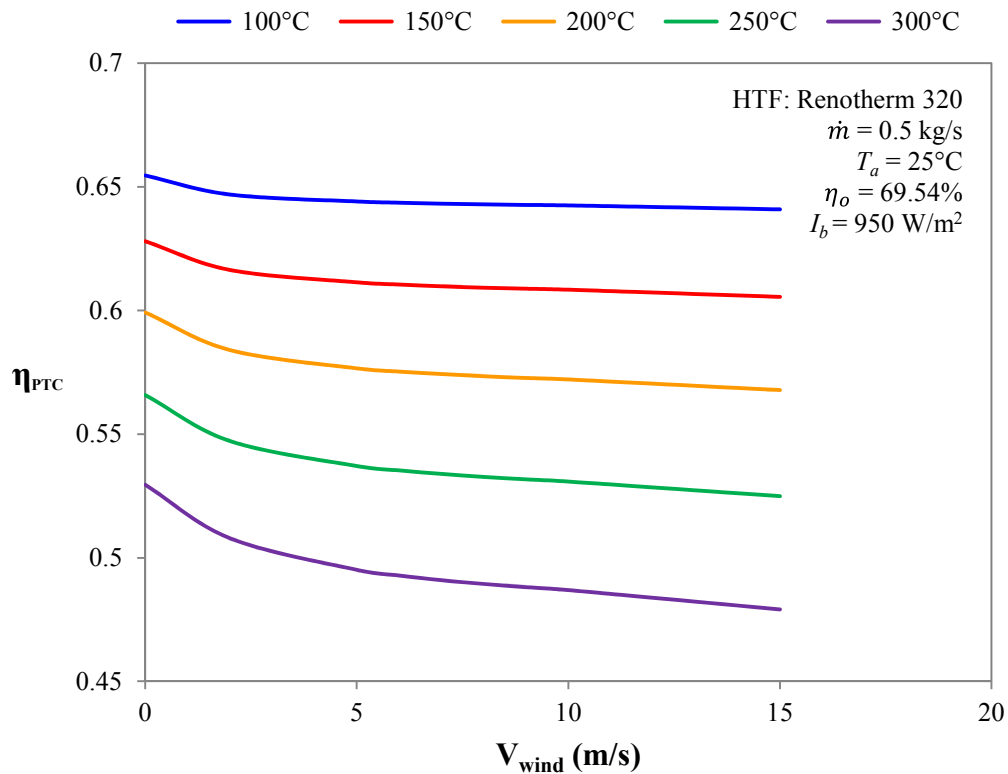


Figure 3.23. Effect of wind speed on thermal efficiency.

Figure 3.23 shows the effect of wind speed on the thermal efficiency of the collector. The model results specify that the effect of wind is considerable over those higher speeds when the PTSC is operated at relatively high temperatures. The maximum wind speed has been defined as 15 m/s since such elevated speeds are not usual case on the earth surface. As it is seen from Figure 3.23, the thermal efficiency declines nearly 5% when the wind speed rises from 0 m/s to 15 m/s at 300°C due to

the increase in the convection currents at higher temperatures and Reynolds numbers. For the case of vacuumed annulus, the thermal efficiency is much slightly affected by wind since the outside temperature of the cover surface approaches the temperature of ambient air thus the thermal loss from the receiver reduces.

3.6 Summary

The collector efficiency of a PTSC depends on many factors which can be basically collected into four groups as design, construction, installation and operation. For a designed and constructed PTSC, the installation takes an important role on site selection (potential of beam radiation) and orientation of the PTSC (North–South or East–West configuration). On the other hand, the thermal efficiency of the PTSC is affected by the previous factors mentioned and the parameters such as properties of the radiative and optical elements, receiver type (gas-filled or vacuumed), tracking mode and working conditions (such as operating temperature of HTF). In this chapter, thermo-mathematical modeling of a PTSC was developed comprehensively to simulate its physical behavior under different operating conditions. The model study included a complete analysis of optical and thermal characteristics of a PTSC. Moreover, the physical behavior of the PTSC under different operating conditions was explained clearly. The developed heat transfer model was compared with the test results of SNL and the other models [50,52,54] for vacuum intact and lost vacuum cases. The results obtained for both cases were in accordance with SNL and exhibited well consistency particularly for vacuum intact case in comparison with those models. Based on the results obtained, it is concluded that this model is suitable for the calculation of the collector efficiency and thermal losses under different operating conditions.

CHAPTER 4

THERMAL ANALYSIS OF SYSTEM COMPONENTS

4.1 Introduction

In this chapter, the developed thermal analyses for each component of the SAPH application are presented in detail. Physical insight of cooking phenomena is described, and the mathematical modeling for cooking process of wheat is performed. In addition, the working principle of brazed plate heat exchanger (BPHE) is explained, and a procedure for the determination of the heat transfer rate and the outlet temperatures of the hot and cold fluids for prescribed fluid mass flow rates and inlet temperatures are predicted by the method of *Number of Transfer Unit* (NTU). Furthermore, design criteria for TET, and a method of estimating heat losses are presented. Finally, pipe headers and receiver tube of PTSC are analyzed in terms of thermal inertia concept for transient (unsteady) operating condition.

4.2 Analysis of water preheating tank

Process-water for cooking operation is initially heated in water preheating tank (WPT) which serves as a coiled heat exchanger (CHE). Two identical WPTs are used. One is to preheat the process-water for cooking process; the other one is to backup thermal energy for the subsequent cooking processes. The WPT is custom designed and has a storage capacity of 60 L in which a coiled pipe exists as shown in Figure 4.1. The HTF (see Appendix A), which flows inside the coiled pipe, transfers thermal energy to the water charged into the WPT. In addition, the outer side of the WPT is well insulated to minimize the heat loss. The technical specifications of WPT are given in Table 4.1.

Table 4.1. Specifications of the WPT.

Sheet material [94]	316L SS
Inside tank diameter, $D_{i,t}$	0.4 m
Thickness of tank material, t	0.002 m
Pipe material [94]	304L SS
Pipe diameter, $D_{i,p} / D_{o,p}$	0.0157/0.0213 m
Effective heat transfer area, A_s	0.0735 m ²
Insulation thickness	0.04 m
Insulation material [95]	Stone wool

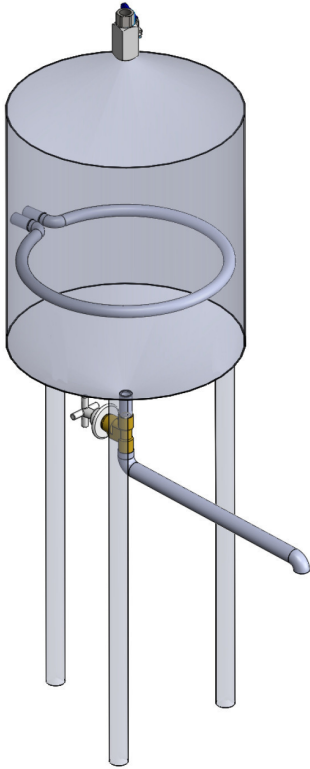


Figure 4.1. Water preheating tank.

The energy balance on a water storage unit at uniform temperature (i.e., fully mixed, or unstratified) is given by

$$(mc_p)_w \frac{dT_w}{dt} = \dot{Q}_p - (UA)_p (T_w - T_a) \quad (4.1)$$

Equation (4.1) is integrated over time to determine the energy transfer to the water (see Appendix C) [96] in the WPT. Water temperature at the end of a time increment is obtained as

$$\int_0^{t+\Delta t} \frac{dT_w}{T_w - T_a - \frac{\dot{Q}_p}{(mc_p)_w (UA)_p}} = -\frac{1}{(UA)_p} \int_0^{t+\Delta t} dt \quad (4.2)$$

from which it follows that the general solution is

$$T_w(t + \Delta t) = T_a + \frac{\dot{Q}_p}{(mc_p)_w (UA)_p} + \left(T_w(t) - T_a - \frac{\dot{Q}_p}{(mc_p)_w (UA)_p} \right) e^{-\frac{\Delta t}{(UA)_p}} \quad (4.3)$$

where

$$(mc_p)_w = (mc_p)_{pw} + (mc_p)_t + (mc_p)_{ins} \quad (4.4)$$

$$\dot{Q}_p = (\dot{m}c_p)_{HTF} (T_{in} - T_{ex}) \quad (4.5)$$

The exit temperature of the HTF is predicted by evaluating the pipe surface that is exposed to boundary condition of constant temperature.

$$T_{ex} = T_s + (T_s - T_{in}) e^{-\frac{h_i A_s}{(\dot{m}c_p)_{HTF}}} \quad (4.6)$$

The coiled pipe is treated as horizontal straight pipe since it is composed of one single coil. In this case, the Nu relation inside a circular smooth pipe is defined by the Gnielinski equation [97] which covers the transition and the turbulent regions together for fully developed turbulent flow.

$$Nu_i = \frac{f/8(\text{Re}_{HTF} - 1000)\text{Pr}_{HTF}}{1 + 12.7\sqrt{f/8}(\text{Pr}_{HTF}^{2/3} - 1)} \left(\frac{\text{Pr}_{HTF}}{\text{Pr}_w} \right)^{0.11} \quad \begin{array}{l} 0.5 \leq \text{Pr} \leq 2000 \\ 2300 < \text{Re} < 5 \times 10^6 \end{array} \quad (4.7)$$

where f is the friction factor, $f = (0.79 \ln \text{Re}_{HTF} - 1.64)^{-2}$ for smooth pipes [81].

The convection heat transfer coefficient within the coiled pipe is obtained from

$$h_i = \text{Nu}_i \frac{k_{HTF}}{D_{i,p}} \quad (4.8)$$

The heat transfer over the coiled pipe can be defined only by natural convection since the effect of radiation can be neglected. The boundary layer over a hot horizontal cylinder starts to develop at the bottom, increasing in thickness along the circumference, and forming a rising plume at the top. Therefore, the local Nu is highest at the bottom, and lowest at the top of the cylinder when the boundary layer flow remains laminar. The average Nu over the entire surface can be determined from equation (4.9) for an isothermal horizontal cylinder [98]:

$$\text{Nu}_o = \left[0.60 + 0.387 \left(\frac{\text{Ra}_D}{\left[1 + (0.559/\text{Pr})^{9/16} \right]^{6/9}} \right)^{1/6} \right]^2 \quad (4.9)$$

The convection heat transfer coefficient at the outside of the CHE is

$$h_o = \text{Nu}_o \frac{k_w}{D_{o,p}} \quad (4.10)$$

The outer surface of the pre-heat tank can be approximated as vertical plate since the diameter of the cylinder is sufficiently large so that the curvature effects are negligible when $D \geq 35L/\text{Gr}_L^{1/4}$. Under this conditions, the average Nu relation for an isothermal vertical plate can be evaluated using the equation recommended by [99]:

$$\text{Nu}_{air} = \left[0.825 + \frac{0.387\text{Ra}_L^{1/6}}{\left[1 + (0.492/\text{Pr})^{9/16} \right]^{8/27}} \right]^2 \quad (4.11)$$

Noting that all fluid properties are to be evaluated at the film temperature, $T_f = (T_p + T_a)/2$.

For the analysis of heat loss from the pre-heat tank, it is convenient to combine all the thermal resistances in the path of heat flow from the hot water to the ambient air into a single resistance $(UA)_p$,

$$\frac{1}{(UA)_p} = \frac{1}{h_o A_{i,t}} + \frac{\ln(D_{o,t}/D_{i,t})}{2\pi L k_t} + \frac{\ln(D_{o,ins}/D_{i,ins})}{2\pi L k_{ins}} + \frac{1}{h_{air} A_{o,t}} \quad (4.12)$$

4.3 Analysis of cooking pot

Cooking is the initial step for the production of some wheat-based cereal products. Typically, grains are first processed by heating them at some elevated temperature and pressure. After cooking the grains are soft enough to be worked into the final product. It is important to optimize the cooking process as it underpins all subsequent operations. At this stage, it is crucial to obtain a product of the desired quality at lowest cost. This requires an understanding of the cooking process which involves both the diffusion of water into the grain and the subsequent conversion (reaction) of the starch within it i.e., gelatinization. The literature on cooking model for wheat is limited and is largely based on the effects of cooking time, temperature, and starch gelatinization. Stapley et al. [100] studied the boiling of whole wheat grains using magnetic resonance imaging (MRI) and pulsed-gradient-spin-echo nuclear magnetic resonance (PGSE NMR). Magnetic resonance imaging was used to image moisture distributions across a central section of grains boiled for different times at either 100°C or 120°C. Diffusion models suggested from the PGSE results were incorporated into finite-element simulations and tested with a number of different model scenarios to compare the simulation results to the MRI data. Watanabe et al. [101] proposed a new mathematical model to describe the characteristic features of the change of moisture profile in starchy food during boiling. Bayram [16] used three gelatinization measuring methods to control the cooking of wheat (*Triticum durum*) for bulgur processing. The optimum cooking time for wheat was determined as 40 min providing 100% gelatinization without any deformation on the wheat kernel. Pressure cooker is an appliance that cooks foods reducing the cooking time required relative to ordinary pots maintaining a higher pressure and temperature during cooking. Using saturated steam (without oxygen)

and reducing cooking time are the two ways of preserving vitamins [102]. Some studies have shown that pressure cookers have many nutritional, organoleptic and sanitary advantages however studies on these subjects that have been put forward so far are not quietly sufficient. In this study field, Koca and Anil [103] investigated the effects of different wheat kinds and cooking methods on physical, chemical and organoleptic traits of bulgur but their study did not include how the cooking method exhibits such advantages mentioned above.

Cooking is a type of process which involves boiling that occurs at the solid-liquid interface when a liquid is brought into contact with a surface maintained at a temperature, T_s sufficiently above the saturation temperature, T_{sat} of the liquid. The boiling process is characterized by the rapid formation of vapor bubbles at the solid-liquid interface that detach from the surface when they reach a certain size and attempt to rise to the free surface of the liquid. The energy demand for this process is generally provided by electrical or thermal power. For large applications, thermal energy is used in usual. The thermal energy transfer to the liquid is realized by a heat exchanger which facilitates the exchange of heat between the two fluids separated by a solid wall while keeping them from mixing with each other. Heat is first transferred from the hot fluid to the wall by convection, through the wall by conduction, and from the wall to the cold fluid again by convection. It is the basic heat transfer mechanism of boiling process to be used for cooking facility.

4.3.1 Description of cooking mechanism

The process water is firstly preheated in the pre-heat tank from its initial temperature to the final temperature of 90°C, and then it is discharged into the cooking pot (CP). The temperature of the preheated water falls down when it is mixed with the unsoaked wheat grains (initially at about ambient temperature) inside the pot. After discharge-process, the mixture is heated up until the cooking temperature reaches the boiling temperature. The degree of cooking temperature is adjusted according to the condition of starch gelatinization since the degree of gelatinization of hard wheat starch depends strongly on cooking temperature. The rate of the gelatinization increased with increasing cooking temperature [104,105],

and it is never completed 100% at cooking temperatures lower than 90°C as shown in Figure 4.2. The temperature inside the CP is controlled by a pressure relief valve that keeps the pressure at the corresponding boiling temperature by periodically allowing some steam to escape, thus preventing any excess pressure buildup. When the boiling begins, energy requirement for cooking operation is lowered. At this stage, the supplied energy is decreased only to be able to keep the cooking temperature at the central region of the mixture constant.

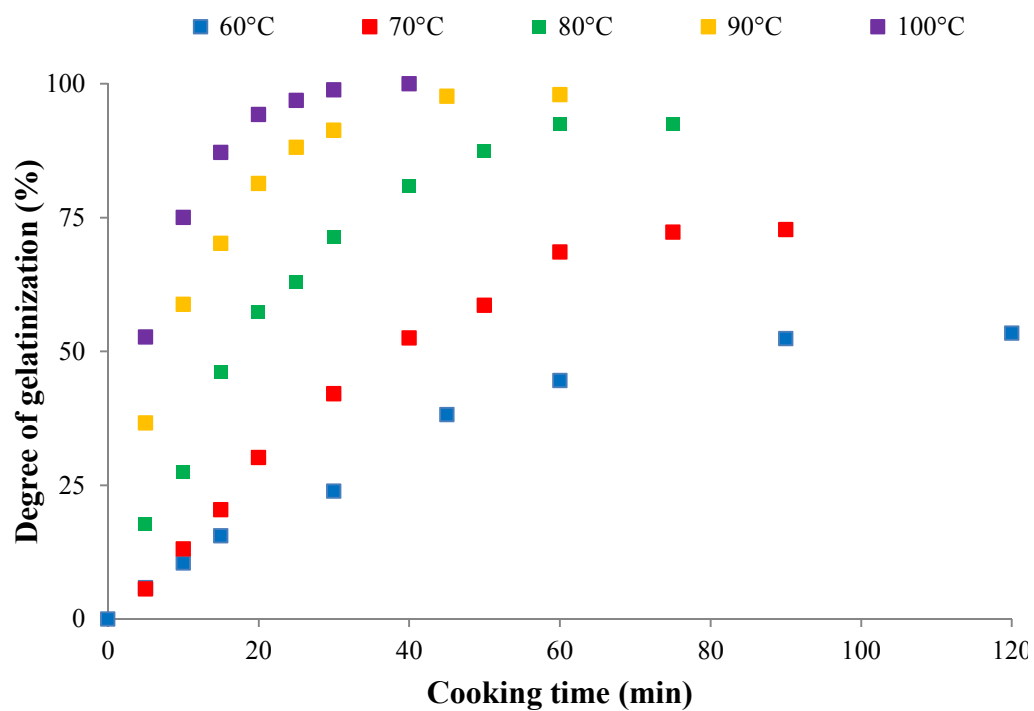


Figure 4.2 Progress of the gelatinization of the hard wheat starch at different cooking temperatures [106].

4.3.2 Thermal modeling of cooking

The detailed drawing of the CP to be modeled is demonstrated in Figure 4.3. The CP is custom designed, and its specifications are introduced in Table 4.2. A screen made of perforated sheet metal is placed into the CP not to directly contact wheat grains in the screen with the coiled pipe. Thus the wheat grains will not adhere to the surface of the coiled pipe whose temperature is high due to the HTF flowing inside it. In other words, the coiled pipe is surrounded only by water which is intended to be exposed to the direct heat transfer while the wheat grains are heated in the screen. The outer side of the CP is well insulated to minimize the heat loss.

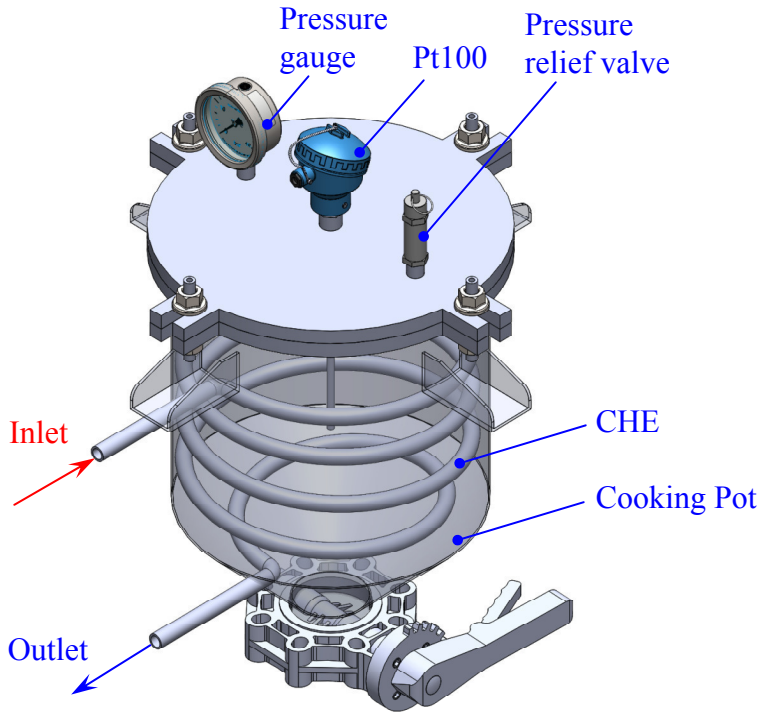


Figure 4.3. CP with internally helicoidal heat exchanger (IHHE).

Table 4.2. Specifications of the IHHE.

Sheet material [94]	316L SS
Inner pot diameter, $D_{i,t}$	0.4 m
Material thickness, t	0.002 m
Pipe material [94]	304L SS
Pipe diameter, $D_{i,p} / D_{o,p}$	0.0157/0.0213 m
Coil pitch, b	0.085 m
Coil radius, R	0.175 m
Effective heat transfer area, A_s	0.288 m ²
Insulation material [95]	Stone wool

4.3.3 Heating process of mixture (Sensible heat gain)

The preheated water is discharged onto the wheat grains, and it is heated from the mixture temperature, T_m to the boiling temperature, T_b . This heating process is named as subcooled or local boiling because the temperature of the main body of the liquid is below the saturation temperature, T_{sat} . At the early stages of boiling, the bubbles are confined to a narrow region near the hot surface. This is because the liquid adjacent to the hot surface vaporizes as a result of being heated above its saturation temperature. However, these bubbles disappear soon before reaching the

liquid-gas interface as a result of heat transfer from the bubbles to the cooler liquid surrounding them. In this case, only sensible heat gain is considered for the heating process, and the final temperature of the mixture of water and grain can be calculated using energy balance equation:

$$m_g c_{p,g} (T_m - T_g) = (m_w + m_e) c_{p,w} (T_w - T_m) \quad (4.13)$$

The sensible energy demand for the mixture to reach the boiling temperature can be defined by

$$Q_s = (m_w + m_e) c_{p,w} (T_b - T_m) + m_g c_{p,g} (T_b - T_m) \quad (4.14)$$

During preheating process, some water will penetrate into the grains so that the amount of process-water will decrease, and the moisture within the grains will increase with time. Thus, the specific heat of the grain samples will change through the temperature rise from T_m to T_b . The value of $c_{p,g}$ is estimated by the relation as [107]

$$c_{p,g} = c_{p,d} + c_{p,w} W \quad (4.15)$$

4.3.3.1 Mass transfer by evaporation

Transition from subcooled boiling to saturated boiling during heating process, mass transfer by evaporation occurs at the liquid-gas interface as a result of water molecules diffusing into the air confined in the CP. It continues up to the boiling temperature until the phase equilibrium is maintained since the vapor pressure at the mixing temperature is less than the saturation pressure of the liquid. The basic theory for estimating the evaporated water and the corresponding heat loss is clarified at Appendix G in detail.

$$\frac{dm_{ev}}{dt} = -AD \frac{1}{L-H} \left(\frac{M_w P_s^{vs}}{RT} \right) (1-\phi) \quad (4.16)$$

4.3.3.2 Energy transfer to process-water

The flow inside the pipe is stated by forced circulation due to pumping of the HTF. The single control parameter is the Reynolds number, which determines the dynamical state of the system. Hence when $Re < Re_c$, all initial conditions are attracted to the laminar state, which is the global attractor for the system. When $Re \gg Re_c$, nearly all initial conditions give rise to turbulence so that the laminar state becomes a local attractor. In practice, $Re_c \lesssim 1800$ so that all disturbances will decay as the time extends to the very long periods for values of Re smaller than this [108]. Turbulence appears abruptly above a well-defined finite-amplitude threshold for $Re \gtrsim 3000$, but the disordered motions come out in localized regions called *puffs* in the range of $1760 \lesssim Re \lesssim 3000$ as shown in Figure 4.4.

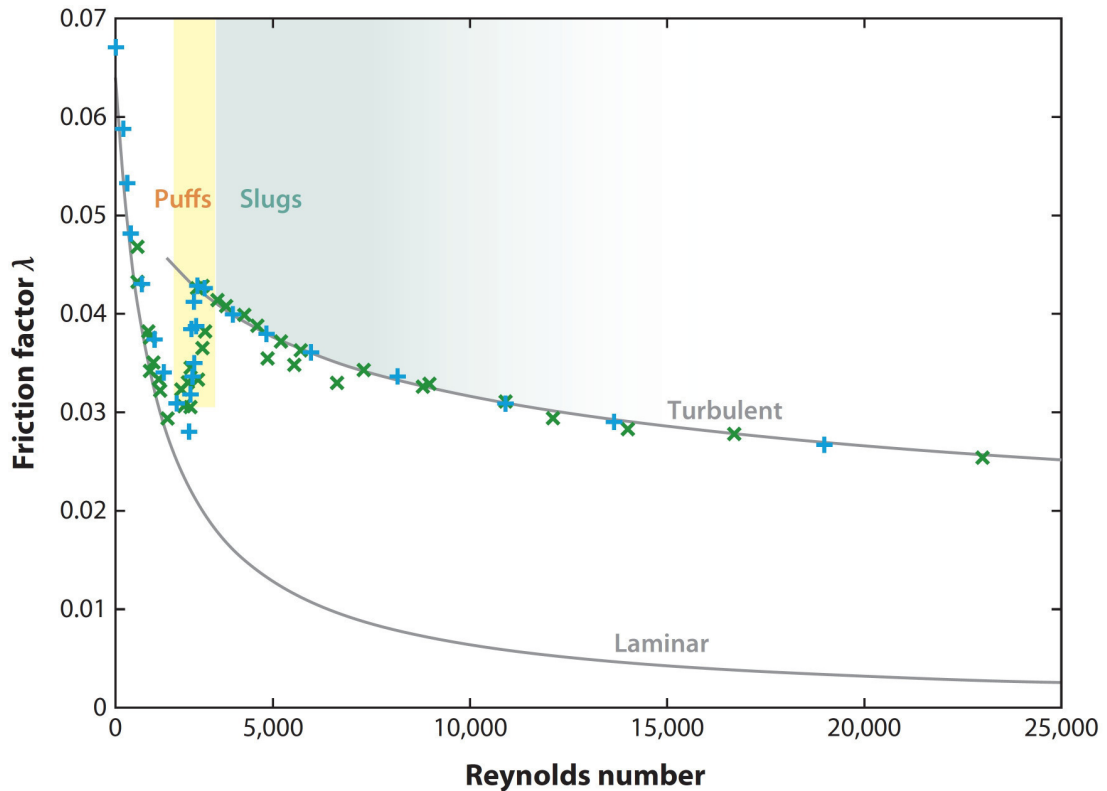


Figure 4.4. Variation of friction factor with Re in the region of puffs [108].

In order to calculate Re , the value of the average velocity u_m at some streamwise cross-section is determined from the requirement that the conservation of mass principle be satisfied.

$$\dot{m}_{in} - \dot{m}_{out} = \frac{dm_{cv}}{dt} \quad (4.17)$$

where \dot{m}_{in} and \dot{m}_{out} are the total rates of mass flow into and out of the control volume, and dm_{cv}/dt is the time rate of change of mass within the control volume boundaries. During a steady-flow process, the total amount of mass contained within a control volume does not change with time ($m_{cv} = \text{constant}$). Then the conservation of mass principle requires that the total amount of mass entering a control volume equal the total amount of mass leaving it.

Equation (4.17) reduces to equation (4.18) when it is applied to single-stream steady pipe flow shown in Figure 4.5.

$$\dot{m}_{in} = \dot{m}_{out} \rightarrow (\rho u_m A)_{in} = (\rho u_m A)_{out} \quad (4.18)$$

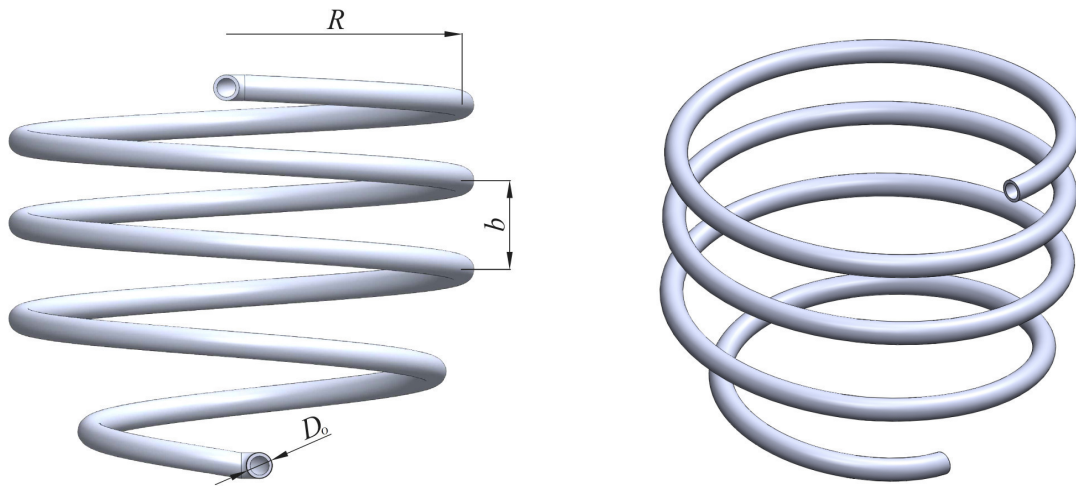


Figure 4.5. Geometry of the IHHE.

Curved or helicoidal pipes are widely used in engineering applications such as food processing. Dean [109,110] first studied the velocity profile of flow in helicoidal pipes using perturbation analysis. His result is valid only for $De < 20$, where the velocity distribution is almost identical to that found in straight ducts. The most prominent characteristic of flow in helicoidal pipes is the secondary flow induced by centrifugal force which enhances the heat transfer rate. Consequently, the friction factor is higher in curved pipes than that in straight pipes for the same

Reynolds number. The pitch of the helicoidal pipe also has an effect on the flow. As a result, the heat transfer rate becomes higher in helicoidal pipes relative to in straight pipes.

Unlike in straight pipes, the following dimensionless parameters are particularly useful in the case of helicoidal pipe: the Dean number (De); the Helical number (He), and the effective radius of curvature, R_c . These are defined as follows:

$$\text{De} = \text{Re} \left(\frac{a}{R} \right)^{1/2} \quad (4.19)$$

$$\text{He} = \text{Re} \left(\frac{a}{R_c} \right)^{1/2} = \text{De} \left[1 + \left(\frac{b}{2\pi R} \right)^2 \right]^{1/2} \quad (4.20)$$

$$R_c = R \left[1 + \left(\frac{b}{2\pi R} \right)^2 \right] \quad (4.21)$$

where a denotes the radius of a circular pipe, b represents the coil pitch, and R is the radius of the coil.

The critical Re_c , which is used to identify the transition from laminar to turbulent flow in curved or helicoidal pipes, has been recommended for design purposes by [111]

$$\text{Re}_c = 2100 \left[1 + 12 \left(\frac{R}{a} \right)^{-0.5} \right] \quad (4.22)$$

The fully developed Nusselt numbers for laminar flow in helicoidal pipes subjected to the uniform wall temperature have been obtained theoretically and experimentally by many researchers [89]. For helicoidal pipes with the thermal boundary condition, the Nu relation has been proposed by [112]

$$\text{Nu}_i = \left[\left(3.657 + \frac{4.343}{\left(1 + \frac{957}{\text{Pr De}^2} \right)^2} \right)^3 + 1.158 \left(\frac{\text{De}}{1 + \frac{0.477}{\text{Pr}}} \right)^{3/2} \right]^{1/3} \quad (4.23)$$

The flow inside the pipe shows a turbulent-like laminar behavior despite the fact that the Re is close to the critical value. The research conducted by [113] has indicated that turbulent flow entrance length in coils with circular cross sections is much shorter than that for laminar flow. Turbulent flow can become fully developed within the first half-turn of the coil. Therefore, most of the turbulent flow and heat transfer analyses concentrate on the fully developed region. The fully developed Nu relation for turbulent flow in helicoidal pipes subjected to the uniform wall temperature is recommended by [114]

$$\text{Nu}_s = 0.0225 \text{Re}^{0.8} \text{Pr}^{0.3} \quad (4.24)$$

$$\text{Nu}_o = \text{Nu}_s \left(1 + 3.54 \frac{a}{R} \right) \left(\frac{\text{Pr}_m}{\text{Pr}_w} \right)^{0.025} \quad \begin{array}{l} 5 < R/a < 84 \\ 1500 < \text{Re} < 2 \times 10^4 \end{array} \quad (4.25)$$

The convection heat transfer coefficient of the HTF within the coil is

$$h_i = \text{Nu}_i \frac{k_{HTF}}{D_{i,p}} \quad (4.26)$$

All fluid properties inside the pipe are evaluated at the bulk fluid temperature of $T_{bulk} = (T_{in} + T_{ex})/2$.

4.3.4 Cooking process of mixture (Latent heat gain)

4.3.4.1 Transition from subcooled boiling to saturated boiling

Boiling is classified as pool boiling or flow boiling, depending on the presence of bulk fluid motion. Boiling is called pool boiling in the absence of bulk fluid flow and

flow boiling (or forced convection boiling) in the presence of it. In our study, it is dealt with pool boiling rather than flow boiling. Four different boiling regimes are observed in pool boiling: natural convection, nucleate, transition, and film boiling as illustrated on the boiling curve in Figure 4.6, which is a plot of boiling heat flux versus the excess temperature. Although the boiling curve given in this figure is for water, the general shape of the boiling curve remains the same for different fluids. The specific shape of the curve depends on the fluid-heating surface material combination and the fluid pressure, but it is practically independent of the geometry of the heating surface.

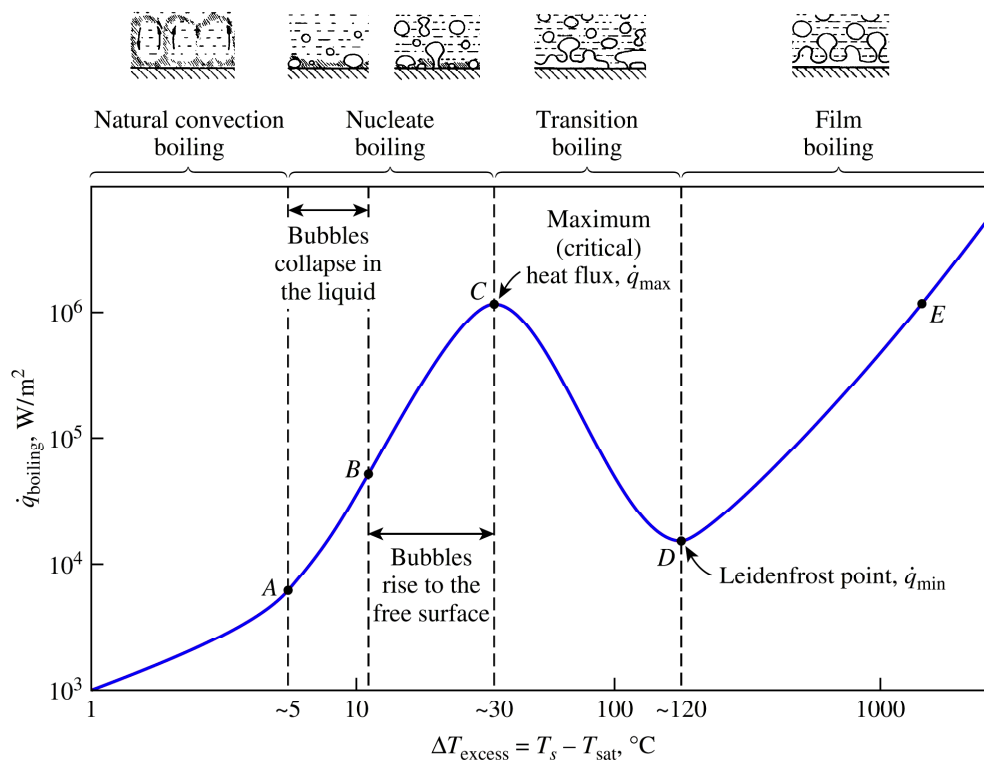


Figure 4.6. Typical boiling curve for water at 1 atm pressure [81].

In the regime of natural convection, the heat transfer takes place from the heater surface (only a few degrees above the saturation temperature i.e., towards point A) to the saturated liquid. The fluid motion in this mode of boiling is governed primarily by natural convection currents. If the temperature of the heating surface becomes higher than the saturation temperature, the regime is replaced from free convection to nucleate boiling. In the nucleate boiling regime, the bubbles start to form at various preferential sites on the heating surface. They are detached from the surface and dissipated in the liquid as obtaining high heat fluxes. The nucleation sites form at an

increasing rate so that the continuous columns of vapor columns appear as we move along the boiling curve from B to point C. As a result, very high heat fluxes are obtainable in this region. The nucleate boiling region ends and the unstable region (existence of partially both nucleate and film boiling) begins after the maximum (critical) is reached. As the heater temperature is increased past point C, the heat flux decreases as shown in Figure 4.6 since a large fraction of the heater surface is covered by a vapor layer which acts as an insulation due to its low thermal conductivity. Thus operation in the transition boiling regime is generally avoided in practice when high temperatures involved. Nucleate boiling at point C is completely replaced by film boiling at point D. Beyond point D, the heater surface is completely covered by a continuous stable vapor layer. The presence of the vapor layer is responsible for the low heat transfer rates in the film boiling region. The heat transfer rate increases with increasing excess temperature as a result of heat transfer from the heated surface to the liquid through the vapor film by radiation, which becomes significant at high temperatures.

Numerous experimental investigations have been reported, and various attempts have been made to correlate that portion of the boiling curve characterizing heat transfer in the nucleate boiling region [116]. It is evident from the results for nucleation behavior and from the discussion of parametric effects that the production of correlations for nucleate pool boiling heat transfer is fraught with difficulty [89]. However, the designer is faced with the necessity of calculating heat transfer coefficients for these systems and the use of correlations is inevitable, though the designer should be aware of the uncertainties involved. For any given situation, these correlations should be expected to give different predictions for the heat transfer coefficients; a good way of assessing the uncertainty is to calculate the coefficients using several of the correlations. One of the correlations proposed for nucleate pool boiling on horizontal tubes [116]:

$$\text{Nu}_o = AF'' \text{Re}_b^{2/3} \text{Pr}^{0.4} \quad (4.27)$$

where $A = 9.7P_c^{0.5}$. Here P_c in bar, and F'' is given by equation (4.27)

$$F'' = 1.8P_r^{0.17} + 4P_r^{1.2} + 10P_r^{10} \quad (4.28)$$

in which P_r is P_{sat}/P_c .

Under saturated pool boiling conditions, the boiling Re becomes

$$\text{Re}_b = \frac{\dot{q}_b D_{o,p}}{\mu_f h_{fg}} \quad (4.29)$$

Average variation of heat transfer coefficient on the tube is defined as

$$h_o = \text{Nu}_o \frac{k_w}{D_{o,p}} \quad (4.30)$$

4.3.4.2 Mass diffusion into wheat grains

The moisture content of wheat grains varies with time due to water diffusion until the wheat grains are not able to accept moisture uptake anymore. Absorbed water throughout cooking process can be estimated by summing up water absorbed by wheat grains throughout the preheating and boiling processes.

$$m_a = m_g \frac{[(W_p - W_0) - (W_b - W_p)]}{100} \quad (4.31)$$

4.3.4.3 Condensation heat transfer

Condensation takes place on the inner surfaces of the CP (cover and lateral wall) when the surface temperature falls below the dew point temperature of the evaporated water. Heat transfer rate in laminar film condensation on the underside of horizontal and inclined downward-facing surfaces are predicted by assuming the condensate flow to be the quasi-steady result of a bounded instability. This assumption makes it possible to determine the final shape of the liquid-vapor interface, and thus predict the average heat transfer coefficient. Gerstmann and

Griffith [117] studied film condensation on the underside of horizontal and inclined surfaces. At slight inclination angles ($\alpha < 7.5^\circ$), several flow regimes were observed, showing various wave patterns, and, at moderate inclination angles ($\alpha > 20^\circ$), roll waves appeared. The net effect of the roll waves increases and remains roughly constant up to an inclination of about 20° from the horizontal. However, the interfacial waves appear to be unchanged between angles of 20° and 90° .

For a horizontal surface, they developed the modified Ra as

$$\text{Ra} = \frac{g\rho_l(\rho_l - \rho_g)h_{fg}}{\mu_l\Delta Tk_l} \left(\frac{\sigma}{g(\rho_l - \rho_g)} \right)^{3/2} \quad (4.32)$$

The Nu relation for turbulent flow in helicoidal pipes subjected to the uniform wall temperature is recommended by

$$\text{Nu}_c = \begin{cases} 0.69\text{Ra}^{0.20} & 10^6 < \text{Ra} < 10^8 \\ 0.81\text{Ra}^{0.193} & 10^8 < \text{Ra} < 10^{10} \end{cases} \quad (4.33)$$

The average Nusselt number can be expressed as

$$\text{Nu}_c = \frac{h_c}{k_l} \left(\frac{\sigma}{g(\rho_l - \rho_g)} \right)^{1/2} \quad (4.34)$$

For slightly inclined surfaces i.e., $\alpha < 20^\circ$, Nu_c and Ra are modified from equations (4.32) and (4.34) by replacing g by $g \cos \alpha$ in each of the expressions.

The presence of air (non-condensable gas) in the CP hinders the condensation heat transfer. Minkowycz and Sparrow [118] investigated the effects of non-condensable gas, interfacial resistance, superheating, free convection due to both temperature and concentration gradients, mass diffusion and thermal diffusion, and variable properties in both the liquid and the gas-vapor regions on laminar film condensation. It was demonstrated that small bulk concentrations of the non-

condensable gas can have a decisive effect on the heat-transfer rate. Chin et al. [119] performed a numerical study for the influence of the air mass fraction (x_a) on the condensation rate on a vertical plate with respect to stagnant or moving steam–air mixtures, and compared their results with the experimental values obtained by Minkowycz and Sparrow [118]. Figure 4.7 shows the agreement between these two models. The ratio between the condensation rate of the mixture and pure steam, K_{air} depends mainly on x_a and slightly on the temperature difference between the gas and the wall. Variation in K_{air} obtained by [119] was proposed in order to predict the heat transfer coefficient by condensation as a function of x_a for various temperature ranges of $(T_\infty - T_w)$. Here T_∞ is the free stream temperature that is equal to the boiling temperature, and T_w is the wall temperature is estimated from the heat loss analysis of the CP.

The mass of condensed steam could then be obtained by

$$m_c = \frac{K_{air} h_c (T_b - T_w)}{h_{fg@T_b}} \quad (4.35)$$

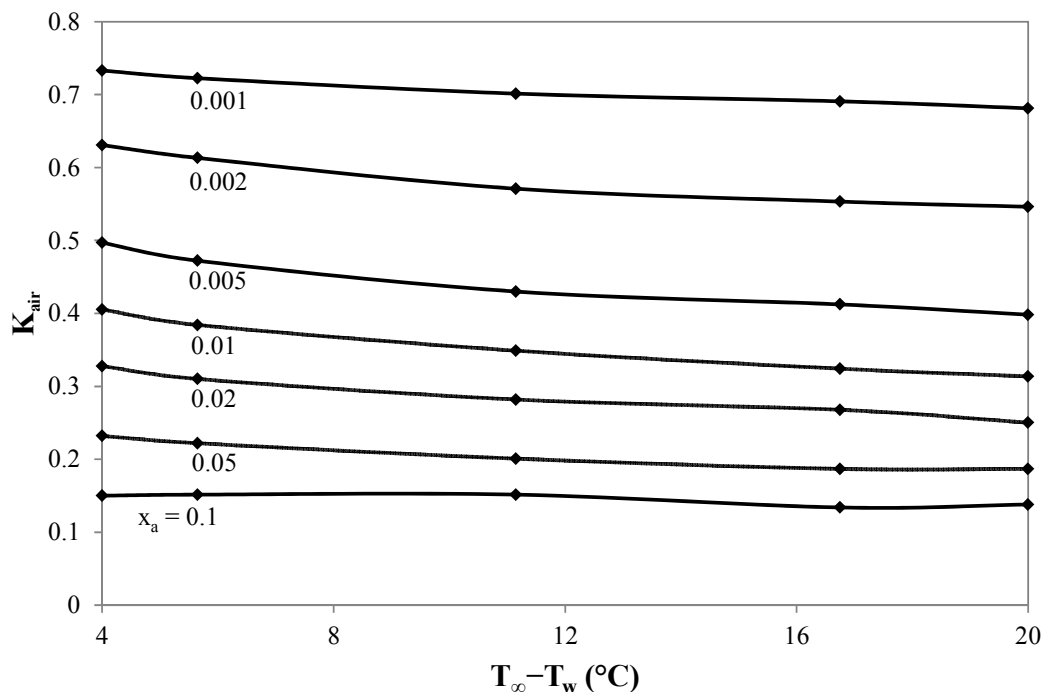


Figure 4.7. Condensation heat transfer in the presence of a non-condensable gas in quiescent mixture at $T_\infty = 100^\circ$. Adapted from [119].

4.3.5 Heat loss to surroundings

Heat loss from the outer surface of the CP (lateral sides and the cover) is estimated using the following relations:

For the lateral side in cylindrical shape, the average Nu relation for an isothermal vertical plate can be evaluated using the equation recommended by [99]:

$$\text{Nu}_{air} = \left[0.825 + \frac{0.387\text{Ra}^{1/6}}{\left[1 + (0.492/\text{Pr})^{9/16} \right]^{8/27}} \right]^2 \quad (4.36)$$

For the lateral side in conical shape, Ra is modified from equation (4.36) by replacing g by $g \cos \alpha$.

For the cover, the average Nu relation can be determined from the simple power-law relations proposed by [120] for horizontal surface facing upwards.

$$\text{Nu}_{air} = \begin{cases} 0.16\text{Ra}^{1/3} & 2 \times 10^8 < \text{Ra} \\ 0.13\text{Ra}^{1/3} & 5 \times 10^8 < \text{Ra} \end{cases} \quad (4.37)$$

Noting that all fluid properties are to be evaluated at the film temperature, $T_f = (T_{cp} + T_a)/2$.

In the analysis of heat loss from the CP, the thermal resistance approach is used for simplicity for heat flow from the boiling water to the ambient air into a single resistance $(UA)_{cp}$ as

$$\frac{1}{(UA)_{cp}} = \frac{1}{h_o A_{i,t}} + \frac{\ln(D_{o,t}/D_{i,t})}{2\pi L k_t} + \frac{\ln(D_{o,ins}/D_{i,ins})}{2\pi L k_{ins}} + \frac{1}{h_{air} A_{o,t}} \quad (4.38)$$

$$\dot{Q}_{loss} = (UA)_{cp} (T_b - T_a) \quad (4.39)$$

4.3.6 Mass transfer by flash evaporation

At the end of cooking process, the energy transfer to the mixture is finalized, and the cover of the CP is opened. Vaporization of the water takes place by flash boiling due to concentration difference between the saturated water and the ambient air. Some empirical formulas have been developed for the diffusion of water vapor in air. One of the popular was proposed by [121]:

$$D_{H_2O-air} = 1.87 \times 10^{-10} \frac{T^{2.072}}{P} \quad 280 \text{ K} < T < 450 \text{ K} \quad (4.40)$$

Utilizing the analogy between heat and mass convection, the mass transfer coefficient is determined by

$$h_{mass} = \frac{\text{Sh } D_{H_2O-air}}{L_c} \quad (4.41)$$

The Sherwood number and the mass transfer coefficients are determined for the case of horizontal surface to be

$$\text{Sh} = \begin{cases} 0.54(\text{Gr Sc})^{1/4} & 10^4 < \text{Gr Sc} < 10^7 \\ 0.15(\text{Gr Sc})^{1/3} & 10^7 < \text{Gr Sc} < 10^{11} \end{cases} \quad (4.42)$$

where $\text{Sc} = \nu / D_{H_2O-air}$ is the Schmidt number.

Then the evaporation rate and the rate of heat transfer by evaporation become

$$\dot{m}_f = h_f A_w (\rho_{v,s} - \rho_{v,\infty}) \quad (4.43)$$

4.3.7 Mass balance of water

During cooking operation, the total mass of water is conserved. That can be defined by the following equation as

$$m_T - \int_0^{\Delta t} \dot{m}_{ev} dt - \int_0^{\Delta t} (\dot{m}_b - \dot{m}_c) dt - \int_0^{\Delta t} \dot{m}_f dt - (m_r - m_l) - m_a = 0 \quad (4.44)$$

where m_T is the amount of water charged into the CP at the beginning of the cooking process. \dot{m}_{ev} is the total evaporated water during the preheating process of the water-wheat mixture. $\dot{m}_b - \dot{m}_c$ is the difference between the total amount of water boiled and condensed during the boiling process. \dot{m}_f is the total amount of water flashed during the resting time. $m_r - m_l$ is the difference between the amount of residual water, m_r , obtained at the end of cooking process and the leached substances, m_l , existing in the residual water. m_a is the amount of water absorbed by wheat grains during cooking operation.

4.3.8 Cooking load

The outlet temperature of the HTF is estimated by using energy balance and the heat transfer equations derived in the previous sections. In this estimation, radiation heat transfer among the lateral walls, food and the coiled pipe can be regarded negligible when compared to condensation since the surfaces have a low emissivity (stainless steel) and small temperature difference with their surroundings, and also the water vapor absorbs infrared radiation. Hence this mode of heat transfer is relatively little importance. Only the energy supplied to the CP is taken into account to launch nucleate boiling and to meet heat loss.

As a form of convection heat transfer, the boiling heat flux from a solid surface to the fluid is expressed from Newton's law of cooling as

$$\dot{q}_b = h_o \Delta T_{excess} \quad (4.45)$$

where $\Delta T_{excess} = T_s - T_{sat}$ is called the excess temperature, which represents the temperature excess of the surface above the saturation temperature of the fluid.

The energy transferred to the mixture under steady-state condition can be written in forms of different equalities:

$$\dot{Q}_{cp} = \dot{m}_{HTF} c_p (T_{in} - T_{ex}) = h_i A_s \Delta T_{lm} = \dot{q}_b A_s = \dot{m}_b h_{fg@T_b} \quad (4.46)$$

where $\Delta T_{lm} = \frac{\Delta T_1 - \Delta T_2}{\ln(\Delta T_1 / \Delta T_2)}$ and here $\Delta T_1 = T_{h,in} - T_s$, $\Delta T_2 = T_{h,out} - T_s$, respectively.

The exit temperature of the HTF is predicted by

$$T_{ex} = T_s + (T_s - T_{in}) e^{\frac{-h_i A_s}{(\dot{m} c_p)_{HTF}}} \quad (4.47)$$

The developed equations were integrated into EES Professional V8.581 and solved simultaneously regarding the algorithm given in Appendix F. The simulation results will be compared with the experimental results in Chapter 5.

4.4 Analysis of brazed plate heat exchanger

Heat exchangers are widely used devices for mainly heating, cooling and heat recovery processes in industrial applications from micro channel cooling to nuclear power plants. In recent years, there is an increase in the usage of gasketed plate heat exchangers (PHEs) especially in chemical industries such as brewery and food industry due to suitability in hygienic applications, ease of cleaning and thermal control. Furthermore, PHEs exhibit excellent heat transfer characteristics which allow more compact designs, and have flexibility in modifying its own size (or capacity) by simply mounting/dismounting the plates used. Over the past 30 years, it has become possible to manufacture brazed plate heat exchangers (BPHEs). These are manufactured by placing a copper or nickel foil in between each of the stainless steel plates and placing the pile of plates in a furnace just above the melting temperature of copper. The BPHE is in principle constructed as a package of corrugated channel plates between front and rear cover-plate packages shown in Figure 4.8. The cover-plate packages consist of sealing plates, blind rings and cover plates. Certain BPHEs are available with different types of channel plates where the

herringbone pattern varies. The benefit of different herringbone patterns is that the hydraulic and thermal characteristics of the BPHE can be modified.

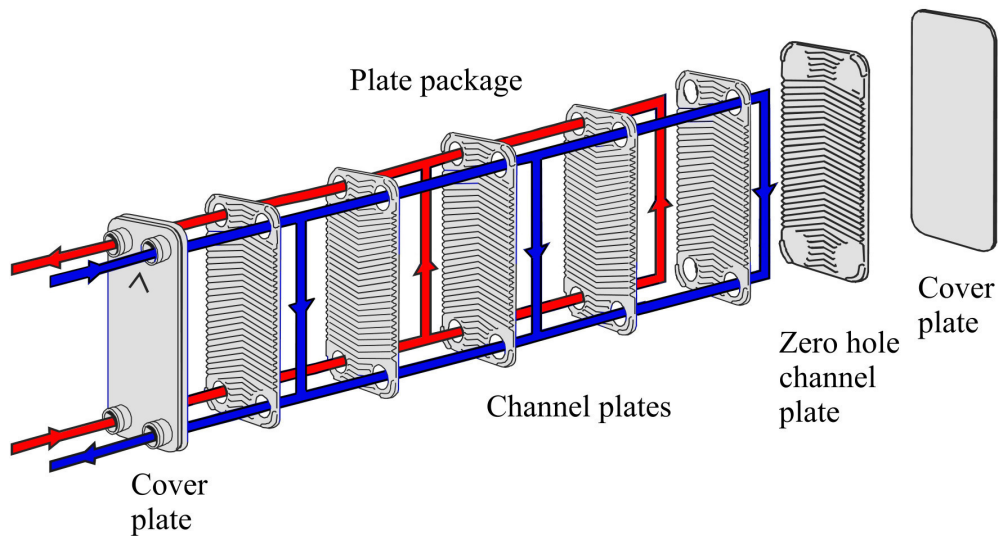


Figure 4.8. Exploded view of the BPHE. Adapted from [122].

4.4.1 Thermal analysis

The design of PHEs is highly specialized so that the variety of the designs available for the plates and arrangements must be selected for a specific purpose. Manufacturers have developed their own software programs for thermal design, selection and rating the PHEs that they market. Since most of the correlations developed for heat transfer and pressure drop cannot be generalized for every PHE to give a high degree of prediction [123]. The prediction method for analyzing the heat transfer relies on experimental data particular to a specific surface profile. Although some design methods have been reported in the literature [124], there is no a rigorous method to be applied to any PHE configuration. However, sizing of the PHE for a given duty can be predicted by the proposed correlations to suit preliminary calculations.

A wide variety of corrugation types and flow arrangements is available in practical applications for plate type heat exchangers. Although a number of commercial plates have a different surface profile, most modern PHEs are the chevron or herringbone type as shown in Figure 4.9. In the chevron type, one plate is

clamped with adjacent which is reversed 180° thus the corrugated pattern maintains numerous contact points between the plates in which the fluid flows. The effective heat transfer area of the PHE is enlarged by the corrugations. The increase in the surface area is expressed by the enlargement factor, ϕ which is defined as the ratio of the developed length to the projected or protracted length.

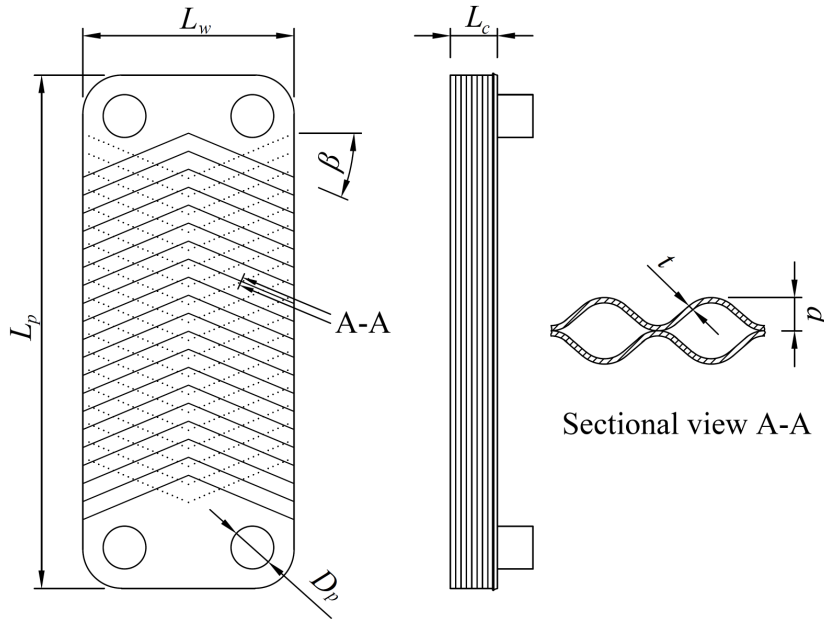


Figure 4.9. Schematic view of the plate.

The enlargement factor is expressed by the actual effective area specified by the manufacturer, A_1 to the projected plate area, A_{1p} :

$$\phi = \frac{A_1}{A_{1p}} \quad (4.48)$$

A_1 and A_{1p} can be estimated by using the relations below. For the thermal analysis, the constructional data of the proposed BPHE for the duty taken from the product catalogue of SWEP (B10TH model) are provided by the manufacturer [122] as given in Table 4.3.

$$A_1 = \frac{A_e}{N_e} \quad (4.49)$$

$$A_{1p} = L_p L_w \quad (4.50)$$

Table 4.3. Technical specifications of the BPHE [122].

Plate material	AISI 316
Effective flow plate distance, L_p	0.243 m
Effective channel width, L_w	0.119 m
Port diameter, D_p	0.024 m
Plate thickness, t	0.0004 m
Corrugation depth, b	0.00224 m
Total effective area, A_e	0.248 m ²
Enlargement factor, ϕ	1.19
Chevron angle, β	23°
Number of plates, N_t	10
Effective number of plates in heat transfer, N_e	8
Number of channels on (hot side/cold side)	4/5
Thermal conductivity of the plate, k_w	15.5 W/m°C

The cross-section of a corrugation surface being very complex, flow between two adjacent plates is defined by the mean channel spacing, b shown in Figure 4.9.

$$b = p - t \quad (4.51)$$

where p is the plate pitch, and t is the plate thickness.

4.4.2 Effectiveness-NTU method

When the inlet or outlet temperatures of the fluid streams are not known, the method of the NTU based on the concept of heat exchanger effectiveness may be used to avoid a trial-and-error procedure. When the type and size of the heat exchanger are specified, the determination of the heat transfer rate and the outlet temperatures of the hot and cold fluids for prescribed fluid mass flow rates and inlet temperatures can be estimated using this method. The heat transfer surface area of the heat exchanger in this case is known, but the outlet temperatures are not. Here the task is to determine the heat transfer performance of a specified heat exchanger. However, in transient system analysis, the heat transfer rate, and the outlet

temperatures of the hot and cold fluids will change instantly thus it is necessary to make iteration to estimate them.

The method is based on a dimensionless parameter called the heat transfer effectiveness ε , defined as

$$\varepsilon = \frac{\dot{Q}}{\dot{Q}_{\max}} \quad (4.52)$$

which is the ratio of actual heat transfer rate in a heat exchanger to the thermodynamically limited maximum possible heat transfer rate if an infinite heat transfer surface area were available in a counter flow heat exchanger.

The maximum possible heat transfer rate in a heat exchanger is

$$\dot{Q}_{\max} = C_{\min} (T_{h,in} - T_{c,in}) \quad (4.53)$$

where C_{\min} is the smaller of $C_h = \dot{m}_h c_{p,h}$ and $C_c = \dot{m}_c c_{p,c}$.

The effectiveness of a heat exchanger depends on the geometry of the heat exchanger as well as the flow arrangement. For counter-flow, ε is expressed as [125]

$$\varepsilon = \frac{\exp[(1-c)NTU]-1}{\exp[(1-c)NTU]-c} \quad (4.54)$$

where c and NTU are the dimensionless quantities called as the capacity ratio, the number of transfer units, respectively.

$$c = \frac{C_{\min}}{C_{\max}} \quad (4.55)$$

$$NTU = \frac{UA_e}{C_{\min}} \quad (4.56)$$

The overall heat transfer coefficient, U is estimated by using the procedure proposed below:

The flow regime between the plates is characterized by Re which is expressed based on channel mass velocity and the hydraulic diameter of the channel.

$$Re = \frac{G_c D_h}{\mu} \quad (4.57)$$

The hydraulic diameter of the channel is defined as

$$D_h = \frac{4 \times \text{channel flow area}}{\text{wetted surface}} = \frac{4A_c}{P_w} = \frac{4bL_w}{2(b + L_w\phi)} \quad (4.58)$$

The channel mass velocity is given by

$$G_c = \frac{\dot{m}}{N_{cp} A_c} \quad (4.59)$$

N_{cp} is the number of channels per pass and is obtained from

$$N_{cp} = \frac{N_t - 1}{2N_p} \quad (4.60)$$

where N_t is the total number of plates, and N_p is the number of passes. The term “pass” in PHE refers to a group of channels in which the flow is in the same direction. Figure 4.8 demonstrates also the flow arrangement of the BPHE (single pass U-type) employed in the experimental setup.

The conventional approach for estimation of the convection heat transfer coefficient between flow passages is employed by some specific correlations that are used for taking into account the effects of the different geometric parameters of the corrugated profiles. Despite the fact that generalized correlations for heat transfer

and pressure drop predictions are not quite well developed, there are still open questions concerning the choice of the most appropriate models. However a few researches are proposed for more elaborate calculations [126,127].

Wanniarachchi et al. [128] proposed the following Nusselt number correlation for herringbone plates in the range of $1 \leq \text{Re} \leq 10^4$, $20^\circ \leq \beta \leq 62^\circ$.

$$\text{Nu} = [\text{Nu}_l^3 + \text{Nu}_t^3]^{1/3} \text{Pr}^{1/3} \left(\frac{\mu}{\mu_w} \right)^{0.17} \quad (4.61)$$

$$\text{Nu}_l = 3.65 \beta^{-0.455} \phi^{0.661} \text{Re}^{0.339} \quad (4.62)$$

$$\text{Nu}_t = 12.6 \beta^{-1.142} \phi^{1-m} \text{Re}^m \quad (4.63)$$

where $m = 0.646 + 0.0011\beta$

The convection heat transfer coefficient, h can be obtained by using equation (4.64) as

$$h = \text{Nu} \frac{k}{D_h} \quad (4.64)$$

The overall heat transfer coefficient for a clean surface is

$$\frac{1}{U} = \frac{1}{h_h} + \frac{1}{h_c} + \frac{t}{k_w} \quad (4.65)$$

where h and c stand for hot and cold streams respectively.

The thermophysical properties of the fluid used in the BPHE are given as a function of temperature in Appendix A. The fluid properties are evaluated at bulk

temperatures at the cold side, hot side and the wall of the BPHE. $T_{bulk} = (T_{in} + T_{out})/2$ will be arranged for hot, cold and wall temperatures.

Finally, the outlet temperatures of the hot and the cold fluid streams are determined to be

$$T_{h,out} = T_{h,in} - \frac{\dot{Q}}{C_h} \quad (4.66)$$

$$T_{c,out} = T_{c,in} + \frac{\dot{Q}}{C_c} \quad (4.67)$$

The developed equations were written in EES Professional V8.581 using its macro tool and solved simultaneously according to the algorithm given in Appendix F. Model validation of the simulation results will be checked in Chapter 5 by employing the experimental data.

4.5 Analysis of thermal expansion tank

TET provides space for the HTF due to volume change when heated from ambient temperature to normal operating temperature. It is usually installed at highest point in the solar field before the suction of the pump to provide positive pressure head, and also to vent moisture, non-condensables and any low boiling components. The TET should be sized to hold about a 25 percent level when the fluid is cold and have no more than a 75 percent level when the system is at its maximum operating temperature. [129]. Using these guidelines will usually result in the TET size to hold about 30 to 50 percent of the total system fluid volume. The TETs are usually blanketed with nitrogen to maintain a non-reactive atmosphere and keeping a positive pressure which prevents air and moisture from entering the tank. If a non-reactive gas is not used, the HTF is oxidized at elevated temperatures and the chemical stability of the HTF is deteriorated with time. Otherwise, the tank temperature should be kept under 60°C, and also the contact surface of the HTF with atmospheric moisture should be reduced to minimize oxidation.

4.5.1 Volume expansion

The density of a fluid, in general, depends more strongly on temperature than it does on pressure. Thermal oils do not usually undergo high pressure differences due to having low saturated pressure at high temperatures, i.e., the vapor pressure at 300°C corresponds to about 1 bar. Thus, it is quantified the variation of the density of the fluid with temperature at constant pressure with *coefficient of volume expansion* β , which is defined as

$$\beta = -\frac{1}{\rho} \left(\frac{\partial \rho}{\partial T} \right) \approx -\frac{\Delta \rho / \rho}{\Delta T} \quad (4.68)$$

The total HTF volume to be confined initially into the piping work and the TET is defined by the following equation,

$$V_{HTF} = V_c + V_h + 0.25V_{ex} + V_{PTSC} \quad (4.69)$$

where

$$V_c = \frac{\pi}{4} \sum_i D_i^2 L_i \quad (4.70)$$

$$V_h = \frac{\pi}{4} \sum_j D_j^2 L_j \quad (4.71)$$

$$V_{PTSC} = \frac{\pi}{4} n_a D_{ia}^2 L_a \quad (4.72)$$

The HTF level in the TET is predicted by differentiating the total volume as a function of time

$$A_s \frac{dH}{dt} = V_{HTF} [\beta(T) - \beta_0] \quad (4.73)$$

4.5.2 Heat loss analysis

Heat loss from the tank to the surrounding air is significant for energy analysis of the system. The procedure for heat losses in the TET was taken from the methodology developed by Kumana and Kothari [130]. The assumptions made for the heat loss calculation in the TET are

- Radiation losses are negligible if the tank is insulated.
- Temperature distribution within the gas and liquid regions are uniform.
- Thermal equilibrium exists between the gas and the liquid fluid.

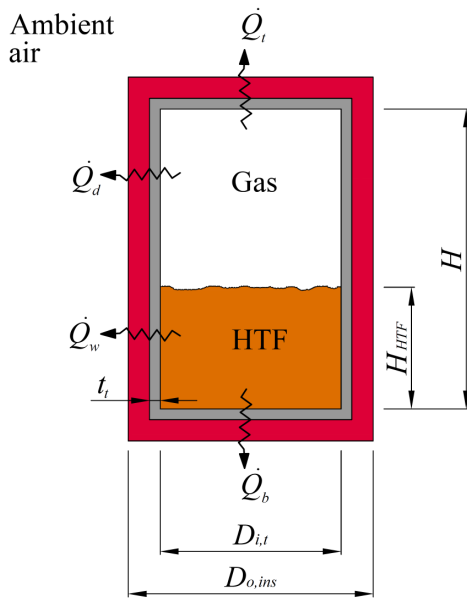


Figure 4.10. Thermal losses from TET in vertical position.

As shown in Figure 4.10, the four individual losses in the tank need to be calculated. The heat loss from each surface is shown below.

For wet sidewall:

$$\frac{1}{(UA_s)_w} = \frac{1}{h_{HTF} A_i} + \frac{\ln(D_{o,t}/D_{i,t})}{2\pi L_w k_t} + \frac{\ln(D_{o,ins}/D_{i,ins})}{2\pi L_w k_{ins}} + \frac{1}{h_\infty A_o} \quad (4.74)$$

$$\text{where } A_i = \pi D_{i,t} H_{HTF} \text{ and } A_o = \pi D_{o,ins} H_{HTF} \quad (4.75)$$

$$\dot{Q}_w = (UA_s)_w (T_{HTF} - T_\infty) \quad (4.76)$$

For bottom side:

$$\frac{1}{(UA_s)_b} = \frac{1}{h_{HTF} A_i} + \frac{t_t}{k_t A_i} + \frac{t_{ins}}{k_{ins} A_o} + \frac{1}{h_\infty A_o} \quad (4.77)$$

$$\text{where } A_i = \pi D_{i,t}^2 / 4 \text{ and } A_o = \pi D_{o,ins}^2 / 4 \quad (4.78)$$

$$\dot{Q}_b = (UA_s)_b (T_{HTF} - T_\infty) \quad (4.79)$$

For dry sidewall:

$$\frac{1}{(UA_s)_g} = \frac{1}{h_g A_i} + \frac{\ln(D_{o,t}/D_{i,t})}{2\pi L k_t} + \frac{\ln(D_{o,ins}/D_{i,ins})}{2\pi L k_{ins}} + \frac{1}{h_\infty A_o} \quad (4.80)$$

$$\text{where } A_i = \pi D_{i,t} (H - H_{HTF}) \text{ and } A_o = \pi D_{o,ins} (H - H_{HTF}) \quad (4.81)$$

$$\dot{Q}_g = (UA_s)_g (T_g - T_\infty) \quad (4.82)$$

For top side:

$$\frac{1}{(UA_s)_t} = \frac{1}{h_g A_i} + \frac{t_t}{k_t A_i} + \frac{t_{ins}}{k_{ins} A_o} + \frac{1}{h_\infty A_o} \quad (4.83)$$

$$\text{where } A_i = \pi D_{i,t}^2 / 4 \text{ and } A_o = \pi D_{o,ins}^2 / 4 \quad (4.84)$$

$$\dot{Q}_t = (UA_s)_t (T_g - T_\infty) \quad (4.85)$$

Therefore, the total heat losses from the TET can be estimated by

$$\dot{Q}_{ex} = \dot{Q}_w + \dot{Q}_b + \dot{Q}_g + \dot{Q}_t \quad (4.86)$$

The convection heat transfer coefficients can be estimated using the proposed correlations below for different cases: external and internal convection for cylinder and vertical or horizontal surfaces.

Wind case: Cross flow over cylinder

The average Nu for external forced convection over cylinder in cross flow is proposed by [131].

$$\text{Nu}_D = \frac{h_\infty D_{oc}}{k_\infty} = C \text{Re}_D^m \text{Pr}^{0.37} \left(\frac{\text{Pr}}{\text{Pr}_w} \right)^{0.25} \quad (4.87)$$

Table 4.4. Constants for equation (4.87).

Re	<i>c</i>	<i>m</i>
1–40	0.76	0.4
40–1×10 ³	0.52	0.5
1×10 ³ –2×10 ⁵	0.26	0.6
2×10 ⁵ –1×10 ⁷	0.023	0.8

Fluid properties are evaluated at the average temperature of $T_f = (T_s + T_\infty)/2$, except Pr_w which is evaluated at the wall temperature.

At low Re, heat transfer of a circular cylinder is influenced by natural convection. At high values of Re, the effect of natural convection is negligible as compared to that of forced convection. For $\text{Re} \leq 1$, the heat transfer in flows of gases can be estimated using the correlation recommended by [132].

$$\text{Nu} = 0.35 + 0.5 \text{Re}^{0.5} + 0.001 \text{Re} \quad (4.88)$$

which holds for air and diatomic gases.

No wind case: Natural currents over cylinder

Vertical cylinder can be approximated as vertical plate when $D_{o,ins} \geq 35H/Gr_H^{1/4}$.

The average Nu relation for an isothermal vertical plate can be evaluated using the equation recommended by [99]

$$Nu_p = \left[0.825 + \frac{0.387Ra_L^{1/6}}{\left[1 + (0.492/Pr)^{9/16} \right]^{8/27}} \right]^2 \quad (4.89)$$

For horizontal plate:

The relations of Nu for the horizontal plate facing downwards and upwards are proposed by [120], respectively.

$$Nu = 0.58Ra^{1/5} \quad 10^6 < Ra < 10^{11} \quad (4.90)$$

$$Nu = \begin{cases} 0.16Ra^{1/3} & Ra < 2 \times 10^8 \\ 0.13Ra^{1/3} & 5 \times 10^8 < Ra \end{cases} \quad (4.91)$$

For windy condition, the convection heat transfer coefficient can be calculated by using the wind enhancement factor proposed by [130]

$$h_{\infty,wind} = \zeta_w h_{\infty,no\ wind} \quad (4.92)$$

For vertical plate:

$$Nu = 0.56Ra^{1/4} \quad 10^5 < Ra < 10^{11} \quad (4.93)$$

For windy condition, the convection heat transfer coefficient is

$$h_{\infty,wind} = \zeta_w h_{\infty,no\ wind} \quad (4.94)$$

The solution algorithm for analyzing the TET was written in EES Professional V8.581 using its macro tool, and solved simultaneously according to the algorithm given in Appendix F.

4.6 Analysis of pipe field

Thermal losses take place in the solar field piping owing to the temperature difference between the HTF and the surrounding air. The way to mitigate the thermal losses is by adding insulation to the pipes, but adding too much insulation generates excessive cost with little extra benefits. Glass wool [133], whose physical properties are given in Appendix E, is used as insulation material in the pipe installations.

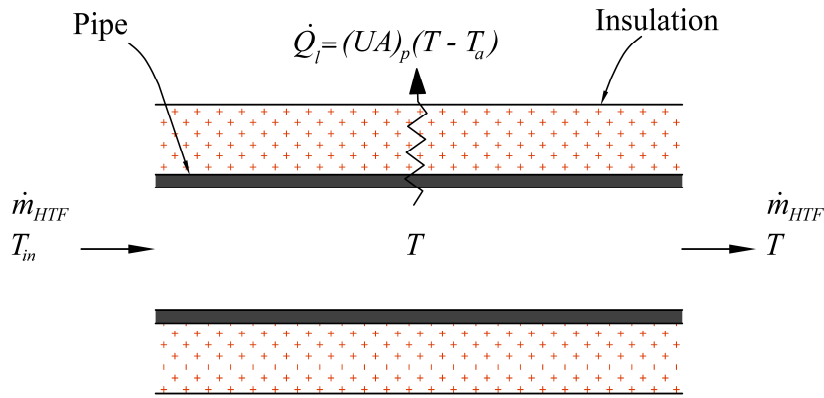


Figure 4.11. Thermal inertia analysis of pipe header.

The transient analysis is employed to the pipe header (see Figure 4.11) applying the energy balance. As a result an ordinary differential equation is obtained as

$$(mc_p)_T \frac{dT}{dt} = \dot{m}_{HTF} c_{p,HTF} (T_{in} - T) - (UA)_p (T - T_a) \quad (4.95)$$

$$\text{where } (mc_p)_T = (mc_p)_{HTF} + (mc_p)_p + (mc_p)_{ins} \quad (4.96)$$

Integrating equation (4.95)

$$\int_0^{t+\Delta t} \frac{dT}{T - T_p} = - \frac{\dot{m}_{HTF} c_{p,HTF} + (UA)_p}{m_{HTF} c_{p,T}} \int_0^{t+\Delta t} dt \quad (4.97)$$

where

$$T_p = \frac{\dot{m}_{HTF} c_{p,HTF} T_{in} + (UA)_p T_a}{\dot{m}_{HTF} c_{p,HTF} + (UA)_p} \quad (4.98)$$

The time dependent temperature variation is obtained as

$$T(t + \Delta t) = T_p + (T(t) - T_p) e^{-\frac{\dot{m}_{HTF} c_{p,HTF} + (UA)_p \Delta t}{m_T c_{p,T}}} \quad (4.99)$$

4.7 Analysis of solar field

A steady-state trough receiver model determines the temperature rise across the node with an energy balance between the absorbed energy, the mass flow rate of HTF through the receiver, and the specific heat of the HTF. However, a steady-state model is insufficient once the thermal inertia associated with the energy state becomes significant. This is the case for parabolic troughs so transient terms must be included.

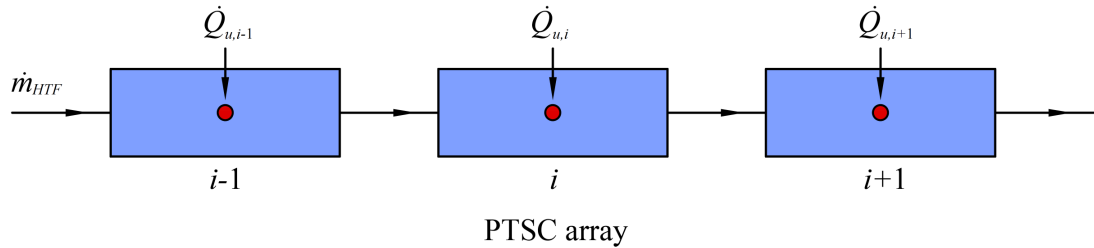


Figure 4.12. Nodal analysis of PTSC array.

Although it is commonly assumed that a solar process heat operates under steady state condition, this assumption is not true for most of the operation time. In this case, a transient analysis is necessary to incorporate the thermal inertia of the system. A physical model called as *nodal approach* is applied to the PTSC field shown in Figure 4.12 since it is well matching with the annual performance of the SAM empirical model which has been previously verified with plant data [134]. If the energy balance is written for transient conditions:

$$(mc_p)_{HTF} \frac{dT}{dt} = \dot{m}_{HTF} c_{p,HTF} (T_{in} - T) + \dot{Q}_u \quad (4.100)$$

which is a first order linear differential equation thus can be solved by the straightforward integration as

$$\int_0^{t+\Delta t} \frac{dT}{T - T_{in} - \dot{Q}_u / \dot{m}_{HTF} c_{p,HTF}} = -\frac{\dot{m}_{HTF}}{m_{HTF}} \int_0^{t+\Delta t} dt \quad (4.101)$$

$$T(t + \Delta t) = T_{in} + \frac{\dot{Q}_u}{\dot{m}_{HTF} c_{p,HTF}} + \left(T(t) - T_{in} - \frac{\dot{Q}_u}{\dot{m}_{HTF} c_{p,HTF}} \right) e^{-\frac{\dot{m}_{HTF}}{\rho_{HTF} V_a} \Delta t} \quad (4.102)$$

Using a nodal notation, the last expression can be rewritten as

$$T_i^+ = T_{i-1} + \frac{\dot{Q}_{u,i}}{\dot{m}_{HTF} c_{p,HTF,i}} + \left(T_i - T_{i-1} - \frac{\dot{Q}_{u,i}}{\dot{m}_{HTF} c_{p,HTF,i}} \right) e^{-\frac{\dot{m}_{HTF}}{\rho_{HTF,i} V_a} \Delta t} \quad (4.103)$$

where T_i^+ is the temperature at node i in the next time step.

4.8 Summary

Thermal models for system components (WPT, CP, BPHE and TET) have been performed to use them in the transient system simulation of the SAPH system after model validation. Physical insight of cooking process was described, and a mathematical model for designing IHHE type CP was performed. In addition, a thermal analysis for BPHE is proposed to determine its size under the prescribed thermal load and inlet temperatures. On the other hand, design considerations for TET were introduced for thermal system design. Finally, pipe headers and receiver tube of PTSC were analyzed in terms of thermal inertia concept for unsteady operations.

CHAPTER 5

EXPERIMENTAL STUDY ON SOLAR ASSISTED COOKING SYSTEM

5.1 Introduction

Process heat applications are utilized in a wide range of industrial sectors. In industrial bulgur plants, process heat is employed for cooking and drying processes which require remarkable quantity of thermal energy; normally it is met from fossil fuels or its derivatives. Cooking process is generally carried out by single-stage cooking system in conventional plants. Each cooking process is operated in 2–3 hours time periods in these plants. The daily bulgur production capacity for them is about 60 tones. In the single-stage, preheating and cooking processes are performed in the same boiler. The boiling loss generated during cooking is continuously exhausted to the surrounding. Unlike conventional plants, latest modern plants are operated with a daily capacity of 140 tones by using double-stage cooking system. The double-stage cooking system is formed of two boilers. The boiler in the first stage preheats the water-wheat mixture to a preset temperature (lower than boiling temperature). After this process, the mixture is discharged into the double-stage which cooks the wheat grains until the gelatinization of the starch in grains' structure is maintained. At the end of the cooking process, the steam formed is expelled to surrounding from the boiler by a vacuum system as waste heat. Thermal energy demand of industrial bulgur plants for cooking facility is supplied by conventional heating systems. The plants having automation and process control are operated daily under continuous batch production. Thus, the heating systems of these plants are generally operated at certain temperature levels and specified loads.

It is fundamental to analyze the industrial sector and the integration capability of the solar heat to the process being applied before carrying out a SAPH application.

Since solar heat integration into a process heat application brings certain technical issues and drawbacks. There are many challenges which must be overcome to make a SAPH application feasible because solar energy shows a tendency of intermittent and variable character throughout a day. In contrast, most of the thermal systems operate under steady conditions thus need a reliable energy supply. Nevertheless, solar systems have been adapted and coupled with many thermal systems for different process applications [12]. These types of applications require a detailed thermal analysis and/or an experimental study for technical feasibility. Another issue in solar thermal system for industrial applications is the optimal sizing of the system components i.e., appropriate sizing of the collectors, storage and heat exchanger. Different guidelines and methodologies [5,40–43] are available in the literature related to the design stages of SHIP systems. For systems operating above 100°C, detailed simulation programs such as TRNSYS, SOLTES or SOLIPH are generally used. Furthermore, the studies presented in the literature [6–39] on the medium temperature SHIP applications may guide the users through the preliminary analysis of the systems being designed.

In this chapter, the experimental setup installed for the designed SAPH system was presented, and the test results obtained from the experimental studies were analyzed. Additionally, performance parameters of the SAPH system were analyzed operating the system under different operating conditions. Model validations for the CP (IHHE type) and BPHE were performed by comparing with the experimental results. Moreover, three different CPs for boiling wheat were designed and their performance tests were accomplished.

5.2 System description

5.2.1 Experimental setup of SAPH application

The schematic diagram of the experimental setup for testing the SAPH system is shown in Figure 5.1. The system is composed of two closed loops (primary and secondary) which are connected to each other by means of a BPHE. The primary loop (PL) basically consists of auxiliary heater, CP, WPTs and TET. And the secondary loop (SL) includes PTSC array, CHE and TET.

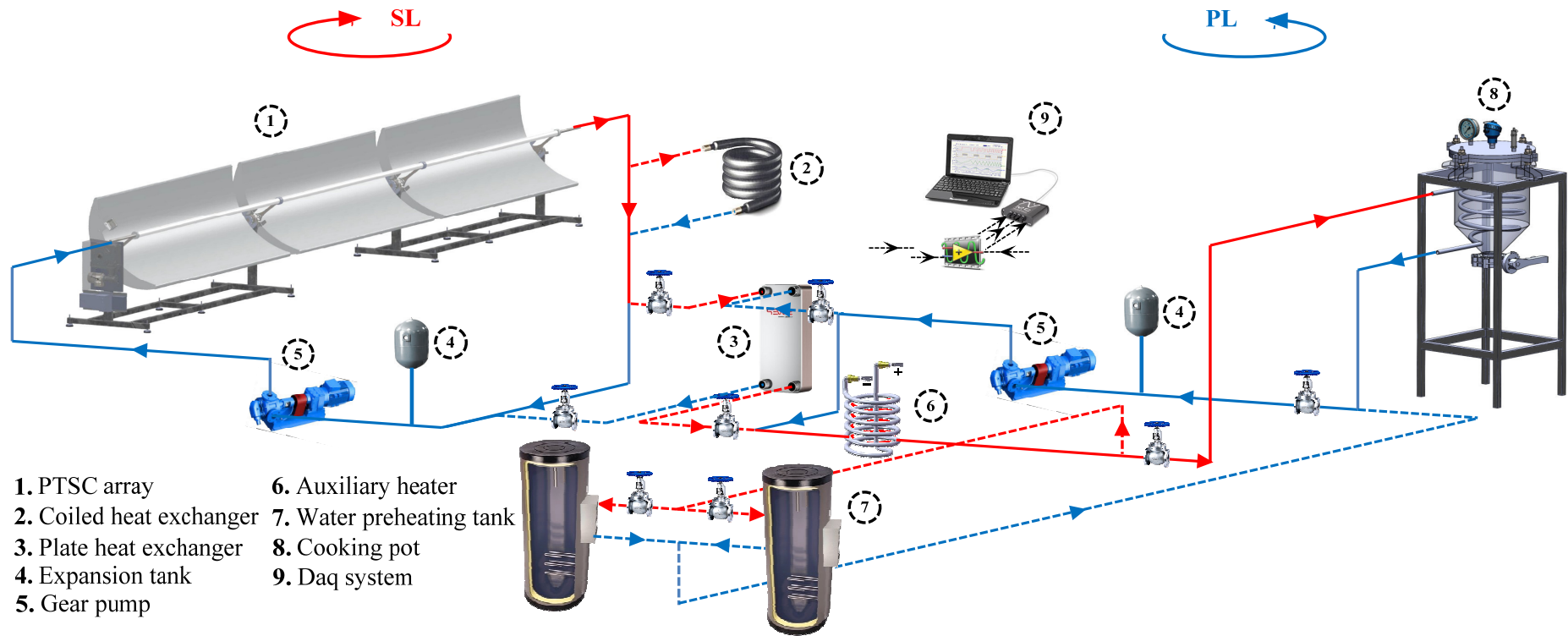


Figure 5.1. Experimental layout of the SAPH application.

The PTSC array is composed of three collectors connected in series as seen from the experimental test setup installed on campus of Gaziantep University (see Figure 5.2). The orientation of the PTSC array is designated as the north-south axis tracking. The tracking system is driven by the frequency-controlled double worm gear motor which is manipulated by the cooperation of the central control unit. The tracking motion is controlled by both fine positioning sun-seeking detector and external GPS (Global Positioning System).



Figure 5.2. Test setup of the SAPH application.

The working fluid used in both loops was selected Renolin therm 320 as HTF (see Appendix A) to easily control the process-temperature, and run the loops at lower operating pressures. The thermal energy transfer from the SL to the PL is realized directly by the BPHE to facilitate the transfer of heat at higher efficiency with a minimal loss. The BPHE was selected from the product catalogue of SWEP whose technical specifications are given in Table 4.1. The HTF is circulated in both loops by means of frequency-controlled gear pumps [135] which are used to adjust the flowrate. The auxiliary heater is a type of special design of CHE enclosed by an electric heater. It is used in stead of a conventional heating system to supply auxiliary thermal power to the HTF circulated within the PL. Furthermore, its use will provide

increasing degree of reliability for the desired application to meet a particular load without TES. The capacity of the electric heater is 6 kW which is controlled by a PID (Proportional Integral Derivative) controller. When the operating temperature of the loop falls below the load-temperature, the auxiliary heater is activated to increase the return-temperature of the HTF to the load-temperature meeting the thermal load.

The WPT is used for the task of water preheating. When the water inside the WPT reaches the pre-heat temperature of 90°C, the preheated water is discharged into the CP. The temperature of the preheated water falls down since it is mixed with wheat grains (initially at about ambient temperature) in the CP. After discharging process, the valves of the water tanks are closed and the CP' is opened to transfer energy only to the mixture until the cooking temperature reaches the boiling temperature, i.e. 100°C. The CP is sealed well by a gasket, and the temperature inside the CP is controlled by a pressure relief valve that keeps the pressure at the corresponding boiling temperature by periodically allowing some steam to escape, thus preventing any excess pressure buildup. When the boiling begins, energy requirement for cooking is reduced. At this stage, the supplied energy is decreased only to be able to keep the cooking temperature at the inner part of the mixture constant. The total mass flowrate is lowered for only supplying energy to the CP.

5.2.2 Measurement devices

The temperature measurements in the experimental setup are performed by the resistance temperature detectors (Pt100, Class A) connected with two leads. The temperature dependent uncertainty of the detectors are designated by the relation of $\pm(0.15 + 0.002T)^{\circ}\text{C}$ and calibrated according to the standard of IEC751 [136]. The pressure measurements are realized analogously by pressure gauges [137]. The flowmeters are selected as coriolis and ultrasonic types to measure the mass flowrate of the heat transfer fluid (HTF) in the PL and SL. The ultrasonic type flow meter has an accuracy of $\pm 1.0\%$ with a repeatability of less than 0.2% [138], and the coriolis has an accuracy of $\pm 0.1\%$ with a repeatability of less than 0.05% [139]. The irradiance sensor is used to measure the global radiation by a high sensitive Kipp & Zonen CMP11 pyranometer with an expected uncertainty of less than 2% as daily total [140]. The diffuse radiation measuring is executed with a shading ball

obstructing the direct beam falling onto the pyranometer. Thus the direct beam radiation is accurately determined using the relation [72]:

$$I = I_d + I_b \cos \theta_z \quad (5.1)$$

where θ_z is the zenith angle of the sun defined as the angle between the line of beam radiation and horizontal surface.

During experimental tests, data on temperature, flow, and solar radiation were gathered by the Daq (data acquisition) devices for further analyses. For this task, 24-bit USB-2416 and USB-TEMP measurement computing Daq devices were selected in order to obtain highly-accurate voltage and temperature measurements, respectively [141,142]. Daq devices are easily connected to the computer and managed by an interface software program called as TracerDAQ Pro that is used to acquire data from the Daq devices for virtual graphing and data logging. For the measurement sensors giving output signal as current (like 4–20 mA), the signals were converted to voltage output by using configurable signal converter [143] to be suited with the signal input of USB-2416.

5.2.3 System arrangement

Various possible configurations of solar plants that assist industrial heating process are presented in [42]. Selecting a suitable configuration or configuring a new concept may provide to obtain relatively much higher solar fraction if it matches with the operating conditions of the IPH application [18]. TES is employed to solar systems primarily for recovering energy to use in non-solar periods. It maintains to eliminate short term fluctuations, and shifts the energy that is stored during periods of high solar availability to use in the early morning and/or at night when the solar gain declines or diminishes in daily system operation. However, using TES imposes some major complications [144]. One of the complications is that the primary collecting system must be sufficiently large to build the supply of stored energy during periods of adequate solar radiation. Thus, additional collecting area (and its additional capital cost) is needed in this condition. The second complication requires

that TES system must be large enough to permit the system to operate over periods of inadequate sunshine. The alternative is to have a backup energy supply, which adds a capital cost and provides a unit that remains idle. In the short run, solar energy can and probably needs to be integrated into systems that also use conventional energy sources, such as fossil fuels. In the long run, however, stand-alone solar energy systems may be desired.

In our system arrangement, the direct integration of the solar field is preferred, and the TES is not used. The electric heater is used in the PL instead of conventional heating system, thus the process thermal load will be assisted by additional heating when the solar fraction is not adequate. The HTF circulating in the loop is initially heated by the electric heater to bring the operating or load-temperature to the preset value. The HTF in the SL is circulated in the solar field until the outlet temperature of the PTSC array exceeds the load-temperature defined for the PL. Later, the flow is directed toward the BPHE by opening the bypass valves of both loops to initiate assisting the PL with solar energy. The electric heater additionally serves as auxiliary heater after solar assisting starts. This process continues until the temperature of the HTF circulating within the SL falls below the return-temperature. At this condition, the bypass valves are shut down, and the HTF within the solar field is re-circulated through the loop. It is intended to collect energy while having passed the hot HTF through the CHE in order to preheat the process-water for later usage. The next solar field operation is managed repeatedly for the following day as mentioned above.

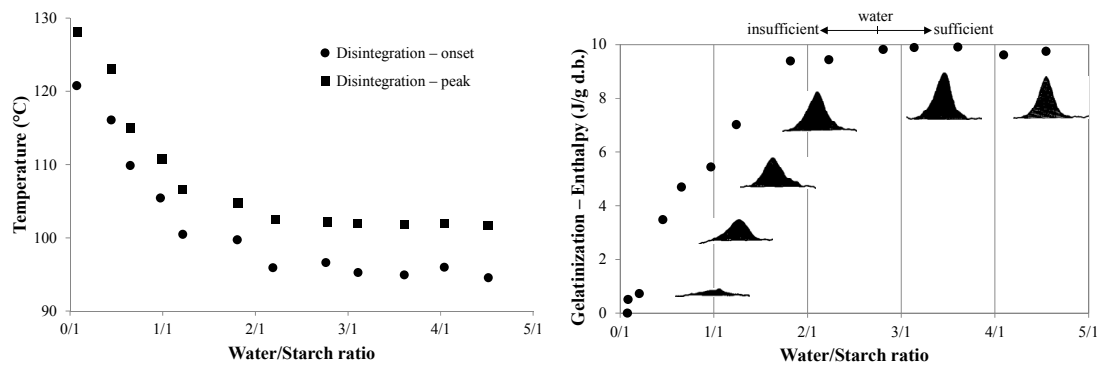
5.3 Methodology

The described system was monitored in different days to be operated. In this section, the test conducted in August 29, 2013 is presented in detail. Furthermore, the performance parameters for the analysis of the SAPH application are introduced. Moreover, the tests belonging to two different days are presented in Section 5.5.

5.3.1 Preparation of materials

For cooking facility, mainly a sample to water ratio of 1:2 (wheat:water) was used to satisfy a high degree of starch gelatinization in wheat grains [145]. The

transition temperatures for gelatinization depend on the availability of water since as the moisture levels of starch are reduced, the starch transition temperatures rise to increasingly higher values as seen in Figure 5.3. Wheat is received from a regional bulgur producer as cleaned i.e. separated from dust, foreign materials and broken wheat. The typical properties of wheat used in experiments are given in Table 5.1. The mass of the wheat, and the corresponding mass of water used for cooking are specified as 13 kg and 26 kg, respectively.



a) Degree of gelatinization against water availability b) Melting temperatures of amylose complexes
Figure 5.3. Gelatinization of starch induced by water and temperature [145].

Table 5.1. Properties of wheat used in experiments.

Provider	Regional bulgur producer			
Color	L^*	a^*	b^*	YI
	51.45	9.6	26.51	77.81
Moisture content, W (% d.b.)				5.99
Protein (% d.b.)				9.01
Ash (% d.b.)				1.48
Specific heat, $c_{p,g}$ (J/kg°C)				1975

Color of the wheat samples were measured by HunterLab Colorimeter [146]. The moisture content of wheat, W was measured at 105 °C using oven method [147]. Kjeldahl method was used to determine the protein contents of wheat using the methodology presented in [147]. The ash contents of wheat were measured at 900 °C [147]. The specific heat of the dry wheat grains was measured by using energy balance applied in equation (4.13). Additionally, variations in grain moisture content during preheating and boiling stages were measured as shown in Table 5.2 by using [147]. This is important to predict the specific heat of wheat grains during preheating, and to predict the time period of cooking process for complete

gelatinization during boiling. The procedure for these measurements was followed by the way: in the CP open to the atmosphere, grain samples were extracted during the preheating process from the mixing temperature to the boiling temperature for 5°C temperature-intervals. After beginning of the boiling process, grain samples were taken out of in a specified time intervals (i.e., 5 min) to be analyzed. The extracted grains were then quenched in cold water. After removal of surface moisture, grains were wrapped and sheltered at 4°C to prevent moisture loss before measuring the moisture content of grains for each batch.

Table 5.2. Variation in grain moisture content.

<i>Variation of moisture content during preheating</i>						
Initial moisture content (% d.b.)		5.99				
Grain moisture content	°C	T_m	85	90	95	100
	(% d.b.)	12.01	16.07	33.21	37.36	39.33
<i>Variation of moisture content during boiling</i>						
Time (min)	W (% d.b.)	Time (min)	W (% d.b.)			
5	42.73	30	77.62			
10	49.23	35	83.58			
15	59.73	40	90.74			
20	68.98	45	94.74			
25	71.6	50	100.3			

5.3.2 Heating of loops

Firstly, the PL is heated by the auxiliary heater to bring the load-temperature to the preset value during the time interval of 9.01 to 9.41 h as seen in Figure 5.4. The mass flowrate of the HTF is regulated by the frequency-controlled gear pump. The flowrate is provided as 1130 kg/h at initial but it falls gradually down 1000 kg/h during heating process. When the load-temperature reaches 137°C at the end of this time interval, the inlet valve of the WPT is opened. The mass flowrate is lowered to 500 kg/h considering the capacity of the auxiliary heater and the time schedule of the process layout. The water charged into the tank is started to be heated from the initial measured temperature of 30°C to the final preheat temperature of 90°C between the time interval of 9.41 to 10.30 h as shown in Figure 5.4. During the preheating process, a mixing device is used to avoid temperature stratification, and to provide uniform temperature within the tank. The heat loss from the loop, and the total

thermal power supplied for both the heat loss and preheating of the process-water are illustrated in Figure 5.4.

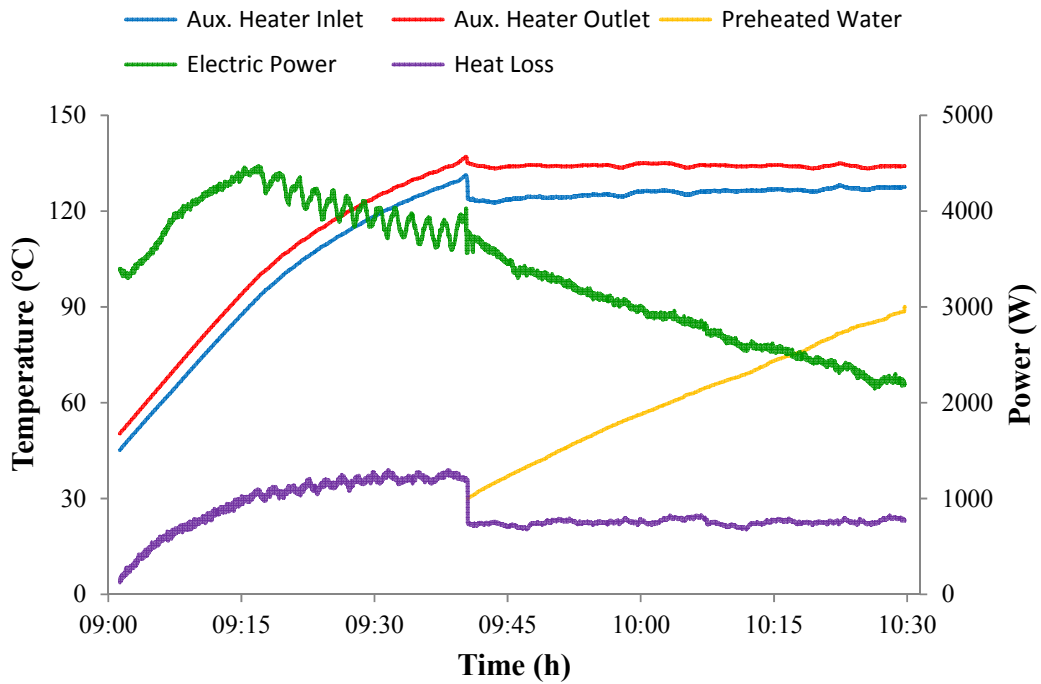


Figure 5.4. Temperature profile and thermal power for the PL.

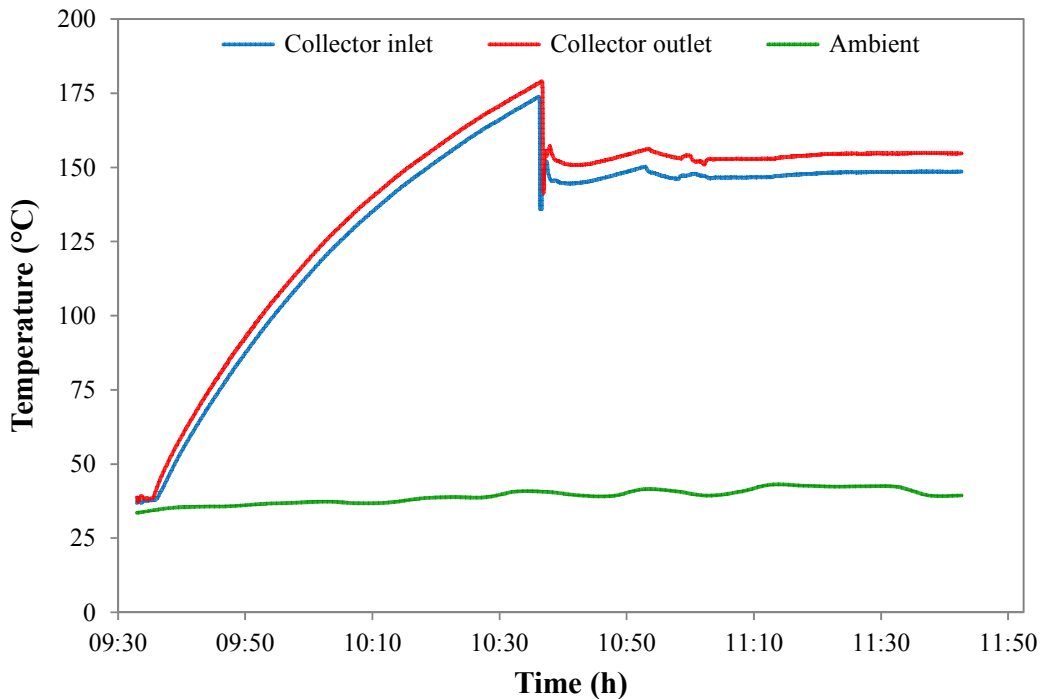


Figure 5.5. Temperature profile for the SL.

The SL is being heated from ambient temperature to 180°C by solar radiation throughout a period of 1-h as shown in Figure 5.5. The flowrate is adjusted by the

gear pump with a constant frequency-control while heating the solar field. The flowrate is initially provided as 1380 kg/h but it falls gradually down 1200 kg/h when the loop temperature has increased to 180°C. Providing higher flowrate at the beginning of the heating operation is intended to develop turbulent currents earlier. Energy discharging to the PL is started with opening the bypass valves. The flowrates are sustained almost 1000 kg/h for both loops during the discharging process. Later, the flow is directed to the BPHE by opening the bypass valves at 10.36 h.

5.3.3 Cooking operation

The temperature of the process-water reaches 90°C at 10.30 h, at this time, the valves of the WPT is closed and the CP' is opened. The HTFs are circulated within the time interval of 10.36 to 10.50 h until the temperature detectors placed in both loops deliver stable readings, and the useful heat gained by the HTF in the SL moves almost constantly again. After these conditions are established, the weighted wheat and the preheated water are poured successively into the CP. The temperature of the discharged water falls down when it is mixed with the wheat which is initially at 27.5°C as shown in Figure 5.6. Until the mixing temperature is raised to the cooking temperature of 100°C, the valves of the CP are in fully-open position. By the time the temperature inside the CP reaches the cooking temperature, the mass flowrate is reduced up to 330 kg/h to keep the central region of the CP at the cooking temperature. More reducing the flowrate causes wheat grains at the central part of the screen to be ungelatinized.

The temperature variations for the inlet and outlet of the BPHE, the CP and the auxiliary heater are shown in Figure 5.6. The inlet temperature of the auxiliary heater is adjusted as the outlet temperature at the cold side of the BPHE due to short distance between them. The temperature profiles exhibit very stable characteristics during cooking operation. The dynamic instability of the solar energy is stabilized by using the auxiliary heater which provides to operate the system at almost steady conditions. Thus sustaining thermal stability during the process heat application is very significant from the view of system design while meeting a variable thermal load demand.

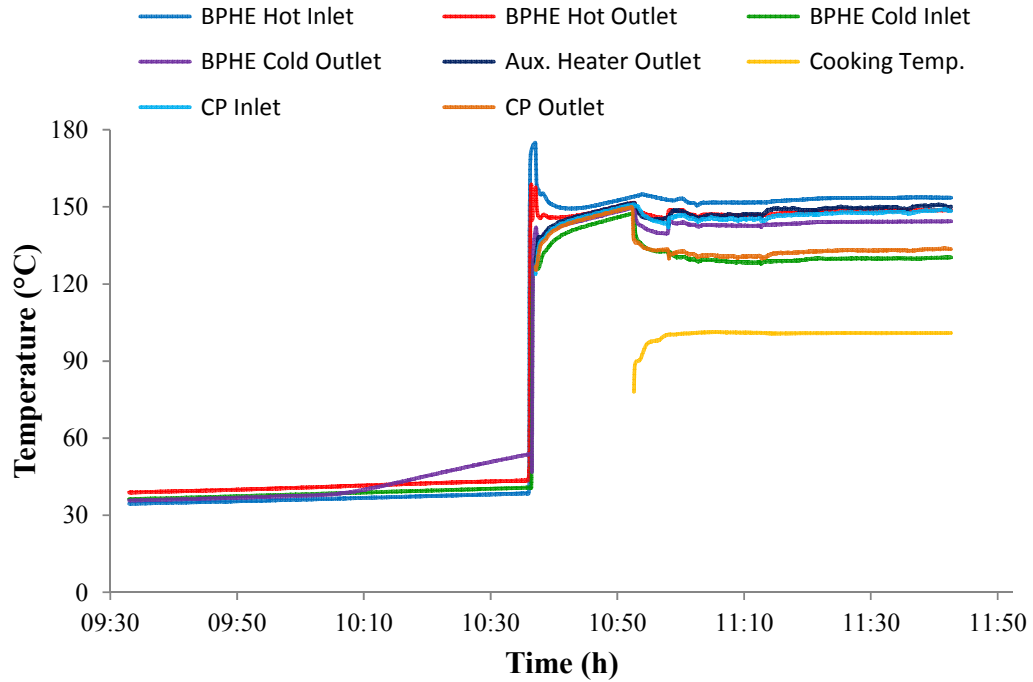


Figure 5.6. Temperature variations in the system components.

When the cooking operation is accomplished, the valves of the CP are completely closed, and the HTF is directed towards the WPT again. The cooked wheat is rested for 2 min in the CP until the vapor inside the CP is completely discharged. Each cooking process is operated in a total time period of 45 min to maintain the gelatinization of the wheat. During cooking operation, the boiled water is directed to a double pipe heat exchanger connected to the pressure relief valve. It is designed for condensation task with an effective heat transfer area of $5.0 \times 10^{-2} \text{ m}^2$. The water being boiled is cooled by the water circulating through the double pipe heat exchanger. At the end of the cooking operation, the total condensed water has been obtained as 3.20 kg. Thus the amount of heat rejected or the boiling loss is estimated basically for the entire cooking process (see equation 5.2). This wasted heat has substantial energy potential that can be considered for heating the process-water in the backup tank up to 90°C . In case of recovering this potential, the process-water will be ready for the next cooking operation. This will provide high daily production capacity for continuous system operation, and better energy efficiency for the application.

$$Q_r = m_v h_{fg} = m_w c_{p,w} (T_p - T_w) \quad (5.2)$$

5.3.4 Performance parameters

In this part, the SAPH application for each system component is analyzed by introducing experimental data and performance parameters.

5.3.4.1 Useful heat gain

The net energy transferred to the HTF by the solar field is related by the useful heat gain which leads the temperature change for the HTF flowing through the receiver tube of the PTSC array. The energy gained by the HTF can be calculated by using equation (5.3).

$$\dot{Q}_u = \dot{m}_{HTF,2} c_{p,HTF} (T_{ex} - T_{in}) \quad (5.3)$$

where $\dot{m}_{HTF,2}$ is the mass flowrate of the HTF circulating in the SL. T_{in} and T_{ex} denote the instant measured temperatures for the HTF at the inlet and exit of the PTSC array. $c_{p,HTF}$ is the average specific heat of the HTF evaluated at the average temperature $(T_{in} + T_{ex})/2$ using the selected working fluid whose properties are given in Appendix A.

5.3.4.2 Thermal efficiency

The thermal efficiency of the PTSC array is defined as the ratio of the useful heat transferred the HTF to the beam radiation incident on the aperture area of the array.

$$\eta_t = \frac{\dot{Q}_u}{A_a \times I_b} \quad (5.4)$$

5.3.4.3 Utilization ratio

It is related with what fraction of the useful heat gain is discharged and utilized instantly in the PL. The rate of discharged energy and the utilization ratio can be calculated by using the following relations.

$$\dot{Q}_d = \dot{m}_{HTF,1} c_{p,HTF} (T_{c,out} - T_{c,in}) \quad (5.5)$$

$$\phi = \frac{\dot{Q}_d}{\dot{Q}_u} \quad (5.6)$$

where $\dot{m}_{HTF,1}$ is the mass flowrate of the HTF circulating in the PL. $T_{c,in}$ and $T_{c,out}$ denote the instant measured temperatures of the HTF at the inlet and outlet of the BPHE. $c_{p,HTF}$ is the average specific heat of the HTF evaluated at the average temperature $(T_{c,in} + T_{c,out})/2$.

5.3.4.4 Overall system efficiency

The overall efficiency of the system is a measure of what portion of the beam radiation falling on the total aperture area of the PTSC array is transferred to the PL.

$$\eta_o = \frac{\dot{Q}_d}{A_a \times I_b} \quad (5.7)$$

5.4 System operation

The results obtained from the test day are analyzed and discussed in detail. Useful heat gained by the solar field, the fraction of the useful power transferred to the PL, thermal power supplied by the auxiliary heater, cooking load, preheating load and the overall heat losses from the loops are investigated.

The performance of the PTSC is evaluated by using the parameters; beam radiation, and inlet and outlet temperatures of the HTF through the absorber tube for a given mass flowrate. Figure 5.7 indicates the variation in the useful heat gain. It is seen that the useful heat gain bounces when the bypass valves are opened on the leading time of 10.36 h due to thermal instability (originating from high temperature difference between the loops) in the temperature detectors. The useful heat gain is directly related to the thermal performance of the PTSC which is a function of beam

radiation. The variation in the beam radiation and the thermal efficiency are shown in Figure 5.8.

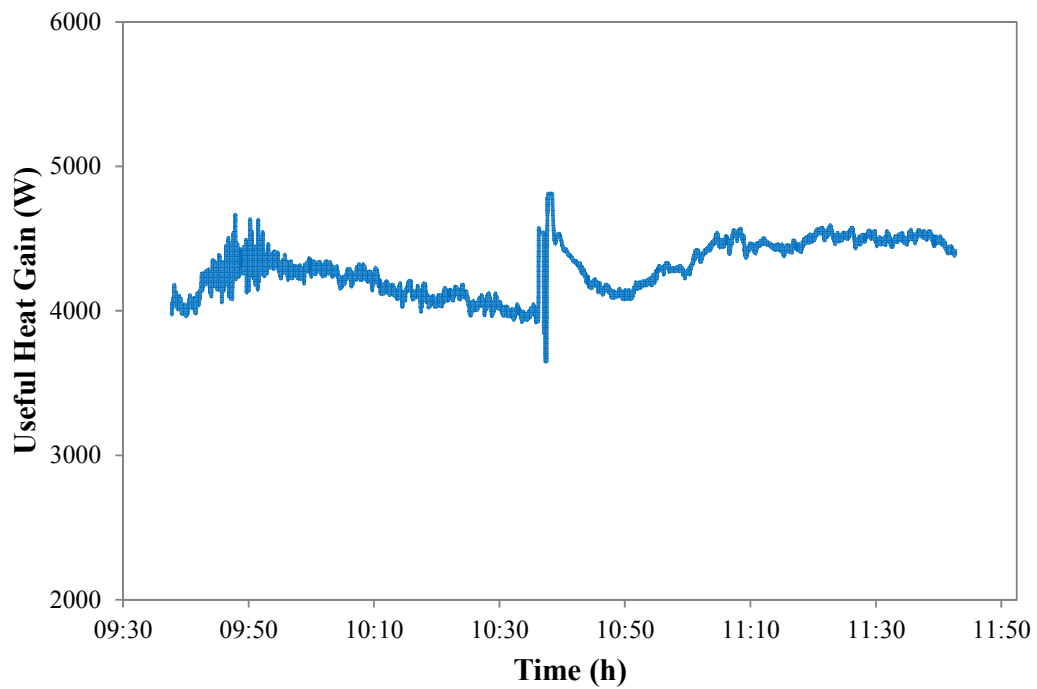


Figure 5.7. Variation in the useful heat gain.

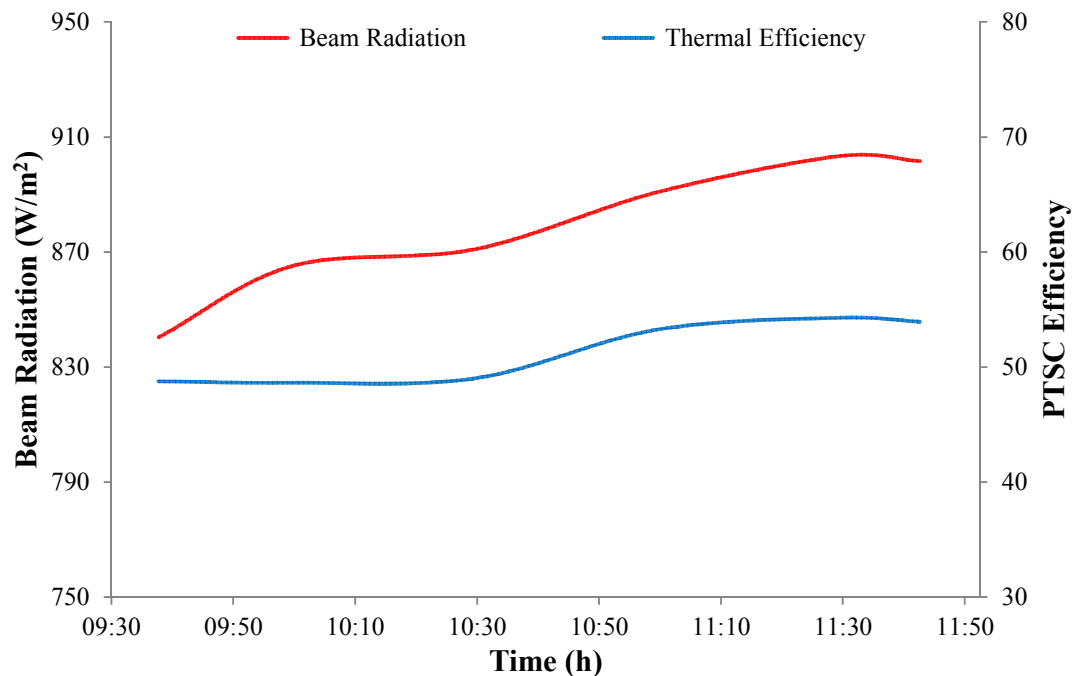


Figure 5.8. Variation of the beam radiation and thermal efficiency.

It is seen from the figure that increasing in the intensity of the beam radiation increases the useful heat gain by the HTF. Therefore the thermal efficiency of the

PTSC follows the variation in the beam radiation. Since it strongly depends on incident beam radiation, optical efficiency of the PTSC, and operating conditions [18,66]. As the test results are analyzed, the behavior of the PTSC used in the experimental study exhibits similar character compared to [148], and the results obtained for two studies show parallelism. When the inlet temperature of the HTF increases, the heat loss from the receiver becomes much higher. Thus the operating temperature should be selected as low as possible when process suitability and layout are considered. In order to obtain maximum possible heat gain from the solar at favorable level, the HTF is operated at about 150°C at turbulent regime. Operating conditions such as temperature and flow regime affect predominantly the thermal efficiency [66]. The thermal efficiency remains nearly constant between the time interval of 9.38 and 10.30 h since the flow regime is predominantly laminar up to 100°C, and the heat loss from the receiver tube of the PTSC is low at lower operating temperatures. This degrades the convection heat transfer coefficient within the absorber pipe, and thus the useful heat gain. On the other hand, at higher temperatures (above 100°C), the flow regime becomes to turn turbulent which increases the thermal efficiency but increasing in heat losses degrade the thermal efficiency. In fact, increase in the mass flowrate causes to develop turbulent currents within the absorber pipe so that the HTF transfers more energy from the inner surface of the pipe. The higher the mass flowrate, the higher the fluid motion which increases the convection heat transfer coefficient of the HTF, and thus the useful heat gain transferred to the HTF. However, when the flow regime turns to turbulent, which is directly related with mass flowrate and viscosity of the HTF, at relatively higher temperatures, i.e. 100°C, the heat loss from the receiver tube increases more and more thus the useful heat gain drops. On the other hand, the effect of cosine losses on the thermal efficiency increases toward noon increasing with the incidence angle of the PTSC aperture. This also decreases the useful heat gain transferred to the HTF.

Figure 5.9 illustrates the variation in the cooking load, the discharged thermal power from the PL to the transferred power for the SL, and the auxiliary power supply throughout the cooking process. It is observed that the rate of energy discharged increases through the time interval of 10.52 and 10.58 h since the mixture in the CP requires more sensible energy to reach the cooking temperature. In this

time interval, the temperature of the SL falls slightly down due to massive energy suction of the mixture, rapid-response incapability of the auxiliary heater against power demand, and high overall heat losses although the auxiliary heater functions at maximum rate which ensures not to exceed the recommended film temperature of the HTF in order to prevent thermal cracking. Since the auxiliary heater is made of CHE enclosed by electric heater, and the temperature of the surface (between the CHE and the electric heater) is controlled by PID which receives the signal from the thermocouple placed to the corresponding surface. As it is seen from Figure 5.9, the cooking load for the mixture falls steeply down due to the fact that the temperature difference between the load-temperature and the mixture temperature decreases. After the cooking process initiates, the cooking load drops remarkably. The rate of discharged power from the SL stabilizes, and the auxiliary heater operates only to meet the thermal losses from the installations (the pipelines, the heat exchanger, the TET and metal parts such as pump, flowmeter). About one-fifth of the useful heat gain is lost from the SL thus the system performance falls below the maximum possible efficiency that could not be obtained.

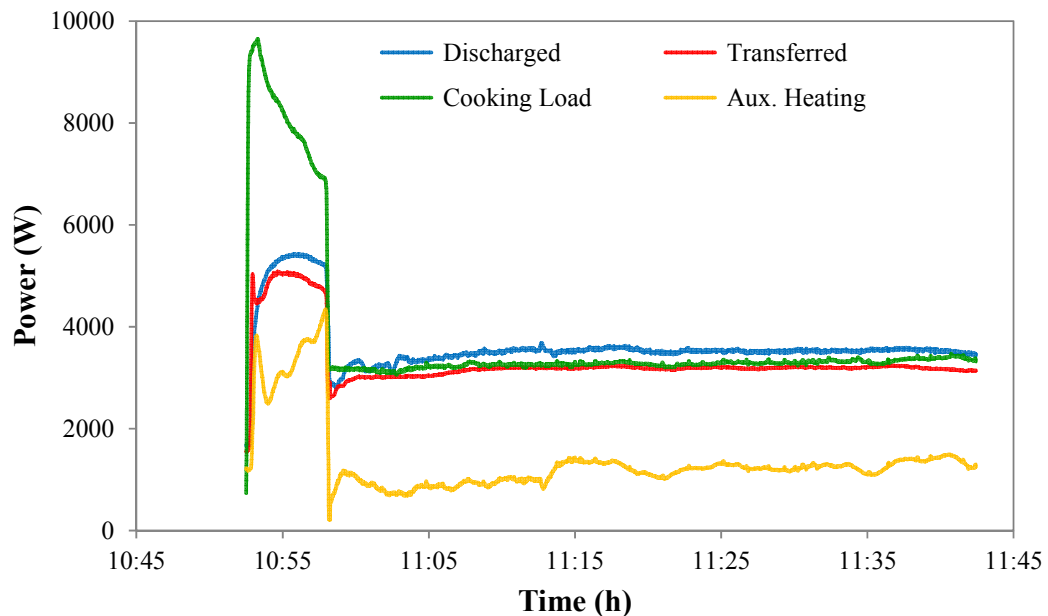


Figure 5.9. Variation in the discharged/transferred power, cooking load and auxiliary heating.

The resulting utilization ratio and the overall system efficiency of the SAPH application during the cooking process are shown in Figure 5.10. It is figured out that the SAPH system yields average utilization of 70.5% during the test period of 10.58–

11.43 h. The percent of the utilization depends strongly on the operating temperatures of the loops, and the heat transfer area of the BPHE. Poor insulation of the system components or the undersized thermal load for the CP lessen the utilization ratio principally. Thus lowering the overall heat loss generates an additional potential for the discharged rate. Proper sizing of the IHHE used in CP and the PTSC array are essential from the view of system design that provides maximum possible utilization. Namely, the temperature difference between the inlet temperatures of the hot and cold sides of the BPHE, and the heat transfer area of the BPHE are very critical parameters on the utilization ratio. Thus, lowering the return-temperature (i.e. the inlet temperature on the cold side of the BPHE) generates additional potential for elevating the utilization ratio in case that it is less than 1. This is the case when the energy discharged is lower than the energy collected as useful heat gain. Otherwise, the operating temperature of the SL falls down. If this is the case, the control of the SAPH system will be difficult due to temperature fluctuations.

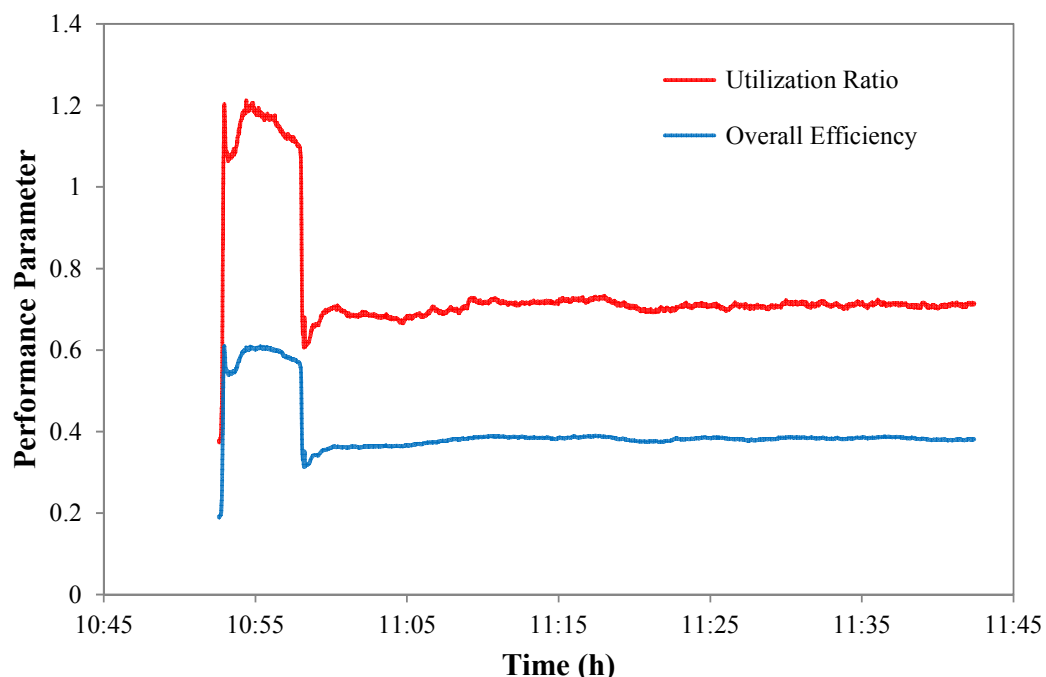


Figure 5.10. Variation in the utilization ratio and overall system efficiency.

It is observed from Figure 5.10 that the overall efficiency has the average value of 37.9% during the test period of 10.58–11.43 h. The efficiency increases at the start of the charging process due to large temperature difference between the mixing and the load-temperatures. As a result, the return-temperature drops more, and thus the

discharged thermal power from the SL to the PL increases. After 10.58 h, the overall efficiency decreases appreciably, and it shows almost constant value until 11.43 h because of the decrease in the cooking load relative to the useful heat gain. In fact, the efficiency of the system can be related by this constant value under the operating conditions that are applied. Because the temperatures and the auxiliary heating power measured on the system are very stable and almost constant. It is seen that the overall efficiency depends particularly on the thermal efficiency of the PTSC array, and the parameters affecting the utilization ratio. It is provided that increasing in useful heat gain, reduction in heat losses, and increasing in the thermal load of the process heat, the overall system efficiency will show an increasing trend.

5.5 Performance tests

The experiment conducted in August 29 presents the test results of the SAPH system under the conditions being applied. But experiencing only single test under constant operating conditions is not sufficient to have a general idea about the system performance. In order to make a reasonable performance analysis, the effective parameters are defined on the system to observe the variation in the performance. Thus the SAPH system is operated and tested under different load profiles and temperatures on the 29th of August, 22nd and 25th of September, 2013. The load temperature is around 150°C for the test being performed in August 29. It is lowered to 140°C and 130°C for the days demonstrated in Figure 5.11. The test results indicate that reduction in load temperature extends the preheating period of the cooking process. Since energy transfer to the mixture drops due to decrease in the temperature difference between the mixture and the CP inlet. This circumstance may not be desirable due to reduction of daily bulgur production. Furthermore, lowering the load temperature decreases the discharged power and consequently the utilization ratio. Along with decreasing in the discharged power raises the operating loop temperature on the SL. Hence selection of proper size for the BPHE requires great importance to obtain maximum yield from the system. It is figured out that the SAPH system yields average utilization of 55.9% and 47.7% for 140°C and 130°C load temperatures, respectively during the boiling process. The corresponding overall efficiencies have obtained averagely as 23.6% and 19.8% during the same test period for 140°C and 130°C load temperatures, respectively.

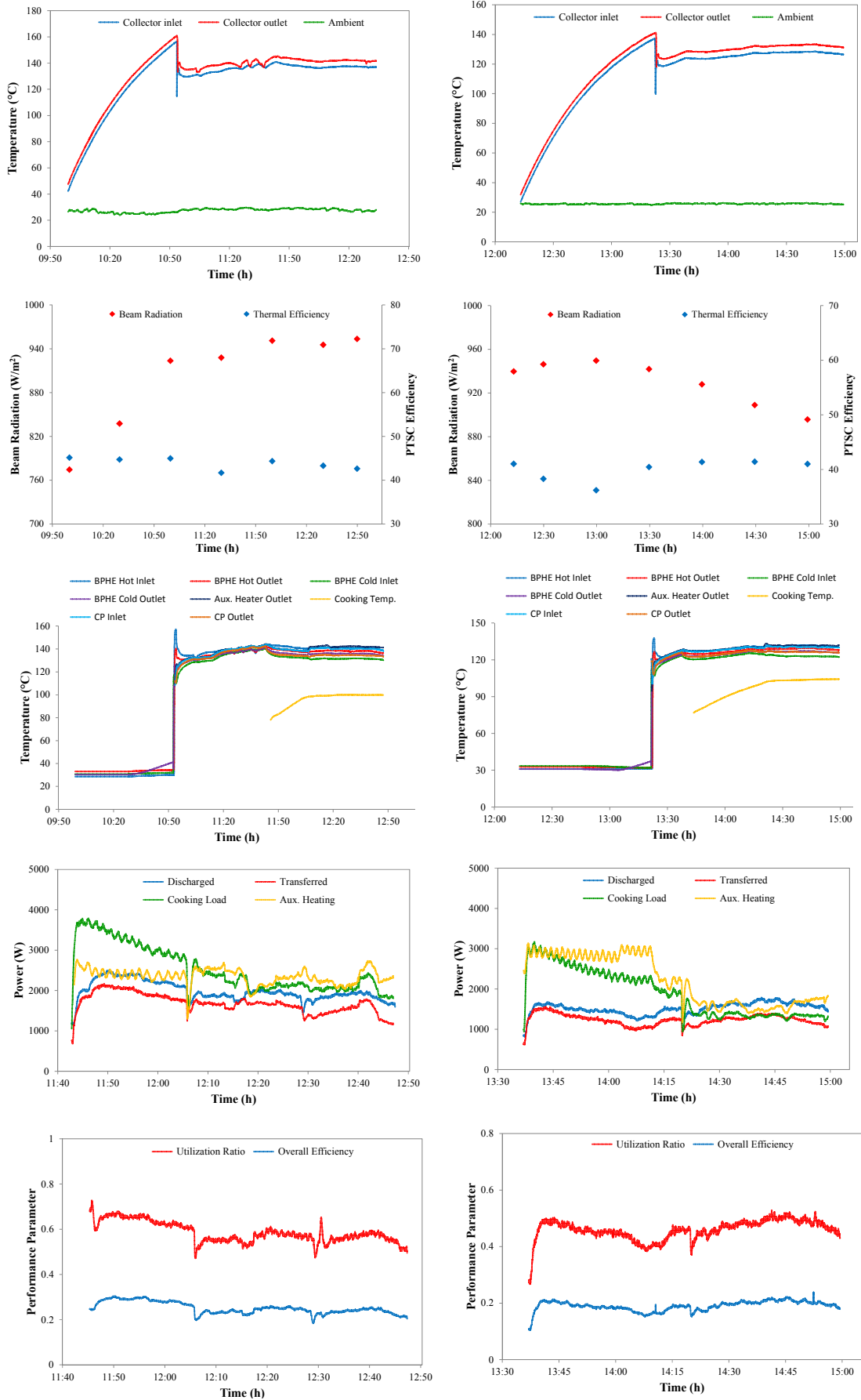


Figure 5.11. Test results of the experiments performed in September 22, 2013 (Left column), September 25, 2013 (Right column).

5.6 Model validation for system components

Results of the developed models for the CP (IHHE type) and BPHE are compared with the experimental results. The model outputs for the CP are obtained at different cooking parameters (inlet and boiling temperatures) as shown in Table 5.3. It is seen that the model yields accurate results in terms of predicting heat transfer area of the IHHE for the given experimental parameters. This validation is very significant for describing the most effective parameters on cooking process. Moreover, it will be useful in the design stage of large-scale CP.

Table 5.3. Model prediction for heat transfer area of the IHHE.

Flow rate kg/h	T_{in} °C	T_{ex} °C	T_{sat} °C	T_a °C	Cooking time sec	Model A_s
377.8	143.75	129.81	100.90	41.46	2700	0.267
556.9	115.01	111.11	99.27	38.98	2700	0.299
519.4	129.48	121.24	99.81	37.08	2700	0.271
570.9	122.16	116.17	99.76	37.93	2700	0.292
685.4	130.97	125.42	110.24	33.72	2220	0.284
813.1	130.83	128.18	120.19	25.67	1400	0.313

The model outputs for the BPHE are obtained for different mass flowrates and operating temperatures as shown in Table 5.4. It is seen that the model yields reasonable results in terms of predicting the outlet temperatures at the hot and cold side of the BPHE for the given experimental parameters. This validation is very significant for predicting the outlet temperatures when the BPHE operates different working conditions. Additionally, it plays important role in the design stage for the selection of BPHE with proper size. Moreover, it aids to size the capacity of auxiliary heater and the collector area needed for system design.

Table 5.4. Model prediction for fluid outlet temperatures of the BPHE.

Flowrate at hot side kg/h	Flowrate at cold side kg/h	Experimental data in °C				Model	
		$T_{h,i}$	$T_{h,out}$	$T_{c,i}$	$T_{c,out}$	$T_{h,out}$	$T_{c,out}$
1034	328	147.2	143.1	126.3	138.7	143.6	138.1
1050	496	134.8	131.1	119.7	127.1	131.7	126.6
1062	501	124.9	120.9	108.8	116.4	121.6	115.9
1048	652	136.1	132.2	122.6	128.4	132.9	128.0
1046	807	138.7	134.5	125.8	130.6	135.2	130.4
1032	1000	150.4	143.3	129.1	136.9	144.1	135.9

5.7 Design aspects for cooking pot

In this section, design perspectives for CP are presented, and the performance analyses of the designed two different CPs (annulus and externally helicoidal types) are discussed in detail. Furthermore, the cooking parameters for all the CPs are investigated in terms of nutritional view.

Table 5.5 also indicates the cooking parameters performed at different boiling operations for IHHE type CP. Results show that the inner structure of the grains, their initial moisture content and thermophysical properties affect the cooking quality, cooking time for complete gelatinization. The complete gelatinization of wheat grains depends strongly on properties of wheat, cooking time and boiling temperature. Water absorption of wheat samples (i.e., moisture content) during cooking process can give information about the level of gelatinization. In the following parts, the cooking parameters will be examined more detailed.

Table 5.5. Properties of parboiled wheat after cooking operation for IHHE.

T_b °C	Color			Protein % d.b.	Ash % d.b.	BOD_5 mg/L×10	W % d.b.	
	L^*	a^*	b^*					
100	51.5	8.88	31.7	85.4	10.943	1.261	215.00	103.30
100	50.3	8.55	30.4	83.9	10.398	1.316	212.50	108.69
100	51.3	9.22	30.3	86.5	10.853	1.325	222.67	114.00
100	51.0	8.85	31.7	85.6	11.575	1.209	220.50	108.29
100	50.7	9.06	31.9	84.8	11.034	1.219	182.50	103.75
100	50.7	9.15	31.3	87.1	9.655	1.284	140.25	93.66
110	52.9	7.00	26.4	72.9	9.521	1.584	228.00	100.82
110	53.4	7.32	30.9	80.1	9.133	1.076	197.50	98.54
120	52.6	7.59	30.2	80.5	9.482	1.097	144.75	101.16
120	50.3	7.46	28.0	77.2	10.367	1.237	216.33	111.05

5.7.1 Annulus type

Figure 5.12 demonstrates a new design concept for CP which is described as annulus type heat exchanger (AHE). Technical specifications of the design involve the parameters given in Table 5.6. Although the production stage of the design is somewhat harder than IHHE, in this concept, the HTF flows at the outside of the CP thus the leakage problem will not be in consideration for producing food in hygienic conditions. The observations show that this design has some complications such as

problem of trapped air at the cornered regions of the annulus. Furthermore, a dead region which occurs within the annulus suffocates the heat transfer but can be improved by new design which involves baffles to manipulate the flow. The flow regime in the annulus region is the most effective parameter which influences the convection heat transfer coefficient, and the energy transferred to the CP that will meet the specified cooking load. The drawback of this design is that the flow regime of the HTF falls usually into laminar region even if the temperature of the HTF is high. Since the characteristic length of the annulus (outer pot diameter) is big, the mean velocity of the HTF and thus Re depending on it decreases together. Increasing the flowrate at a certain level forms a pressure surge at the inlet side of the CP. But in lower flow rates and temperatures, the regime of the flow may turn to laminar or transition regime which degrades the convection heat transfer coefficient within the annulus region. Hence the thermal efficiency of the CP drops severely.

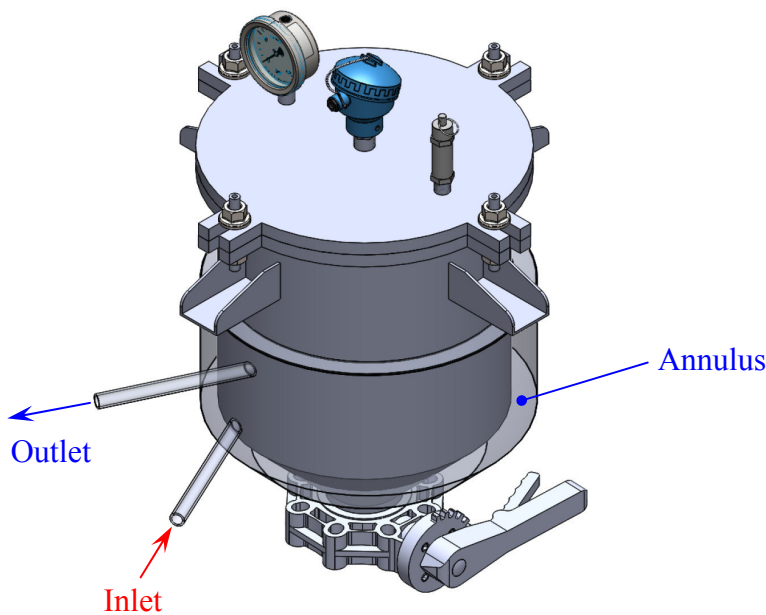


Figure 5.12. CP with AHE.

Table 5.6. Specifications of the AHE.

Sheet material	316L SS
Inner pot diameter	0.38 m
Material thickness	0.002 m
Annulus distance	0.0275 m
Effective heat transfer area	0.30 m ²
Insulation material	Stone wool

When the thermal performance of the pot is compared to the IHHE, for the same flowrate, inlet and cooking temperatures, it is found that the AHE design exhibits much lower performance although its effective heat transfer area is slightly higher than the former. In other words, the pot having higher thermal performance will cause the HTF to undergo higher temperature difference which provides to raise the energy transferred to the mixture.

Figure 5.13 indicates a typical cooking operation realizing at 110°C boiling point. During preheating process, the temperature of the mixture is increased by energy transfer to reach it to the boiling temperature. The mass flowrate of the HTF is adjusted depending on the process time in which the preheating treatment is to be accomplished. Once the boiling begins, the flowrate is decreased to the level at which the minimum energy transfer is sufficient to keep the boiling temperature constant. The amount of flowrate is obtained higher compared to the IHHE due to having low thermal performance. This means that for the same of flowrate, the effective heat transfer area in the AHE type must have higher heat transfer surface area, in other words the CP should have larger size to achieve the same task.

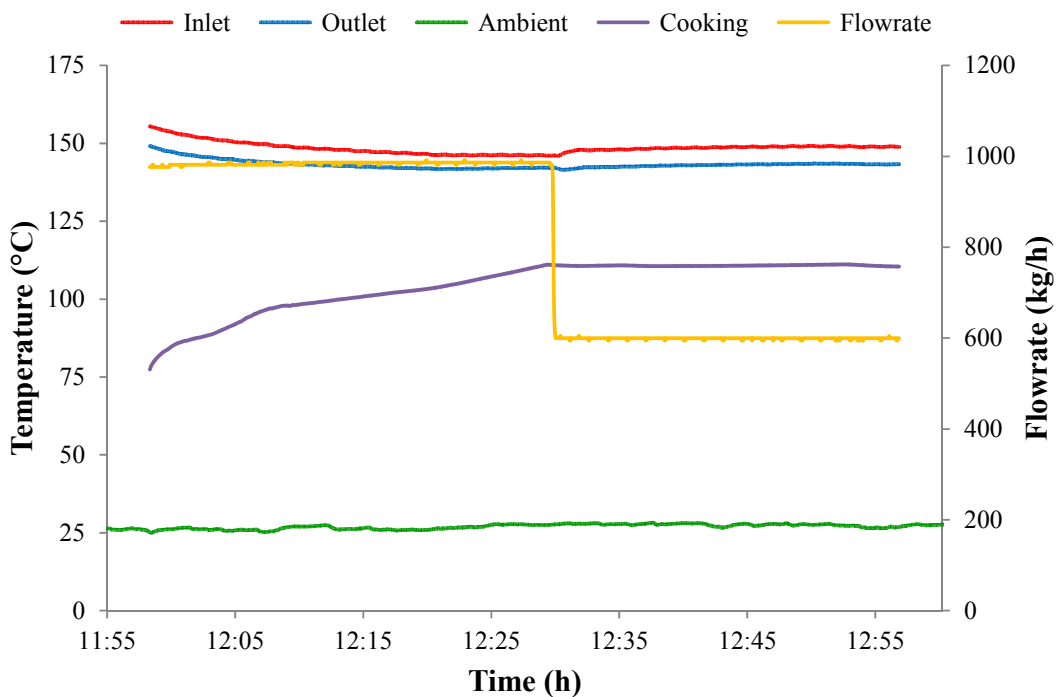


Figure 5.13. Temperature variation for the AHE during cooking operation.

Table 5.7 indicates the cooking parameters for different boiling operations. When the properties of the parboiled wheat are analyzed, it is seen that the method of cooking is not much effective factor on the final product. These results are not spectacular since there is not a certain relation between BOD_5 and W . Outwardly, it is expected that when the initial moisture contents of wheat grains are the same, and the complete gelatinization of wheat grains is maintained at the end of cooking operation with 100% moisture content, BOD_5 values could be identical in different boiling temperatures. However, at higher boiling temperatures the pressure on the wheat grains will be much more, this causes much more leached substances to pass into the water.

Table 5.7. Properties of parboiled wheat after cooking operation for the AHE.

T_b °C	Color			YI	Protein % d.b.	Ash % d.b.	BOD_5 mg/L×10	W % d.b.
	L^*	a^*	b^*					
100	50.83	9.05	32.01	86.07	9.254	1.339	157.75	98.41
100	51.39	8.77	30.57	83.52	11.144	1.301	209.00	93.47
110	51.18	9.03	31.22	86.47	9.688	1.363	161.00	101.01
110	51.52	8.61	30.83	83.55	11.045	1.156	136.00	93.80

5.7.2 Externally coiled type

Figure 5.14 demonstrates another designed CP which is described as externally helicoidal heat exchanger (EHHE). Technical specifications of the design involve the parameters given in Table 5.8.

Table 5.8. Specifications of the EHHE.

Sheet material	316L SS
Inner pot diameter	0.38 m
Material thickness	0.002 m
Cross-section of coil	0.026×0.026 m
Coil pitch	0.05 m
Coil radius	0.205 m
Effective heat transfer area	0.175 m ²
Insulation material	Stone wool

The production stage of the EHHE is the most complicated among three designs. The major complication in this design is considered to be using the outside of the pot

as heat transfer area. This can make the design dysfunctional since the space between the coils or unwetted region will not be directly exposed to convection heat transfer by the HTF. Contrarily, leakage is not important relative to the IHHE. In case of using thermal oil (including toxic substances) as a working fluid in the EHHE, and if any leakage is available in the CP, thermal oil will not blend with cooking media.

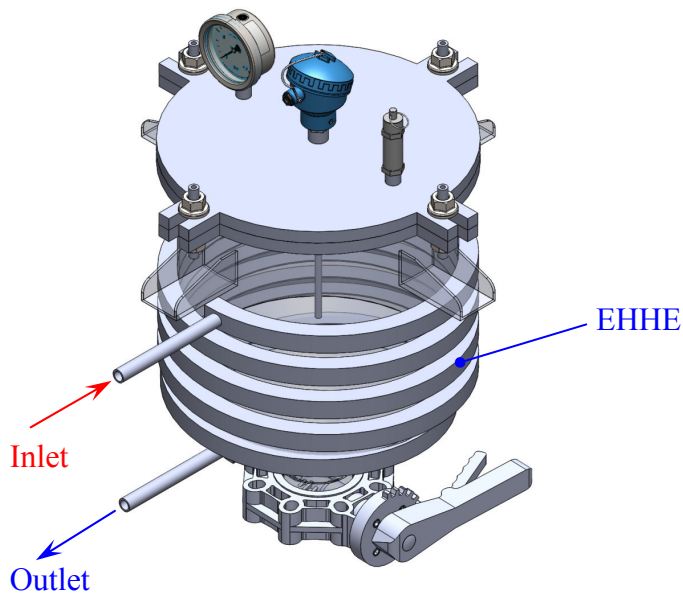


Figure 5.14. CP with EHHE.

When the thermal performance of the pot is compared to the IHHE, for the same flowrate, inlet and cooking temperatures, it is inferred that this design could exhibit higher performance when its effective heat transfer area is made identical with the former. Furthermore, the thermal performance of a heat exchanger depends strongly on the heat transfer area and Re . If these two parameters are enhanced, the energy transfer will be much easy. Re depends on mean velocity, u_m which is a function of cross-sectional area of the coil in which the HTF flows. Thus the mean velocity of the EHHE will be lower than that of the IHHE. It means that for the same amount of flowrate passed in both coils, the convection heat transfer coefficient could be higher relying on the cross-section.

Figure 5.15 indicates a typical cooking operation realizing at 100°C boiling point. In this operation, the procedure applied for cooking is the same with the

former designs. The amount of flowrate is obtained higher compared to the IHHE to keep the boiling at constant temperature due to having low heat transfer area.

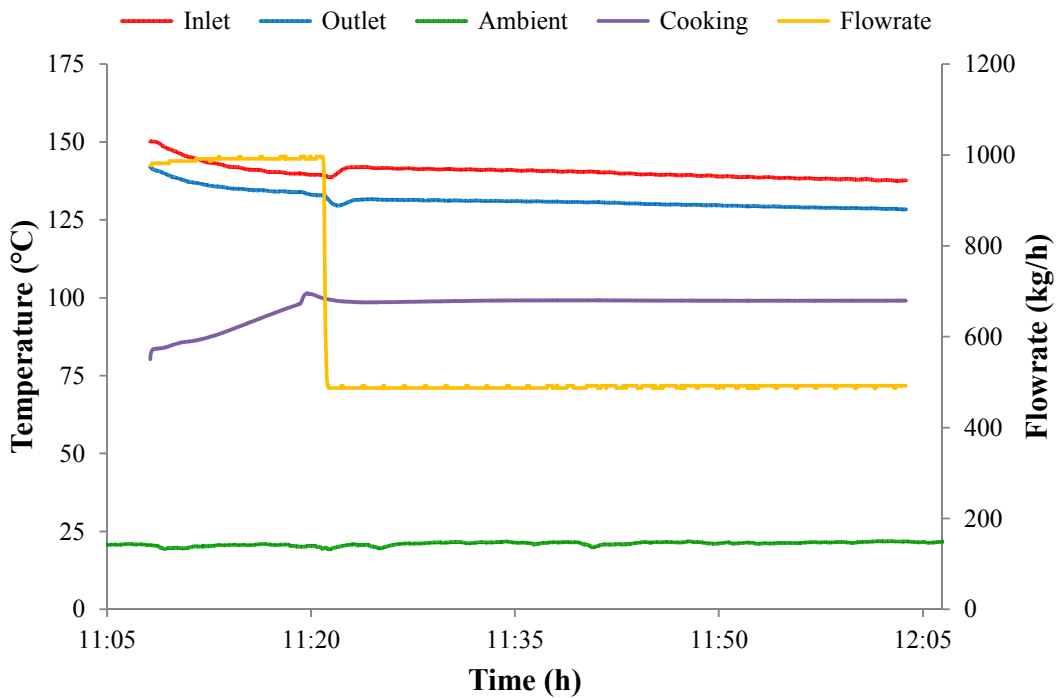


Figure 5.15. Temperature variation for the EHHE during cooking operation.

Table 5.9 indicates the cooking parameters for different boiling operations. As it is observed, there is no strict rule between the final product and the cooking parameters such as BOD_5 , W and cooking temperature. In order to understand the phenomena lying under this fact, more research could be performed in this area.

Table 5.9. Properties of parboiled wheat after cooking operation for the EHHE.

T_b °C	Color			Protein % d.b.	Ash % d.b.	BOD_5 mg/L×10	W % d.b.
	L^*	a^*	b^*				
100	51.80	7.39	28.38	77.91	11.457	1.109	146.00
110	51.16	7.35	29.20	78.99	10.502	1.174	216.50
120	52.17	9.04	28.80	80.12	10.356	1.191	125.80

5.8 Summary

An experimental investigation on the performance evaluation of a SAPH application integrated with a parabolic trough solar collector array has been carried out. An appropriate process arrangement has been proposed for cooking applications

in industrial areas. Furthermore, analyzing and testing of the system components have been conducted in detail. Performance parameters such as the collector array's instantaneous efficiency, energy discharged, thermal losses, utilization ratio, and the overall system efficiency have been evaluated by testing the experimental system under different operating conditions. For cooking application, three different CP were designed, and their performance outputs were evaluated from the view of thermal load capacity, speed of cooking time, quality of wheat cooked and process suitability.

CHAPTER 6

TRANSIENT SIMULATION OF SAPH APPLICATION

6.1 Introduction

Simulations and experiments provide to determine dynamic system behavior and integrated performance. Experimental studies of component performance are the basis of confidence in component modeling. Comparison of physical measurements and simulations is the key of validating the component model. The conclusions to be drawn from these validations can provide a wealth of information about solar processes and their thermal design. In this chapter, simultaneous solutions of the sets of models that describe the performance of the SAPH application are analyzed by the transient system simulation.

6.2 Transient analysis

The SAPH application was simulated instantaneously by writing an algorithm in Visual Basic 6.0. The developed model equations for PTSC array, BPHE, thermal load for cooking, TET and pipe field were included in the algorithm and solved iteratively. The pipe field is analyzed by using *finite volume difference method*. The algorithm uses a database for beam radiation measured in 2012-year at 37°16'N latitude and 39°00'E longitude with 10-min time intervals. Figure 6.1 shows the monthly averaged distribution of this data record.

6.3 System operation

The system layout shown in Figure 5.1 was employed for simulation. The PL is operated in full time sustaining the cooking load given in Figure 5.9. The load

temperature is specified as 150°C in the PL. The SL is operated until the set temperature (i.e., 150°C) assigned for the outlet of the PTSC array is reached. When the given set temperature is reached, the bypass valves in both loops are opened and the energy discharge to the PL starts. In this condition, the return temperature of the CP will be heated by discharged energy. If the discharged energy is not sufficient to increase the set temperature at the PL, the auxiliary heater will supply energy to reach it to the set temperature. If the outlet temperature of the BPHE at the hot side rises above the set temperature, the obtained temperature will be the inlet temperature of the CP. This process continues until the return temperature of the CP falls below the outlet temperature of the PTSC array in daily operation.

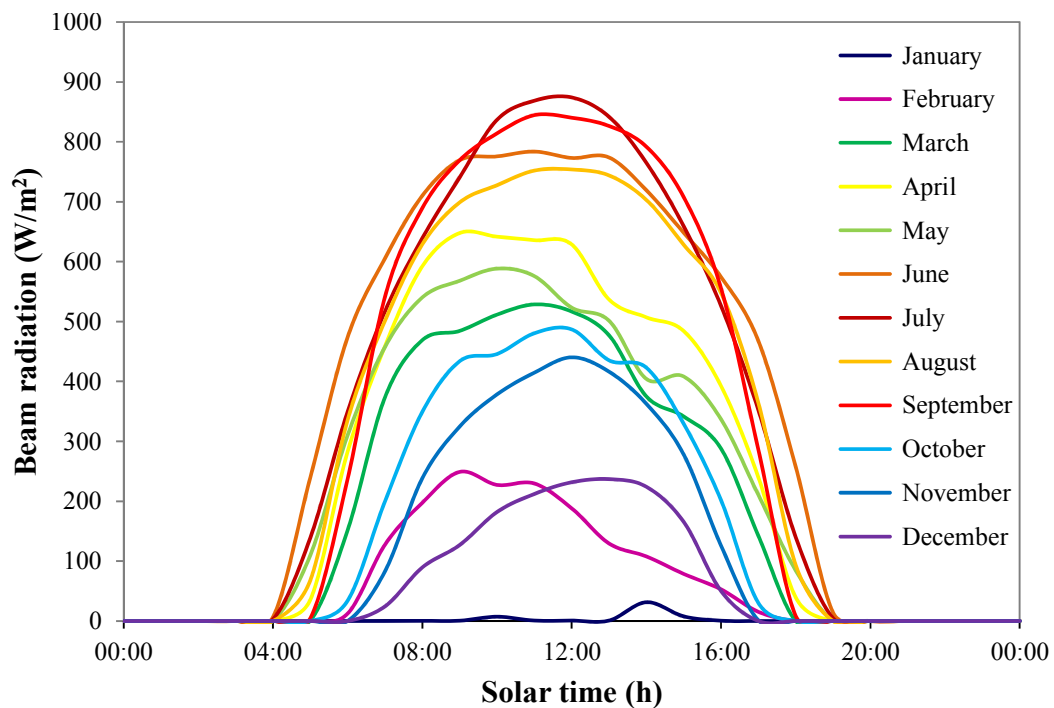


Figure 6.1. Monthly average beam radiation used for simulation.

6.4 Simulation results

If the parameters, given in Table 6.1, are applied to the simulation, the variation of monthly solar fraction is obtained as Figure 6.2. As it is expected, the solar fraction increases in summer season due to high solar potential. The simulation supposes that if the system operates under given conditions in full time of day, the maximum solar fraction is obtained in June. This result is expected since it is clear that north-south axis tracking significantly increases the collected incident beam

radiation on the collector aperture when the summer solstice occurs. The annual performance of the system was obtained as 20.8% when the given conditions in Table 6.1 and Figure 6.2 were applied. This performance depends on many system and operation parameters. The most critical ones can be treated as monthly beam radiation level, cooking load, load temperature, ambient conditions, heat loss from system components, size of the BPHE and the thermal performance of the PTSC.

Table 6.1. System parameters used in simulation.

Location	Gaziantep
Solar collector [67]	Smirro300
Thermal storage	None
Cooking load	Variable
Set temperature	150°C
PL pipe length	14 m
SL pipe length	21 m
Pipe inner/outer diameter	0.0297/0.0337 m
Pipe insulation [133]	Glass wool

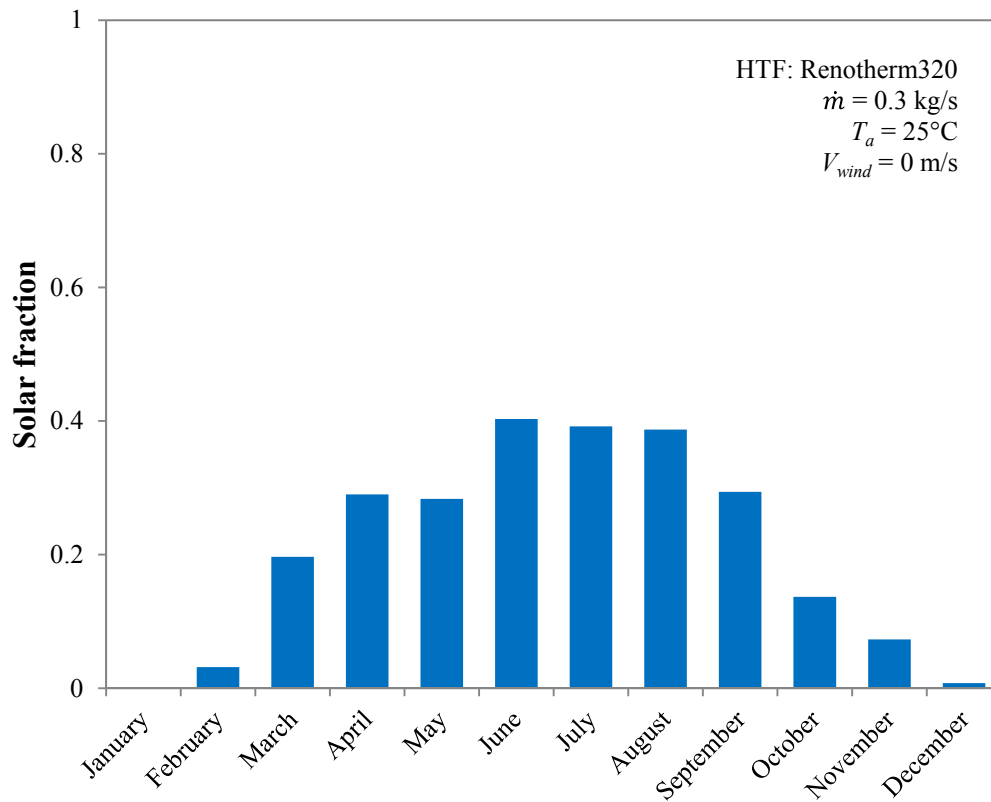


Figure 6.2. Variation of solar fraction with respect to months.

Figure 6.3 indicates the simulation results obtained for the mid-day of June, August and October to see the system outputs under different solar conditions. The variation of beam radiation and the temperatures obtained instantly at the inlet/outlet of the system components are shown under the corresponding days. The temperatures follow the variation of the beam radiation as expected. The temperatures in constant level display the set temperatures for the outlet temperature of the auxiliary heater or the load temperature of the CP.

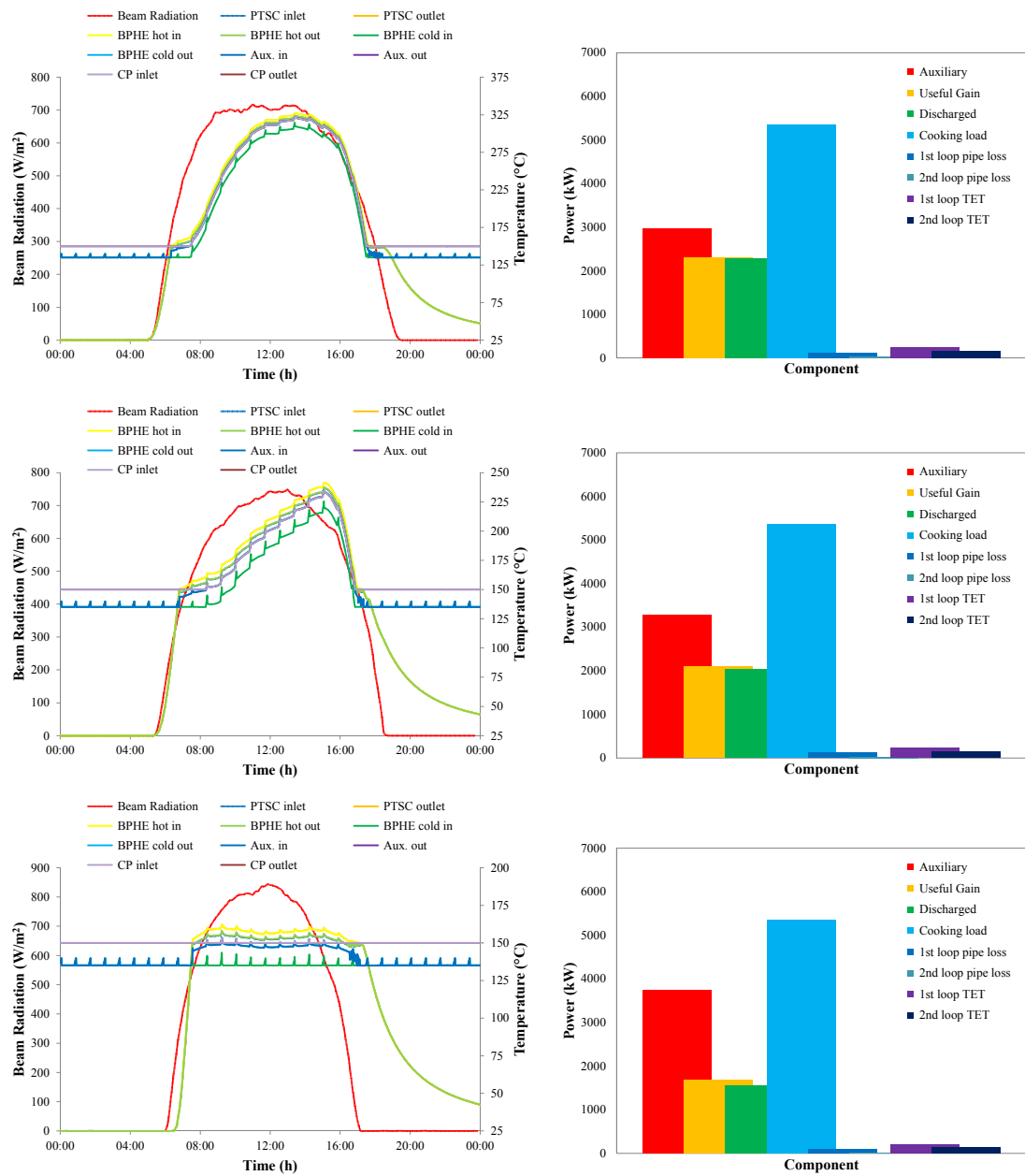


Figure 6.3. Simulation results for the days in June 15, 2012 (First row); August 15, 2012 (Second row); October 15, 2012 (Third row).

Care must be exercised that the operating temperatures vary depending on the daily beam radiation level. In June and August, the average beam radiation is high relative to October as a result the useful heat gain transferred to the working fluid increases. Thus, the HTF in the SL is overheated and exceeds the set temperature in June and August as seen from Figure 6.3. The reasons lying under this attribute can be accounted as high performance exhibition of the PTSC and low heat loss from the system components. Since the simulations have been performed by the provided inputs which may not always match the actual operating conditions. On the other hand, the proper sizing of the system components is necessary to prevent the overdamped temperature responses. The present system size is more suitable for the

Figure 6.3 also shows the daily energy policy of the system components. As it is seen, the discharged power transferred to the PL is low in October relative to June. This causes low solar fraction and consequently overall system efficiency. As the daily overall efficiencies are analyzed for the days in June, August and October, the corresponding results are obtained as 40.1%, 35.6% and 27.5%, respectively.

6.5 Summary

Transient analysis of the SAPH system was accomplished for the provided inputs, and the performance characteristics of the system were investigated for different seasons. The parameters affecting the system performance were described, and the annual overall efficiency of the SAPH application was obtained for the specified operating conditions. For the given conditions, the system yields that 20.8% of the annual energy needed for cooking process can be met by solar energy.

CHAPTER 7

CONCLUSIONS AND RECOMMENDATIONS

In this dissertation, an experimental methodology for designing a SAPH system for cooking application using parabolic trough collector without thermal storage was performed, and a comprehensive system modeling was developed. The methodology is based on the individual design of different components and subsequent integration of the components into the whole system. The system was tested and monitored with a number of experiments under cloudless sky conditions in Gaziantep thus the thermal performance of the system and the technical feasibility for a cooking facility at moderate temperature were analyzed. Furthermore, the system analysis was carried out by complex models of each component which was integrated into the system whose behavior is simulated to emulate the real-time operation. The consistency of the results obtained showed that the proposed methodology can be extended appropriately to large-scale SAPH system design.

The following conclusions are drawn from the theoretical and experimental studies:

- The optical loss is the most variable and effective parameter on the collector efficiency relative to the thermal loss.
- While the geometric and the cosine losses fluctuate during the daylight hours due to incidence angle, the variation for the remaining optical parameters exhibits almost stable character.
- Variation in the radiative properties of the optical materials with incidence angle can be regarded as insignificant for values lower than 20 degrees.
- Annulus condition of the receiver has considerable effect on the thermal efficiency. Vacuuming the annulus is the best choice for reducing the heat

loss however the maintenance of the receiver can be problematic. Thus use of a less-conducting fluid drops the heat loss through the annulus space by convection.

- Increase in mass flowrate requires much pumping work thus the optimal mass flowrate is needed to keep it minimally for the sake of raising the thermal efficiency of PTSC.
- The type of HTF used in PTSC has almost insignificant effect on the enhancement of the thermal efficiency.
- Increase in wind speed is considerable effect on thermal efficiency for the air-filled receiver relative to vacuum. Its effect decreases the thermal efficiency incrementally after the bulk temperature of 150°C.
- Although each CP design possesses pros and cons in its own side, selection of the design should be made in terms of cooking load and time that are to be met for a specified system capacity.
- The heat flux for onset of nucleate boiling can be accounted as the minimum energy to keep the central region of the mixture (water-wheat) at boiling temperature for complete gelatinization. Thus optimum mass flowrate of the HTF should be designated regarding this energy that is required to boil the mixture in nucleate region. Otherwise, boiling losses will be much higher.
- It is analyzed that the most important factors for the system performance are the HTF characteristics (technical specifications), collector area, thermal efficiency of the collector selected, operating temperatures and flowrates, heat transfer areas of the heat-exchange devices, overall heat loss, capacity of the auxiliary heater, and load profile of the process heat application. All these factors can degrade the performance if necessary considerations are not to be executed properly in the design stage of the SAPH.
- Collector area should be sized according to a nominal value of beam radiation that is to be identified averagely for a period of time rather than peak values taken in summer season. This justification will minimize the capacity of the auxiliary heater. However, this procedure does not give optimum size for system components as long as a definite optimization method is not applied.
- Heat transfer area of the BPHE should be selected properly to meet the thermal load of the process heat, and thus the heat transfer area of the IHHE

must match with the discharged thermal power profile at maximum level. Otherwise the utilization ratio decreases notably.

- In case of lowering the thermal load of the process, the system yields significantly lower performance characteristics.
- Minimizing the heat losses from expansion tanks, pipelines, valves, fittings and metal parts increases the overall performance of the system since the energy transfer between the components is directly affected by the overall heat loss generated from the system.
- The annual performance of the SAPH system was obtained as 20.8% under the specified conditions given in Chapter 6. This efficiency can be improved by applying different process layouts and utilizing the waste energy properly.
- The overall system efficiency can be improved also by selecting a high performance PTSC having a vacuumed receiver tube.

The following recommendations should be drawn for further research in this scope:

- Optical and thermal models of the PTSC can be improved by developing a more detailed three dimensional optical and thermal models for the generalization of the governing equation to obtain more accurate results.
- Thermal model of the IHHE was developed using time-average experimental data during boiling process. Results show that steady-state analysis is sufficient reasonably to design a CP. However, a new model could be developed for transient conditions to predict heat and mass fluxes within the CP, and pressure and temperature distribution for the inner region of the food compartment.
- In the light of the developed theoretical model for the IHHE, making a parametric model will describe the effective parameters to be able to increase the thermal performance. For further study, experimental studies should be performed to analyze the cooker based on Finite Element Method (FEM).
- Modeling of the boiling of whole wheat grains is to be studied to image moisture distributions in the grains for optimizing the cooking time for both conserving of food quality and energy consumption.

- Optimum size of the BPHE is to be calculated using the methodology proposed for maximizing the solar fraction and the annual system efficiency.
- Alternative and different combinations of the SAPH application should be studied for maximizing the annual solar fraction and the system efficiency. For example; the system with TES tank should be included in future work extending the model used for TET.
- Annual efficiency of the system can be analyzed when a different PTSC is used.
- Annual efficiency of the system may be analyzed using the radiation data of the distinct regions in Turkey to compare the results.
- Operation parameters of the system can be optimized by thermo-economic analysis using exergetic method for projecting an economic assessment of payback period.
- The theoretical system analysis proposed in this thesis could be extended to large-scale industrial process heat applications for preliminary system analysis.

REFERENCES

- [1]. IEO2013: U.S. Energy Information Administration, International Energy Outlook. (2013). DOE/EIA-0484. Available at: <http://www.eia.gov/>. Accessed 15.11.2014.
- [2]. IEA Statistics: Renewables information (2012). IEA/OECD. Available at: <http://www.iea.org/>. Accessed 15.11.2014.
- [3]. Vannoni C., Battisti R., Drigo S. (2008). Potential for Solar Heat in Industrial Processes. IEA SHC Task 33 and SolarPACES Task IV. Ciemat.
- [4]. Mauthner F., Weiss W. (2014). Solar Heat Worldwide: Markets and Contribution to the Energy Supply 2012. IEA-SHC.
- [5]. Kutscher CF., Davenport RL., Dougherty DA., Gee RC., Masterson PM., May EK. (1982). Design approaches for solar industrial process heat systems. Technical Report No. SERI/TR-253-1356.
- [6]. Schweiger H., Mendes JF., Schwenk C., Hennecke K., Barquero CG., Sarvisé AM., Carvalho MJ., (2001). POSHIP: The Potential of Solar Heat for Industrial Processes, Final Report of Project No. NNE5-1999-0308.
- [7]. Cottret N., Menichetti E. (2011). Solar Heat for Industrial Processes (SHIP): State of the art in the Mediterranean region.
- [8]. IEA SHC Task 49: Solar Heat Integration in Industrial Processes. Available at: <http://ship-plants.info/>. Accessed 15.11.2014.
- [9]. Werner S., Constantinescu N. (2006). ECOHEATCOOL Work package 1: The European heat market. Euroheat & Power.
- [10]. Kalogirou S. (2003). The potential of solar industrial process heat applications, *Applied Energy*, **76**, 337–361.
- [11]. Lauterbach C., Schmitt B., Jordan U., Vajen K. (2012). The potential of solar heat for industrial processes in Germany, *Renewable and Sustainable Energy Reviews*, **16**, 5121–5130.

- [12]. Silva R., Berenguel M., Pérez M., Fernández-García A. (2014). Thermo-economic design optimization of parabolic trough solar plants for industrial process heat applications with memetic algorithms, *Applied Energy*, **113**, 603–614.
- [13]. Weiss W., Rommel M. (2008). Process heat collectors: IEA SHC Task 33 and SolarPACES Task IV: Solar Heat for Industrial Processes. AEE INTEC.
- [14]. Schweiger H., Mendes JF., Benz N., Hennecke K., Prieto G., Cusi M., Gonçalves H. (2000). The potential of solar heat in industrial processes. A state of the art review for Spain and Portugal. In: Proceedings of EuroSun.
- [15]. Silkroad Development Agency. Available at: <http://www.ika.org.tr/>. Accessed 15.11.2014.
- [16]. Bayram M. (2005). Modelling of cooking of wheat to produce bulgur, *Journal of Food Engineering*, **71**, 179–186.
- [17]. Makarna, Bulgur, Bakliyat ve Bitkisel Yağ Tanıtım Grubu. Available at: <http://www.mbtg.org.tr/>. Accessed 15.11.2014.
- [18]. Yılmaz IH., Söylemez MS., Hayta H., Yumrutaş R. (2014). A Process Heat Application Using Parabolic Trough Collector. In: International Congress on Energy Efficiency and Energy Related Materials (ENEFM2013), *Springer Proceedings in Physics*, **155**, 137–141.
- [19]. Kreith F., Davenport R., Feustel J. (1983). Status review and prospects for solar industrial process heat (SIPH), *Journal of Solar Energy Engineering*, **105**, 385–400.
- [20]. Thomas A. (1992). Operation and performance of the solar steam generation system installed at the government silk factory, Mysore, *Energy Conversion and Management*, **3**, 191–196.
- [21]. Köhne R., Oertel K., Zunft S. (1996). Investigation of control and simulation of solar process heat plants using a flexible test facility, *Solar Energy*, **56**, 169–182.
- [22]. Nagaraju J., Garud SS., Kumar KA., Rao MR. (1999). 1 MW_{th} Industrial solar hot water system and its performance, *Solar Energy*, **66**, 491–497.
- [23]. Eskin N. (2000). Performance analysis of a solar process heat system, *Energy Conversion and Management*, **11**, 1141–1154.

- [24]. Karagiorgas M., Botzios A., Tsoutsos T. (2001). Industrial solar thermal applications in Greece: Economic evaluation, quality requirements and case studies, *Renewable and Sustainable Energy Reviews*, **5**, 157–173.
- [25]. Bokhoven TP., Van Dam J., Kratz P. (2001). Recent experience with large solar thermal systems in The Netherlands, *Solar Energy*, **71**, 347–352.
- [26]. Krüger D, Lichtenthäler N, Dersch J, Schenk H, Hennecke K, Anthrakidis A, Rusack M, Lokurlu A, Saidi K, Walder M, Fischer S, Wirth HP. (2011). Solar steam supply: Initial operation of a plant. In: ISES Solar World Congress 2011, Kassel.
- [27]. Abdel-Dayem AM. (2011). Numerical-simulation and experimental-validation of the largest Egyptian solar process-heat system, *Journal of Renewable and Sustainable Energy*, **4**, 043102–17.
- [28]. Boutaghriout B., Bouaka, A., Hamouda C., Smadi H., Malek A. (2013). Investigation on the use of solar thermal energy in the agro food industry in Algeria. In: Renewable and Sustainable Energy Conference (IRSEC), IEEE.
- [29]. Pietruschka D., Fedrizzi R., Orioli F., Söll R., Stauss R. (2012). Demonstration of Three Large Scale Solar Process Heat Applications with Different Solar Thermal Collector Technologies, *Energy Procedia*, **30**, 755–764.
- [30]. Cotrado M., Dalibard A., Söll R., Pietruschka D. (2014). Design, Control and First Monitoring Data of a Large Scale Solar Plant at the Meat Factory Berger, Austria, *Energy Procedia*, **48**, 1144–1151.
- [31]. Vittoriosi A., Fedrizzi R., Brock R., Orioli F., Orioli V., Pietruschka D. (2014). Monitoring of a MW Class Solar Field Set up in a Brick Manufacturing Process, *Energy Procedia*, **48**, 1217–1225.
- [32]. Frank E., Marty H., Hangartner L., Minder S. (2014). Evaluation of Measurements on Parabolic Trough Collector Fields for Process Heat Integration in Swiss Dairies, *Energy Procedia*, **57**, 2743–2751.
- [33]. Lauterbach C., Schmitt B., Vajen K. (2014). System analysis of a low-temperature solar process heat system, *Solar Energy*, **101**, 117–130.
- [34]. Iglauer O., Zahler C. (2014). A New Solar Combined Heat and Power System for Sustainable Automobile Manufacturing, *Energy Procedia*, **48**, 1181–1187.

- [35]. Frein A., Calderoni M., Motta M. (2014). Solar Thermal Plant Integration into an Industrial Process, *Energy Procedia*, **48**, 1152–1163.
- [36]. Hafner B., Stoppok O., Zahler C., Berger M., Hennecke K., Krüger D. (2014). Development of an Integrated Solar-fossil Powered Steam Generation System for Industrial Applications, *Energy Procedia*, **48**, 1164–1172.
- [37]. Mauthner F., Hubmann M., Brunner C., Fink C. (2014). Manufacture of Malt and Beer with Low Temperature Solar Process Heat, *Energy Procedia*, **48**, 1188–1193.
- [38]. Silva R., Cabrera FJ., Pérez-García M. (2014). Process Heat Generation with Parabolic Trough Collectors for a Vegetables Preservation Industry in Southern Spain, *Energy Procedia*, **48**, 1210–1216.
- [39]. Eldean MAS., Soliman AM. (2015). Study of Using Solar Thermal Power for the Margarine Melting Heat Process, *Journal of Solar Energy Engineering*, **137**, 021004–1/13.
- [40]. Gordon JM., Rabl A. (1982). Design, analysis and optimization of solar industrial process heat plants without storage, *Solar Energy*, **28**, 519–530.
- [41]. Collares-Pereira M., Gordon JM., Rabl A., Zarmi Y. (1984). Design and optimization of solar industrial hot water systems with storage, *Solar Energy*, **32**, 121–133.
- [42]. Aidonis A., Drosou V., Mueller T., Staudacher L., Fernandez-Llebarez F., Oikonomou A., Spencer S. (2005). PROCESOL II - Solar thermal plants in industrial processes: Design and Maintenance Guidelines. ALTENER 4.1030/Z/02-084/2002.
- [43]. Kulkarni GN., Kedare SB., Bandyopadhyay S. (2008). Design of solar thermal systems utilizing pressurized hot water storage for industrial applications, *Solar Energy*, **82**, 686–699.
- [44]. Pavlović TM., Radonjić, IS., Milosavljević, DD., Pantić, LS. (2012). A review of concentrating solar power plants in the world and their potential use in Serbia, *Renewable and Sustainable Energy Reviews*, **16**, 3891–3902.
- [45]. Dudley VE., Kolb G., Sloan M., Kearney D. (1994). Test results: SEGS LS-2 solar collector. Sandia National Laboratories, SAND94-1884.
- [46]. Li M., Wang LL. (2006). Investigation of evacuated tube heated by solar trough concentrating system, *Energy Conversion and Management*, **47**, 3591–3601.

- [47]. Edenburn MW. (1976). Performance analysis of a cylindrical parabolic focusing collector and comparison with experimental results, *Solar Energy*, **18**, 437–444.
- [48]. Kalogirou S. (1996). Parabolic Trough Collector System for Low Temperature Steam Generation: Design and Performance Characteristics, *Applied Energy*, **55**, 1–19.
- [49]. Odeh SD., Morrison GL., Behnia M. (1998). Modelling of Parabolic Trough Direct Steam Generation Solar Collectors, *Solar Energy*, **62**, 395–406.
- [50]. Forristall R. (2003). Heat transfer analysis and modelling of a parabolic trough solar receiver implemented in engineering equation solver. NREL/TP–550e34169.
- [51]. Jacobson E., Ketjoy N., Nathakaranakule S., Rakwichian W. (2006). Solar Parabolic Trough Simulation and Application for a Hybrid Power Plant in Thailand, *Science Asia*, **32**, 187–199.
- [52]. Garcia-Valladares O., Velazquez N. (2009). Numerical simulation of parabolic trough solar collector: Improvement using counter flow concentric circular heat exchangers, *International Journal of Heat and Mass Transfer*, **52**, 597–609.
- [53]. Qu M., Yin H., Archer DH. (2010). Experimental and Model Based Performance Analysis of a Linear Parabolic Trough Solar Collector in a High Temperature Solar Cooling and Heating System, *Journal of Solar Energy Engineering*, **132**, 166–182.
- [54]. Padilla RV., Demirkaya G., Goswami DY., Stefanakos, E., Rahman, M. (2011). Heat transfer analysis of parabolic trough solar receiver, *Applied Energy*, **88**, 5097–5110.
- [55]. Huang W., Hu P., Chen Z. (2012). Performance simulation of a parabolic trough solar collector, *Solar Energy*, **86**, 746–755.
- [56]. Coccia G., Latini G., Sotte M. (2012). Mathematical modeling of a prototype of parabolic trough solar collector, *Journal of Renewable and Sustainable Energy*, **4**, 023110–1/15.
- [57]. Kalogirou SA. (2012). A detailed thermal model of a parabolic trough collector receiver, *Energy*, **48**, 298–306.

- [58]. Wirz M., Roesle M., Steinfeld A. (2012). Three-Dimensional Optical and Thermal Numerical Model of Solar Tubular Receivers in Parabolic Trough Concentrators, *Journal of Solar Energy Engineering*, **134**, 041012–1/9.
- [59]. Silva R., Perez M., Fernández-García A. (2013). Modeling and co-simulation of a parabolic trough solar plant for industrial process heat, *Applied Energy*, **106**, 287–300.
- [60]. You C., Zhang W., Zhiqiang Y. (2013). Modeling of fluid flow and heat transfer in a trough solar collector, *Applied Thermal Engineering*, **54**, 247–254.
- [61]. Dongqiang L., Qiang L., Zhifeng W., Jian L., Jianbin L. (2013). An experimental study of thermal characterization of parabolic trough receivers, *Energy Conversion and Management*, **69**, 107–15.
- [62]. Hachicha AA., Rodríguez I., Capdevila R., Oliva A. (2013). Heat transfer analysis and numerical simulation of a parabolic trough solar collector, *Applied Energy*, **111**, 581–592.
- [63]. Ouagueda M., Khellaf A., Loukarfi L. (2013). Estimation of the temperature, heat gain and heat loss by solar parabolic trough collector under Algerian climate using different thermal oils, *Energy Conversion and Management*, **75**, 191–201.
- [64]. Marif Y., Benmoussa H., Bouguettaia H., Belhadj MM., Zerrouki M. (2014). Numerical simulation of solar parabolic trough collector performance in the Algeria Saharan region, *Energy Conversion and Management*, **85**, 521–529.
- [65]. Mokheimer EMA, Dabwan YN., Habib MA., Said SAM., Al-Sulaiman FA. (2014). Techno-economic performance analysis of parabolic trough collector in Dhahran, Saudi Arabia, *Energy Conversion and Management*, **86**, 622–633.
- [66]. Yılmaz İH., Söylemez MS. (2014). Thermo-mathematical modeling of parabolic trough collector, *Energy Conversion and Management*, **88**, 768–784.
- [67]. Technical specifications of Smirro300 provided by the manufacturer, Solera Sunpower GmbH. Available at: <http://www.smirro.de/>. Accessed 15.11.2014.
- [68]. Touloukian YS, DeWitt DP. (1970/1972). Thermophysical properties of matter: Thermal radiative properties-metallic elements and alloys/Thermal radiative properties-nonmetallic solids. Vol. 7/Vol. 8. New York: IFI/Plenum.

- [69]. Technical data for stainless steel tubes with selective coating. Available at: <http://www.energie-solaire.com>. Accessed 15.11.2014.
- [70]. The Earth's energy budget. Available at: <http://www.nasa.gov/>. Accessed 15.11.2014.
- [71]. Goswami DY., Kreith F., Kreider JF., Kreith F. (2000). Principles of Solar Engineering. 2nd edition. Philadelphia, PA: Taylor & Francis.
- [72]. Duffie JA., Beckman WA. (2005). Solar engineering of thermal processes. 3rd edition. New York: John Wiley & Sons.
- [73]. Stine WB., Harrigan RW. (1985). Solar Energy Fundamentals and Design: With Computer Applications. New York : John Wiley & Sons.
- [74]. Spisz EW., Weigund AJ., Bowmun RL., Juck JR. (1969). Solar Absorptances and Spectral Reflectances of 12 Metals for Temperatures Ranging from 300 to 500 K. NASA TN D-5353.
- [75]. Solar reflectance of MIRO-SUN. Available at: <http://www.alanod-solar.com/>. Accessed 15.11.2014.
- [76]. Technical datasheet of DURAN Glass–Tubing, Capillary and Rod of Borosilicate Glass 3.3. Available at: <http://www.duran-group.com/>. Accessed 15.11.2014.
- [77]. Guven HM., Bannerot RB. (1984). Optical and thermal analysis of parabolic trough solar collectors for technically less developed countries Technical report–1. USAID Project Grant No. 386–0465.
- [78]. Guven HM., Bannerot RB. (1985). Derivation of universal error parameters for comprehensive optical analysis of parabolic troughs. In: Proceedings of the ASME-ASES Solar Energy Conference, Knoxville, USA.
- [79]. Arasu AV., Sornakumar T. (2007). Design, manufacture and testing of fiberglass reinforced parabola trough for parabolic trough solar collectors, *Solar Energy*, **81**, 1273–1279.
- [80]. Rabl A. (1985). Active Solar Collectors and Their Applications. New York/Oxford: Oxford University Press.
- [81]. Cengel YA, Ghajar AJ. (2011). Heat transfer and mass transfer: Fundamentals & Applications. New York: McGraw-Hill.
- [82]. Product Information: Renolin Therm 320 Heat Transfer Fluid. Available at: <http://www.lukoilmarine.com/>. Accessed 15.11.2014.

- [83]. Sandall OC., Hanna OT., Mazet PR. (1980). A New Theoretical Formula for Turbulent Heat and Mass Transfer with Gases or Liquids in Tube Flow, *The Canadian Journal of Chemical Engineering*, **58**, 443–447.
- [84]. Davis JR. (2000). Alloy Digest Sourcebook: Stainless Steels. ASM International.
- [85]. Harnett JP., Irvine TF. (1971). Advances in Heat Transfer. Vol. 7. New York: Academic Press.
- [86]. Ratzel A., Hickox C., Gartling D. (1979). Techniques for reducing thermal conduction and natural convection heat losses in annular receiver geometries, *Journal of Heat Transfer*, **101** (1), 108–113.
- [87]. Song S., Yovanovich M. (1987). Correlation of thermal accommodation coefficient for engineering surfaces. In: Proceedings of the ASME National Heat Transfer Conference, New York.
- [88]. Kuehn TH., Goldstein RJ. (1976). Correlating equations for natural convection heat transfer between horizontal circular cylinders, *International Journal of Heat and Mass Transfer*, **19**, 1127–1134.
- [89]. Rohsenow WM, Hartnett JP, Cho YI. (1998). Handbook of Heat Transfer. 3rd edition. New York: McGraw-Hill.
- [90]. Naeeni N., Yaghoubi M. (2007). Analysis of wind flow around a parabolic collector (2) heat transfer from receiver tube, *Renewable Energy*, **32**, 1259–1272.
- [91]. Harnett JP., Irvine TF. (1975). Advances in Heat Transfer. Vol. 11. New York: Academic Press.
- [92]. Oppenheim AK. (1956). Radiation Analysis by the Network Method, *Transactions of the ASME*, **78**, 725–735.
- [93]. Swinbank WC. (1963). Long-wave radiation from clear skies, *Quarterly Journal of the Royal Meteorological Society*, **89**, 339–348.
- [94]. Thermophysical database of EES, V9.433 Academic Commercial.
- [95]. Technical datasheet of İzocam Industrial Blanket. Available at: <http://www.izocam.com.tr/>. Accessed 15.11.2014.
- [96]. Popiel CO., Wojtkowiak J. (1998). Simple Formulas for Thermophysical Properties of Liquid Water for Heat Transfer Calculations (from 0°C to 150°C), *Heat Transfer Engineering*, **19**, 87–101.

- [97]. Gnielinski V. (1976). New equations for heat and mass transfer in turbulent pipe and channel flow, *International Chemical Engineering*, **16**, 359–68.
- [98]. Churchill SW., Chu HHS. (1975). Correlating Equations for Laminar and Turbulent Free Convection from a Horizontal Cylinder, *International Journal of Heat Mass Transfer*, **18**, 1049–1053.
- [99]. Churchill SW., Chu HHS. (1975). Correlating Equations for Laminar and Turbulent Free Convection from a Vertical Plate, *International Journal of Heat Mass Transfer*, **18**, 1323–1329.
- [100]. Stapley AGF., Fryer PJ., Gladden LF. (1998). Diffusion and reaction in whole wheat grains during boiling, *AIChE Journal*, **44**, 1777–1793.
- [101]. Watanabe H., Fukuoka M., Tomiya A., Mihori T. (2001). A new non-Fickian diffusion model for water migration in starchy food during cooking, *Journal of Food Engineering*, **49**, 1–6.
- [102]. Rocca-Poliméni R., Flick D., Vasseur. J. (2011). A model of heat and mass transfer inside a pressure cooker, *Journal of Food Engineering*, **107**, 393–404.
- [103]. Koca AF., Anıl M. (1996). Farklı Buğday Çeşitleri ve Pişirme Yöntemlerinin Bulgur Kalitesine Etkisi, *Gıda*, **21**, 369–374.
- [104]. Bakshi AS., Singh RP. (1980). Kinetics of water diffusion and starch gelatinization during rice parboiling, *Journal of Food Science*, **45**, 1387–1392.
- [105]. Lund DB., Wirakartakusumah M. (1984). *Engineering and Food*. Vol. 1. London, UK: Elsevier.
- [106]. Turhan M., Gunasekaran S. (2002). Kinetics of in situ and in vitro gelatinization of hard and soft wheat starches during cooking in water, *Journal of Food Engineering*, **52**, 1–7.
- [107]. Bruce DM., Giner SA. (1993). Mathematical Modeling of Grain Drying in Counter-flow Beds: Investigation of Crossover of Air and Grain Temperatures, *Journal of Agricultural Engineering Research*, **2**, 143–161.
- [108]. Mullin T. (2011). Experimental studies of transition to turbulence in a pipe, *Annual Review of Fluid Mechanics*, **43**, 1–24
- [109]. Dean WR. (1927). Note on the motion of fluid in a curved pipe, *Philosophical Magazine*, **4**, 208–223.

- [110]. Dean WR. (1928). The stream-line motion of fluid in a curved pipe, *Philosophical Magazine*, **5**, 673–695
- [111]. Srinivasan SS., Nandapurkar FA. (1970). Holland Friction factor for coils, *Transactions of the Institution of Chemical Engineer*, **48**, 156–161.
- [112]. Manlapaz R., Churchill SW. (1981). Fully developed laminar convection from a helical coil, *Chemical Engineering Communication*, **9**, 185–200.
- [113]. Hogg GW. (1968). The Effect of Secondary Flow on Point Heat Transfer Coefficients for Turbulent Flow inside Curved Tubes. Moscow, ID: Ph.D. thesis, University of Idaho.
- [114]. Pratt NH. (1947). The heat transfer in a reaction tank cooled by means of a coil, *Transactions of the Institution of Chemical Engineers*, **25**, 163–180.
- [115]. Sathyabhama A., Hegde RN. (2010). Prediction of Nucleate Pool Boiling Heat Transfer Coefficient, *Thermal Science*, **14**, 353–364.
- [116]. Cornwell K., Houston SD. (1994). Nucleate pool boiling on horizontal tubes: A convection-based correlation, *International Journal of Heat and Mass Transfer*, **37**, 303–309.
- [117]. Gerstmann J. Griffith P. (1967). Laminar Film Condensation on the Underside of Horizontal and Inclined Surfaces, *International Journal Heat Mass Transfer*, **10**, 567–580.
- [118]. Minkowycz WJ., Sparrow EM. (1966). Condensation heat transfer in the presence of noncondensables, interfacial resistance, superheating, variable properties, and diffusion, *International Journal of Heat and Mass Transfer*, **9**, 1125–1144.
- [119]. Chin Y., Ormiston S., Soliman H. (1994). Numerical solution of the complete two phase model for laminar film condensation with a non-condensable gas. In: Proceedings of the tenth International Heat and Mass Transfer Conference, Brighton, UK.
- [120]. Fujii T., Imura H. (1972). Natural Convection Heat Transfer from a Plate with Arbitrary Inclination, *International Journal of Heat Mass Transfer*, **15**, 755–764.
- [121]. Marrero TR., Mason EA. (1972). Gaseous Diffusion Coefficients, *Journal of Physic*, **1**, 113–118.
- [122]. Technical datasheet of B10TH. Available at <http://www.swep.net/>. Accessed 15.11.2014.

- [123]. Kakac S, Liu H. (2002). Heat Exchangers Selection, Rating and Thermal Design. 2nd edition. Florida: CRC Press.
- [124]. Palm B., Claesson J. (2006). Plate Heat Exchangers: Calculation Methods for Single and Two-Phase Flow, *Heat Transfer Engineering*, **27**, 88–98.
- [125]. Kays WM, London AL. (1984). Compact Heat Exchangers. 3rd edition. New York: McGraw-Hill.
- [126]. Heavner RL., Kumar H., Wanniarachchi AS. (1993). Performance of an Industrial Heat Exchanger: Effect of Chevron Angle. In: AIChE Symposium Series, New York.
- [127]. Muley A. Manglik RM. (1999). Experimental Study of Turbulent Flow Heat Transfer and Pressure Drop in a Plate Heat Exchanger with Chevron Plates, *Journal of Heat Transfer*, **121**, 110–117.
- [128]. Wanniarachchi AS., Ratnam U., Tilton BE., Dutta-Roy K. (1995). Approximate Correlations for Chevron-Type Plate Heat Exchangers. In: 30th National Heat Transfer Conference. New York: ASME.
- [129]. Devore K. (2014). Thermal Expansion Tank Design and Operation, *Process Heating Magazine*, **21**, 14–16.
- [130]. Kumana J., Kothari S. (1982). Predict Storage-Tank Heat Transfer Precisely, *Chemical Engineer*, **89**, 127–132.
- [131]. Zukauskas A. 1987. Advances in Heat Transfer. Vol. 18. Orlando, Florida: Academic Press.
- [132]. Van der Hegge ZEG. (1957). Modified correlation formulae for the heat transfer by natural and by forced convection from horizontal cylinders, *Applied Scientific Research Section A*, **6**, 129–140.
- [133]. Technical datasheet of İzocam Glass Wool Prefabricated Pipe. Available at: <http://www.izocam.com.tr/>. Accessed 15.11.2014.
- [134]. Wagner M., Blair N., Dobos A. (2010). Detailed Physical Trough Model for NREL's Solar Advisor Model. National Renewable Energy Laboratory (NREL): NREL/CP-5500-49368.
- [135]. Technical properties of YKF-1" Internal Eccentric Gear Pump. Available at: <http://www.yildizpompa.com.tr/>. Accessed 15.11.2014.
- [136]. Technical datasheet of Pt100. Available at: <http://www.ordel.com.tr/>. Accessed 15.11.2014.

- [137]. Pakkens pressure gauge datasheet. Available at: <http://www.pakkens.net/>. Accessed 15.11.2014.
- [138]. Technical datasheet of TFM2100. Available at: <http://www.aktek.com.tr/>. Accessed 15.11.2014.
- [139]. Optimass 6000 technical datasheet. Available at: <http://www.krohne.com/>. Accessed 15.11.2014.
- [140]. Technical datasheet of CMP11. Available at: <http://www.kippzonen.com/>. Accessed 15.11.2014.
- [141]. USB-2416 User's Guide. Available at: <http://www.mccdaq.com/>. Accessed 15.11.2014.
- [142]. USB-TEMP User's Guide. Available at: <http://www.mccdaq.com/>. Accessed 15.11.2014.
- [143]. ENDA ECSC Configurable Signal Converter. Available at: <http://www.enda.com.tr/>. Accessed 15.11.2014.
- [144]. Dinçer İ, Rosen M. (2011). Thermal Energy Storage: Systems and Applications. 2nd edition. Chichester: John Wiley & Sons.
- [145]. Münzing K. (1991). DSC studies of starch in cereal and cereal products, *Thermochimica Acta*, **193**, 441–448.
- [146]. Specifications of Colorflex. Available at: <http://www.hunterlab.com/>. Accessed 15.11.2014.
- [147]. AOAC. Association of Official Analytical Chemists. (1990). Official methods of analysis of the association of official analytical chemists. 15th edition. Washington, DC.
- [148]. Kumaresan G., Sridhar R., Velraj R. (2012). Performance studies of a solar parabolic trough collector with a thermal energy storage system, *Energy*, **47**, 395–402.

APPENDIX

Appendix A: Thermophysical Properties of Heat Transfer Fluid (Renolin therm 320)

$$\text{Density (kg/m}^3\text{): } \rho = 880 - 0.6495T(^{\circ}\text{C}) \quad (\text{A.1})$$

$$\text{Specific heat capacity (J/kg}\cdot^{\circ}\text{C): } c_p = 1864 + 4.289T(^{\circ}\text{C}) \quad (\text{A.2})$$

$$\text{Thermal conductivity (W/m}\cdot^{\circ}\text{C): } k = 0.1344 - 0.00007235T(^{\circ}\text{C}) \quad (\text{A.3})$$

$$\text{Kinematic viscosity (mm}^2\text{/s): } \nu = \exp\left(\frac{920}{T(^{\circ}\text{C})+102.83} - 2.665\right) \quad (\text{A.4})$$

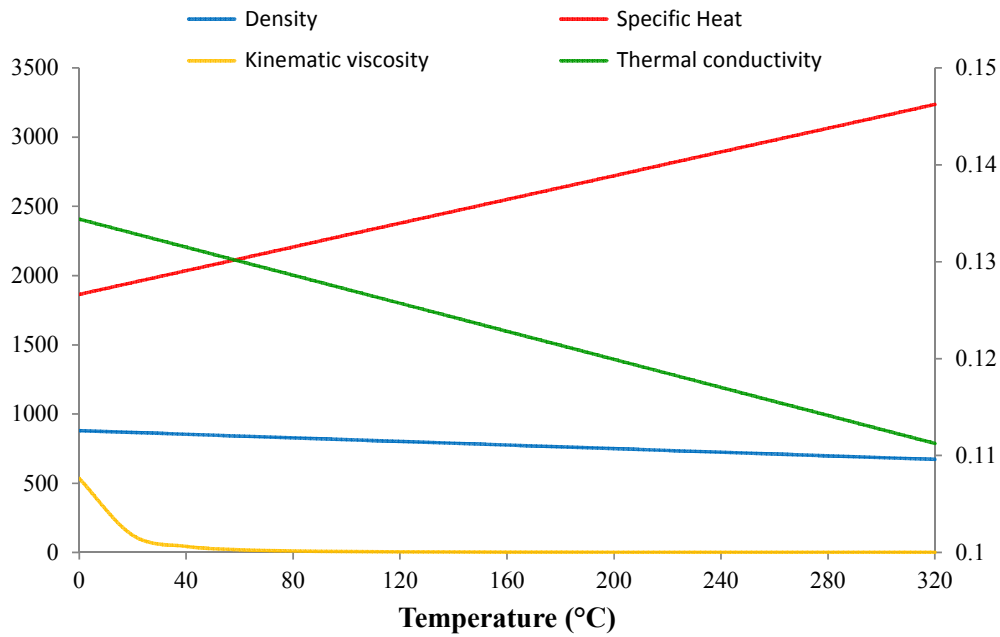


Figure A.1. Variation of thermophysical properties with temperature. Adapted from [82].

Appendix B: Thermophysical Properties of Air

Molecular Weight (kg/mol): 28.966

Gas Constant R (kJ/kg·K): 0.287040

Critical Temperature T_c (K): 132.6

Critical Pressure P_c (MPa): 3.77

The specific heat, dynamic viscosity, and thermal conductivity are treated only the functions of temperature in Kelvin. To obtain the density of a gas, the perfect gas law may be used [89]:

$$\text{Density (kg/m}^3\text{): } \rho = \frac{P}{RT} \quad (\text{B.1})$$

$$\text{Specific heat capacity (J/kg·K): } c_p = \sum_{i=0}^N A_i T^i \quad (\text{B.2})$$

$$\text{Dynamic viscosity (kg/m·s} \times 10^{-6}\text{): } \mu = \sum_{i=0}^N B_i T^i \quad (\text{B.3})$$

$$\text{Thermal conductivity (W/m·K): } k = \sum_{i=0}^N C_i T^i \quad (\text{B.4})$$

Table B.1. Constants for equations (B.2–B.4). Adapted from [89]

i	$A_i^{(1)}$	$B_i^{(2)}$	$B_i^{(3)}$	$C_i^{(1)}$
0	1.03439	-9.8601×10^{-1}	4.8856745	-2.276501×10^{-5}
1	$-0.2848870 \times 10^{-3}$	-9.080125×10^{-2}	5.43232×10^{-2}	1.2598485×10^{-4}
2	0.7816818×10^{-6}	$-1.17625575 \times 10^{-4}$	$-2.4261775 \times 10^{-5}$	-1.481523×10^{-7}
3	$-0.4970786 \times 10^{-9}$	1.2349703×10^{-7}	7.9306×10^{-9}	$1.73550646 \times 10^{-10}$
4	$0.1077024 \times 10^{-12}$	$-5.7971299 \times 10^{-11}$	-1.10398×10^{-12}	$-1.066657 \times 10^{-13}$
5	0	0	0	$2.47663035 \times 10^{-17}$
6	0	0	0	0

⁽¹⁾ $250 \leq T < 1050\text{K}$, ⁽²⁾ $250 \leq T < 600\text{K}$, ⁽³⁾ $600 \leq T < 1050\text{K}$

Appendix C: Thermophysical Properties of Water

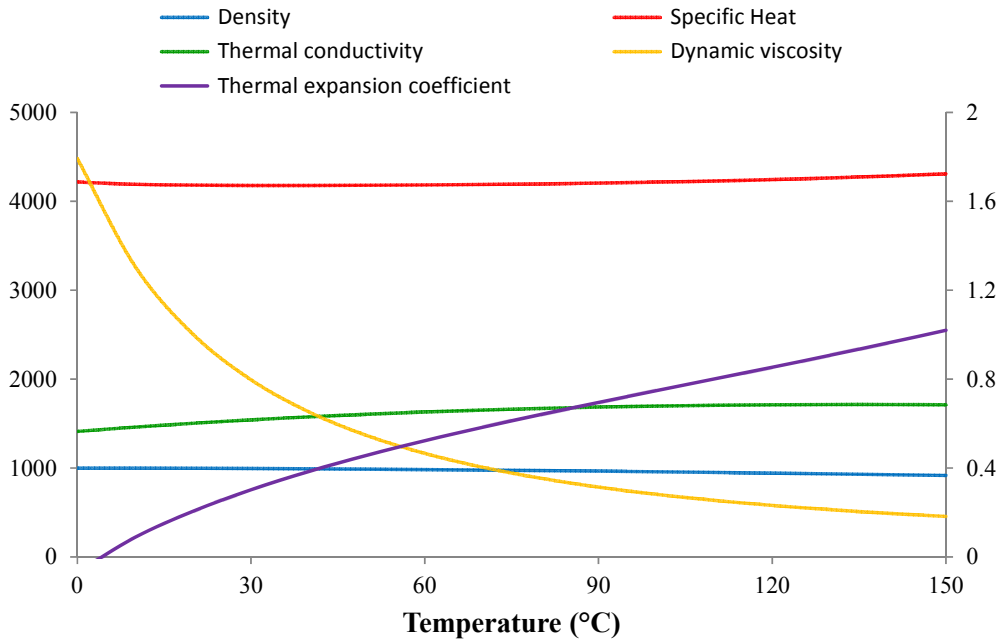


Figure C.1. Variation of thermophysical properties with temperature.

$$\text{Density (kg/m}^3\text{): } \rho = a + bT + cT^2 + dT^{2.5} + eT^3 \quad (\text{C.1})$$

$$\text{Specific heat capacity (kJ/kg}\cdot\text{°C): } c_p = a + bT + cT^{1.5} + dT^2 + eT^{2.5} \quad (\text{C.2})$$

$$\text{Thermal conductivity (W/m}\cdot\text{°C): } k = a + bT + cT^{1.5} + dT^2 + eT^{0.5} \quad (\text{C.3})$$

$$\text{Dynamic viscosity (kg/m}\cdot\text{s): } \mu = \frac{1}{a + bT + cT^2 + dT^3} \quad (\text{C.4})$$

$$\text{Thermal expansion coefficient (1/K): } \beta = a + bT + cT^{1.5} + dT^2 \quad (\text{C.5})$$

Table C.1. Constants for equations (C.1–C.5). Adapted from [96]

	ρ	c_p	k	μ	β
a	999.79684	4.2174356	0.5650285	557.82468	$-6.8785895 \times 10^{-5}$
b	0.068317355	-0.0056181625	0.0026363895	19.408782	2.1687942×10^{-5}
c	-0.010740248	0.0012992528	-0.00012516934	0.1360459	$-2.1236686 \times 10^{-6}$
d	0.00082140905	-0.00011535353	$-1.5154918 \times 10^{-6}$	$-3.1160832 \times 10^{-4}$	7.7200882×10^{-8}
e	$-2.3030988 \times 10^{-5}$	4.14964×10^{-6}	-0.0009412945	0	0

Appendix D: Technical Specifications of Pipe Materials

$$\text{Density (kg/m}^3\text{): } \rho = \sum_{i=0}^N A_i T^i \quad (\text{D.1})$$

$$\text{Specific heat capacity (J/kg}\cdot\text{K): } c_p = \sum_{i=0}^N B_i T^i \quad (\text{D.2})$$

$$\text{Thermal conductivity (W/m}\cdot\text{K): } k = \sum_{i=0}^N C_i T^i \quad (\text{D.3})$$

$$\text{Linear expansion coefficient (1/K): } \alpha = \sum_{i=0}^N D_i T^i \quad (\text{D.4})$$

Table D.1. Constants for equations (D.1–D.4). Adapted from [94]^(*)

i	A_i	B_i	C_i	D_i
304/304L SS				
0	8006	461.7	14.49	0.00001431
1	-0.3580	0.5641	0.01634	1.842×10^{-8}
2	-0.0001339	-0.001508	0	-2.882×10^{-11}
3	0	2.077×10^{-6}	0	3.870×10^{-14}
316/316L SS				
0	8034	484.2	13.05	0.00001519
1	-0.3720	0.2071	0.01634	9.560×10^{-9}
2	-0.00005435	-1.942×10^{-5}	0	-2.329×10^{-11}
3	0	0	0	3.580×10^{-14}

^(*) $25 \leq T \leq 300^\circ\text{C}$

Appendix E: Technical Specifications of Insulation Materials

Table E.1. Physical properties stone wool. Adapted from [95].

Properties	Description							
Density, kg/m ³	80							
Thickness, mm	50							
Facing	Stitched with galvanized wire							
Specific heat, kJ/kg°C	0.84							
Thermal conductivity	°C	50	100	150	200	250	300	350
W/m°C	0.038	0.047	0.058	0.069	0.083	0.098	0.115	

Table E.2. Physical properties glass wool. Adapted from [133].

Properties	Description							
Density, kg/m ³	75							
Thickness, mm	25							
Facing	Aluminum sheet cladding							
Specific heat, kJ/kg°C	0.84							
Thermal conductivity	°C	25	50	75	100	125	150	
W/m°C	0.038	0.047	0.058	0.069	0.083	0.098		

Appendix F: Flowcharts of Program Algorithms

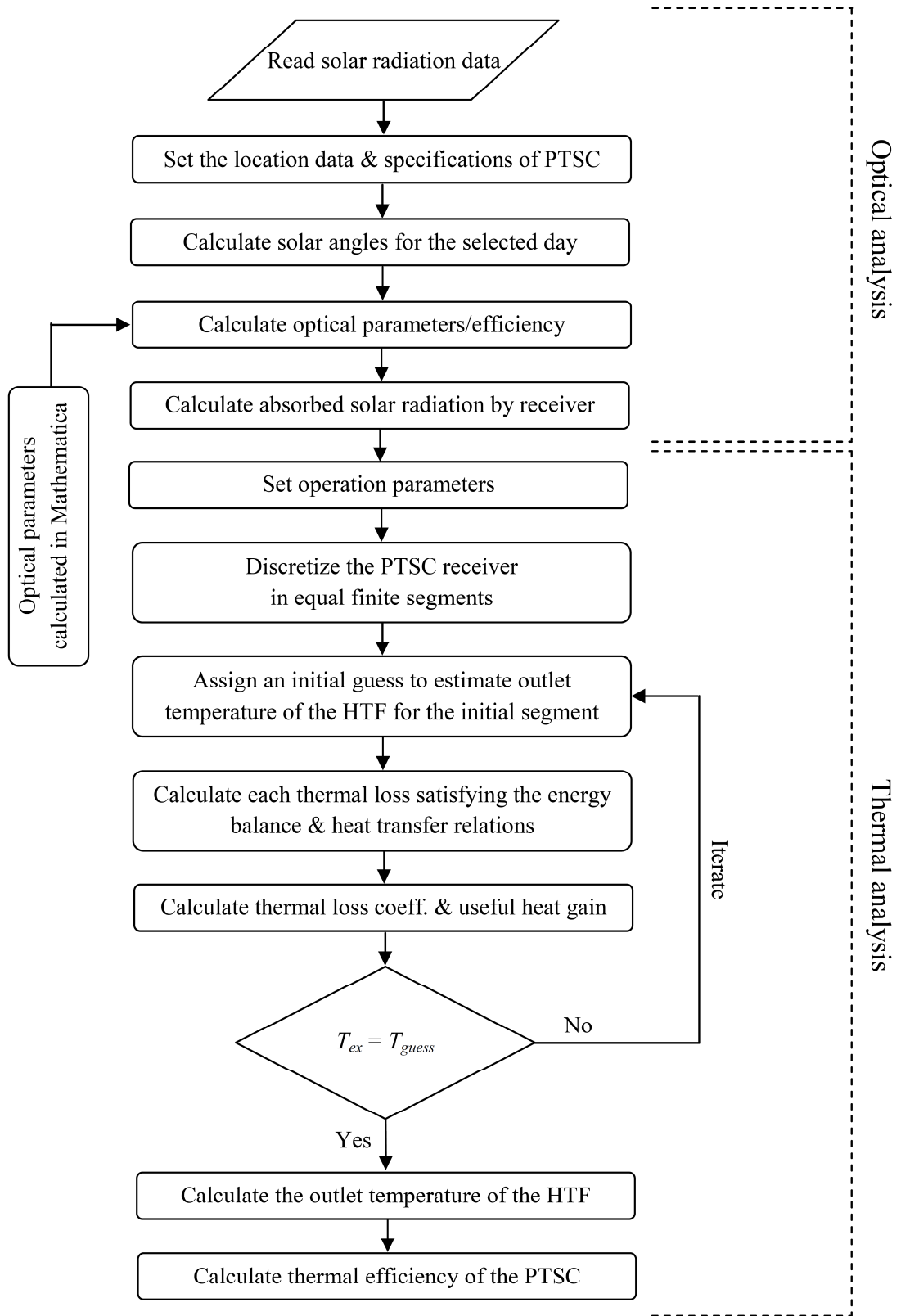


Figure F.1. Flowchart for PTSC simulation.

Appendix F: (Continued)

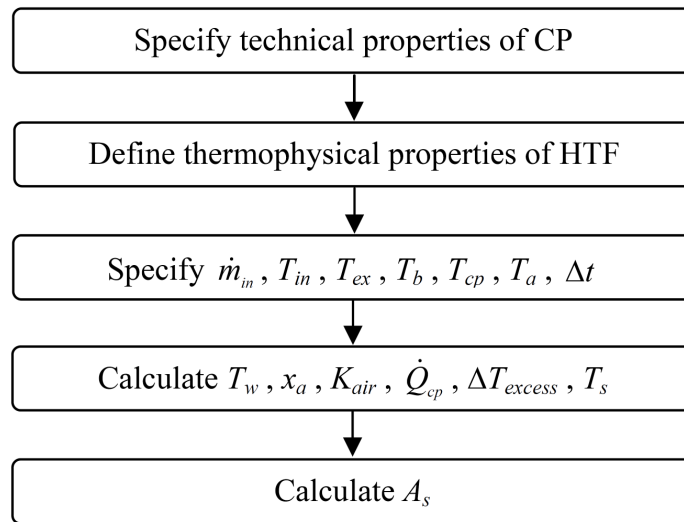


Figure F.2. Flowchart for cooking pot (IHHE).

Appendix F: (Continued)

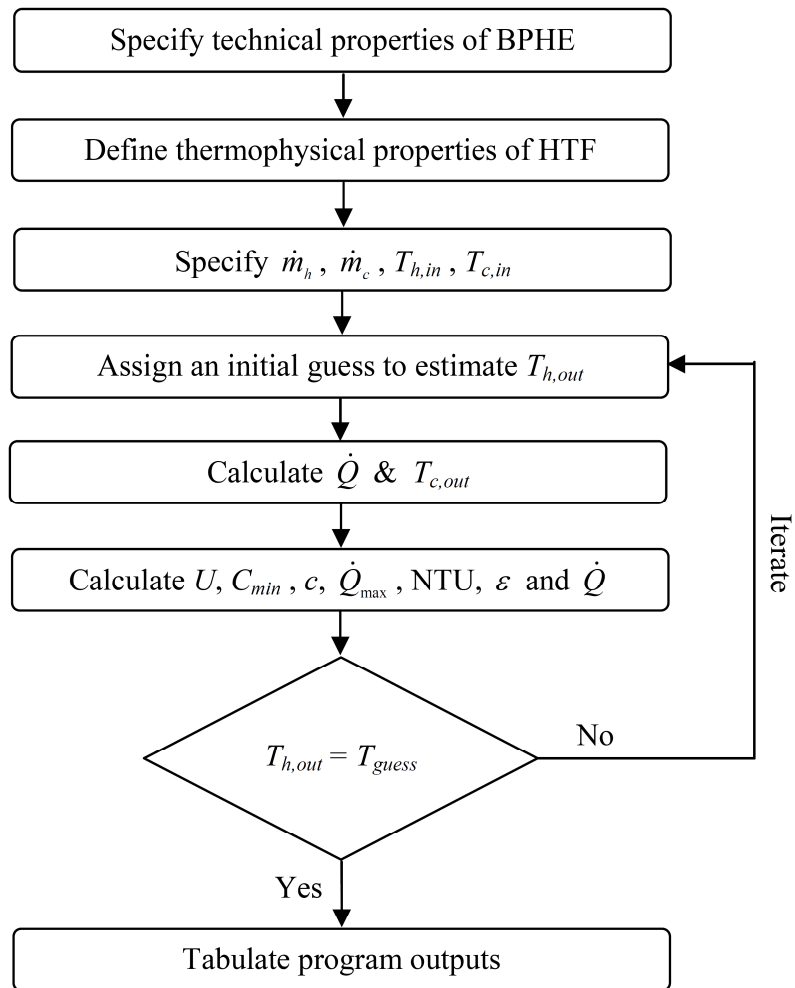


Figure F.3. Flowchart for BPHE simulation.

Appendix F: (Continued)

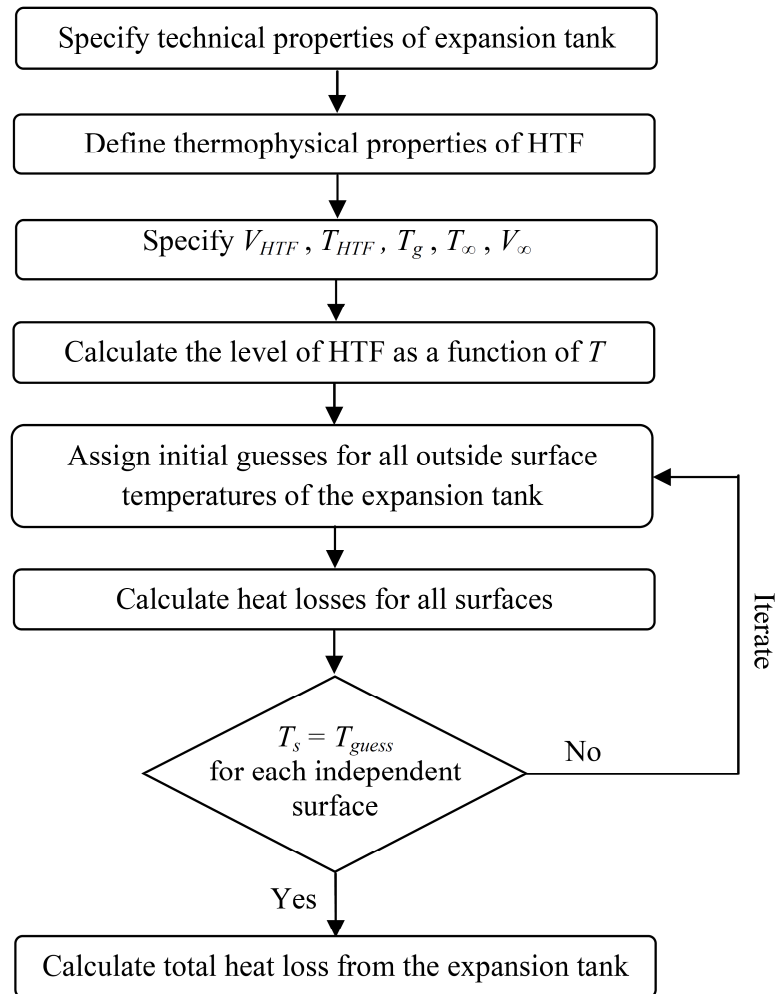


Figure F.4. Flowchart for thermal expansion tank simulation.

Appendix F: (Continued)

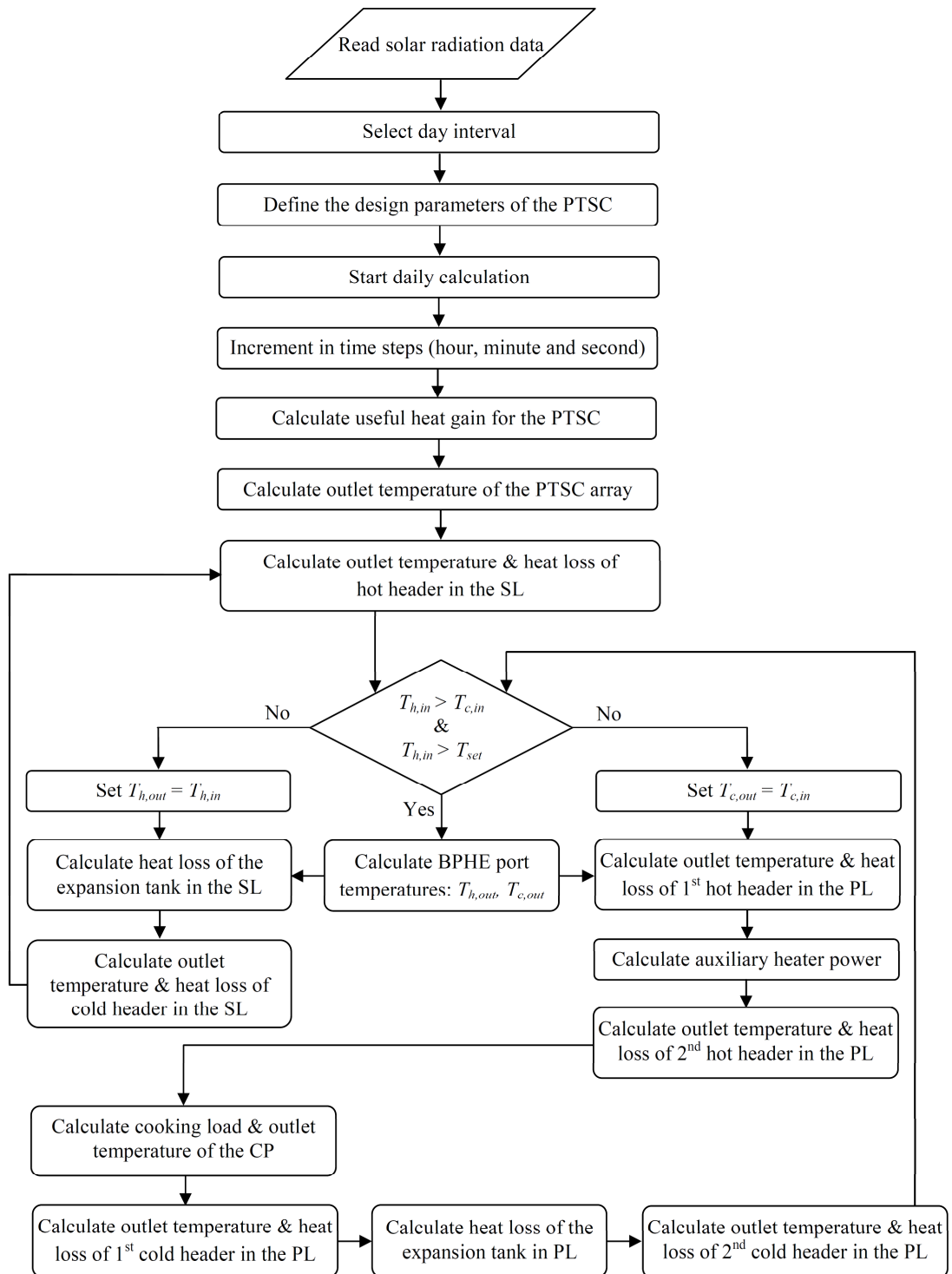


Figure F.5. Flowchart for transient simulation of SAPH application.

Appendix G: Evaporating Liquid – Basic Theory

Consider a liquid in a closed container with a moving control volume $V(t)$ that encompasses the liquid in the container. The interface height is given by $H(t)$ which is changing with time. Thus the volume of liquid at any time t is

$$V(t) = AH(t) \quad (\text{G.1})$$

where A is the cross-sectional area of the container. Consider first the isothermal quasi-steady evaporation of the water. The macroscopic mass balance over the liquid is

$$\frac{d}{dt} \int_{V(t)} \rho_L dV + \int_A \rho_L (v - w) \cdot ndA = 0 \quad (\text{G.2})$$

where $w = dH/dt$ is the velocity of the liquid gas interface and v is the velocity of the liquid. This can be expressed as

$$\frac{dM}{dt} = - \int_A \rho_l (v - w) \cdot ndA = -j_{rel} A \quad (\text{G.3})$$

where j_{rel} ($\text{kg}/\text{m}^2 \cdot \text{s}$) is the mass flux leaving the moving control volume due to evaporation, and the mass of liquid in the container at any time t is

$$M = A \frac{d(\rho_L H)}{dt} \quad (\text{G.4})$$

Since the evaporation is slow, we can assume that the concentration of water vapor in the gas phase is quasi-static (inertial effects are not important). The quasi-static concentration field in the ambient gas that constitutes the surrounding gas phase ignoring (convective effects) must satisfy

Appendix G: (Continued)

$$\frac{d^2c}{dy^2} = 0 \quad (\text{G.5})$$

Let the concentration of the water in the gas phase at the liquid surface be equal to its equilibrium concentration c_s and sufficiently far away from the interface let it be c_∞ . Then the concentration field for the water species can be found by solving Equation (G.5) to give

$$c(y) = \frac{(c_\infty - c_a)}{L - H}(y - L) + c_\infty \quad (\text{G.6})$$

At the surface of the evaporating liquid ($y = H$) the mass flux is

$$j_{rel} = -D \frac{dc}{dy} = -D \frac{(c_\infty - c_a)}{L - H} = -D \frac{1}{L - H} (c_\infty - c_a) \quad (\text{G.7})$$

Thus the total mass leaving the surface is

$$j_{rel} A = AD \frac{1}{L - H} (c_\infty - c_a) \quad (\text{G.8})$$

Thus the change in mass of the liquid in the container is given by

$$\frac{dM}{dt} = -AD \frac{1}{L - H} (c_\infty - c_a) \quad (\text{G.9})$$

If we assume the vapor phase is an ideal gas then we can write

$$(c_\infty - c_a) = \frac{M_w}{RT} (P_s^v - P_\infty^v) \quad (\text{G.10})$$

Appendix G: (Continued)

where P_i^v is the vapor pressure of the evaporating liquid at station i . Here M_w is the molecular weight of the liquid and R is the universal gas constant. It is customary to take P_s^v to be the equal to the saturation vapor pressure of the evaporating species P_s^{vs} at temperature T , that is,

$$P_s^v = P_s^{vs} \quad (\text{G.11})$$

Then in the case when water is evaporating in air, we can write

$$(c_s - c_\infty) = \frac{M_w}{RT} (P_s^{vs} - P_\infty^{vs}) = \frac{M_w P_s^{vs}}{RT} (1 - \phi) \quad (\text{G.12})$$

where $\phi = P_\infty^{vs} / P_s^{vs}$ is the relative humidity of the medium. Hence the change in volume of water in the container due to the evaporation is

$$A\rho_L \frac{dH}{dt} = -AD \frac{1}{L-H} \left(\frac{M_w P_s^{vs}}{RT} \right) (1 - \phi) \quad (\text{G.13})$$

and simplifying gives

$$\frac{dH}{dt} = -\frac{D}{\rho_L} \frac{1}{L-H} \left(\frac{M_w P_s^{vs}}{RT} \right) (1 - \phi) \quad (\text{G.14})$$

If the temperature is constant during evaporation (or more precisely quasi-steady), then we have

$$(H_0^2 - H^2) + 2L(H_0 - H) = -\beta t \quad (\text{G.15})$$

Appendix G: (Continued)

$$(H_0^2 - H^2) + 2L(H_0 - H) = -2D \left(\frac{M_w P_s^{vs}}{RT} \right) (1 - \phi) \quad (\text{G.16})$$

The solution to this problem is

$$H(t) = L - \sqrt{H_0^2 - 2H_0L + L^2 + 2t\beta} \quad (\text{G.17})$$

Thus all the water has evaporated when

$$t = \frac{H_0(2L - H_0)}{2\beta} \quad (\text{G.18})$$

Note that temperature effects enter through β . In reality T will be changing albeit slowly. To account for the change in temperature we examine the energy balance.

Temperature Effect: It is best understood by examining the macroscopic energy balance for the evaporating system. But first we start with the thermal energy *point equation* for the liquid which is written as

$$\rho_L c_P \frac{DT}{Dt} = \nabla \cdot (k \nabla T) \quad (\text{G.19})$$

In the point equation we are ignoring viscous dissipation effects and pressure work related terms which is a reasonable assumption for slow evaporation. At the liquid/gas interface of the evaporating liquid we have the following jump boundary conditions (mass and energy):

$$\rho_L (v_L - w) \cdot n = \rho_G (v_G - w) \cdot n \quad (\text{G.20})$$

$$\rho_L H_L (v_L - w) \cdot n + q_L \cdot n = \rho_G H_G (v_G - w) \cdot n + q_G \cdot n \quad (\text{G.21})$$

Appendix G: (Continued)

where H_i is the enthalpy per unit mass of phase i . These two expressions can be combined to give

$$(q_L - q_G) \cdot n = \lambda \rho_L H_G (v_L - w) \cdot n, \quad \lambda = H_1 - H_2 \quad (\text{G.22})$$

where λ is the latent heat of evaporation per unit mass. Integrating point energy equation (G.19) over the liquid volume $V(t)$ gives

$$\frac{d}{dt} \int_{V(t)} \rho_L c_p T dV + \int_{A(t)} \rho_L c_p T (v_L - w) \cdot ndA = \int_{A(t)} q_L \cdot ndA \quad (\text{G.23})$$

Substituting equation (22) into equation(23) to eliminate q_L gives

$$\frac{d}{dt} \int_{V(t)} \rho_L c_p T dV + \int_A \rho_L c_p T (v_L - w) \cdot ndA = \int_{A(t)} q_G \cdot ndA + \int_{A(t)} \lambda \rho_L (v_L - w) \cdot ndA \quad (\text{G.24})$$

Using equation (G.3) we can simplify the RHS of equation (G.24) to give

$$\frac{d}{dt} \int_{V(t)} \rho_L c_p T dV + \int_A \rho_L c_p T (v_L - w) \cdot ndA = A q_G \cdot n - \lambda \frac{dM}{dt} \quad (\text{G.25})$$

The LHS of equation (G.25) can be simplified by making the following assumptions: For small liquid volumes, we can safely assume that T , C_p and ρ_L are approximately uniform within the liquid so that

$$\frac{d}{dt} \int_{V(t)} \rho_L c_p T dV + \int_A \rho_L c_p T (v_L - w) \cdot ndA = \frac{d}{dt} (c_p M T) - c_p T = M c_p \frac{dT}{dt} \quad (\text{G.26})$$

Thus the energy balance becomes

Appendix G: (Continued)

$$Mc_P \frac{dT}{dt} = Aq_G \cdot n - \lambda \frac{dM}{dt} \quad (\text{G.27})$$

In the absence of radiation and convective effects the heat transferred from the gas phase to the liquid is

$$\dot{Q} = Aq_G \cdot n = -Ak_G \frac{dM}{dy} = -Ak_G(T_\infty - T_s) \quad (\text{G.28})$$

where T_s is the surface temperature of the liquid. Thus we can write the energy balance as

$$Mc_G \frac{dT}{dt} = -Ak_G(T_\infty - T_s) - \lambda \frac{dM}{dt} \quad (\text{G.29})$$

Then for a quasi-static process we can assume that $dT/dt \approx 0$, so that

$$(T_\infty - T_s) = -\frac{1}{Ak_G} \frac{dM}{dt} \lambda \quad (\text{G.30})$$

But we have already shown that

$$\frac{dM}{dt} = -AD \frac{1}{L-H} \left(\frac{M_w P_s^{\text{vs}}}{RT} \right) (1-\phi) \quad (\text{G.31})$$

Thus the temperature difference is

$$(T_\infty - T_s) = \frac{\lambda D}{(L-H)k_g} \left(\frac{M_w P_s^{\text{vs}}}{RT} \right) (1-\phi) \quad (\text{G.32})$$

and we have already found that

Appendix G: (Continued)

$$L - H(t) = \sqrt{H_0^2 - 2H_0L + L^2 + 2t\beta} \quad (\text{G.33})$$

So that

$$(T_\infty - T_s) = \frac{\lambda D}{\sqrt{H_0^2 - 2H_0L + L^2 + 2t\beta} k_g} \left(\frac{M_w P_s^{vs}}{RT} \right) (1 - \phi) \quad (\text{G.34})$$

We have not shown how to compute the surface temperature of the water. This requires an energy balance over the liquid phase and then one must account for the energy input (heating) to the liquid. The simplest approach would be to consider only conduction effects so that the energy balance reduces to

$$\nabla \cdot (k_L \nabla T) \quad (\text{G.35})$$

Integrating this over the volume of the liquid and assuming that the *side walls* of the container are insulated, we would get

$$\int_V \nabla \cdot (k \nabla T) dV = \int_A n \cdot \nabla \cdot (k_L \nabla T) dA = Q_{in} - Ak_L \left(\frac{dT}{dy} \right)_H = 0 \quad (\text{G.36})$$

Thus the heat input Q_{in} to the bottom of the container is related to

$$Q_{in} = Ak_L \left(\frac{dT}{dy} \right)_H \quad (\text{G.37})$$

But we have already shown from equation (G.28) that

$$k_G \frac{dT}{dy} = Ak_G (T_\infty - T_s) \quad (\text{G.38})$$

Appendix G: (Continued)

and from continuity of heat flux we have

$$Ak_L \left(\frac{dT}{dy} \right)_H = k_G \left(\frac{dT}{dy} \right)_H = Ak_G (T_\infty - T_s) \quad (\text{G.39})$$

Hence

$$Q_{in} = Ak_G (T_\infty - T_s) = \frac{\lambda D}{\sqrt{H_0^2 - 2H_0L + L^2 + 2t\beta k_g}} \left(\frac{M_w P_s^{vs}}{RT} \right) (1 - \phi) \quad (\text{G.40})$$

Appendix H: Curriculum Vitae

Personal Knowledge

Surname, Name: YILMAZ İbrahim Halil

Nationality: Turkish (T.C.)

Place of Birth and Date: Akçakale / 27 November, 1982

Marital Status: Married

Phone: +90 342 317 2536

Fax: +90 342 360 1104

E-mail: iyilmaz@gantep.edu.tr

Education

Degree	Institution	Year of Graduation
MSc	Natural & Applied Science	2009
BSc	Mechanical Engineering	2005
High School	Gaziantep Cumhuriyet High School	1999

Work Experience

Year	Place	Enrollment
2007–Present	Gaziantep University	Research Assistant
2009–2009	Exitcom Recycling GmbH	Mechanical Engineer
2005–2005	Tanış Milling Machines	Mechanical Engineer

Publication

1. Yılmaz İH., Söylemez MS. (2014). Thermo-mathematical modeling of parabolic trough collector, *Energy Conversion and Management*, **88**, 768–784.
2. Yılmaz İH., Söylemez MS. (2012). Design and computer simulation on multi-effect evaporation seawater desalination system using hybrid renewable energy sources in Turkey, *Desalination*, **291**, 23–40.

International Symposium

1. Yılmaz İH., Söylemez MS., Hayta H., Yumrutaş R. (2014). A Process Heat Application Using Parabolic Trough Collector. In: International Congress on Energy Efficiency and Energy Related Materials (ENEFM2013), *Springer Proceedings in Physics*, **155**, 137–141.
2. Yılmaz İH., Söylemez MS., Hayta H., Yumrutaş R. (2014). Model-Based Performance Analysis of a Concentrating Parabolic Trough Collector Array. In: Progress in Exergy, Energy, and the Environment, **6**, 815–827.

National Symposium

1. Yılmaz İH., Hayta H., Söylemez MS., Yumrutaş R. (2013). Bulgur potasının termal analizi. In: 19. Ulusal Isi Bilimi ve Tekniği Kongresi, **19**, 746–749.

Foreign Languages

1. English
2. German

Hobbies

Art and cultural activities, Reading, Table tennis, Basketball, Chess